

ISTANBUL TECHNICAL UNIVERSITY ★ GRADUATE SCHOOL OF SCIENCE
ENGINEERING AND TECHNOLOGY

**DESIGN AND CHARACTERIZATION OF CARBON INKS
FOR PEROVSKITE SOLAR CELLS**



M.Sc. THESIS

Nur Dilara Öztürk

Department of Nano Science and Nano Engineering

Nano Science and Nano Engineering Programme

JUNE 2018

ISTANBUL TECHNICAL UNIVERSITY ★ GRADUATE SCHOOL OF SCIENCE
ENGINEERING AND TECHNOLOGY

**DESIGN AND CHARACTERIZATION OF CARBON INKS
FOR PEROVSKITE SOLAR CELLS**



M.Sc. THESIS

Nur Dilara ÖZTÜRK
513161006

Department of Nano Science and Nano Engineering

Nano Science and Nano Engineering Programme

Thesis Advisor:Dr. Ali KILIÇ

JUNE 2018

İSTANBUL TEKNİK ÜNİVERSİTESİ ★ FEN BİLİMLERİ ENSTİTÜSÜ

**PEROVSKİT GÜNEŞ PİLLERİ İÇİN KARBON MÜREKKEP TASARIMI VE
KARAKTERİZASYONU**

YÜKSEK LİSANS TEZİ

**Nur Dilara ÖZTÜRK
(513161006)**

Nano Bilim ve Nano Mühendislik Anabilim Dalı

Nano Bilim ve Nano Mühendislik Programı

Tez Danışmanı: Dr. Öğr. Üyesi Ali KILIÇ

HAZİRAN 2018

Nur Dilara Öztürk, a M.Sc. student of ITU Graduate School of Science Engineering and Technology student ID 513161006, successfully defended the thesis/dissertation entitled “DESIGN AND CHARACTERIZATION OF CARBON INKS FOR PEROVSKITE SOLAR CELLS”, which she prepared after fulfilling the requirements specified in the associated legislations, before the jury whose signatures are below.

Thesis Advisor : **Dr. Ali KILIÇ**
İstanbul Technical University

Jury Members : **Dr. Ali KILIÇ**
İstanbul Technical University

Prof. Dr. Ali DEMİR
İstanbul Technical University

Dr. Hüseyin AVCI
Eskişehir Osmangazi University

Date of Submission : 04 May 2018
Date of Defense : 28 June 2018





To my family,



FOREWORD

I would like to thank my advisor, Dr. Ali Kılıç for his guidance and support throughout this thesis. Special thanks to Prof. Dr. Ali Demir and all group members in TEMAG research lab for their help and valuable discussions during my thesis. I would like to very special thank to my friend Elena Stojanovska for supporting in every stage of my thesis. I would also like to thank to Dr. Erhan Sancak and PhD. student Derya Saltık for their precious help. The last but not the least, special thanks to my precious friend Özgür Erol for supporting and encouraging me in every stage of my life.

This project is supported by project number 214M371 of TUBITAK.

June 2018

Nur Dilara ÖZTÜRK
(Textile Engineer)



TABLE OF CONTENTS

	<u>Page</u>
FOREWORD	ix
TABLE OF CONTENTS	xi
ABBREVIATIONS	xiii
SYMBOLS	xv
LIST OF TABLES	xvii
LIST OF FIGURES	xix
1. INTRODUCTION	1
1.1 Purpose of Thesis.....	4
1.2 Literature Review	4
1.2.1 Conductive inks	4
1.2.1.1 Metal based inks	5
1.2.1.2 Organic inks.....	5
1.2.1.3 Carbon based inks.....	5
1.2.2 Electrical conductivity	18
1.2.2.1 Electronic conductivity.....	21
1.2.2.2 Ionic conductivity	22
1.3 Hypothesis	22
2. EXPERIMENTAL TECHNIQUES & METHODS	23
2.1 Experimental Techniques	23
2.1.1 Material characterization	23
2.1.1.1 Scanning electron microscope (SEM)	23
2.1.1.2 BET analysis.....	24
2.1.1.3 Four-point probe method.....	26
2.1.2 Photovoltaic device fabrication technique.....	27
2.1.2.1 UV-Ozone cleaning	27
2.1.2.2 Spin coating	27
2.1.2.3 Doctor blading	28
2.1.2.4 Vacuum thermal evaporation	29
2.1.3 Photovoltaic performance evaluation	29
2.1.3.1 Solar simulator.....	29
2.1.3.2 Current-voltage (JV) curves and power conversion efficiency (PCE).....	31
2.2 Experimental Methods.....	31
2.2.1 Materials	31
2.2.2 Methods	32
2.2.2.1 Preparation of carbon-based conductive ink	32
2.2.2.2 Preparation of environmentally friendly carbon-based conductive ink	32
2.2.2.3 Preparation of doped polymer carbon-based conductive ink	33
2.2.2.4 Preparation of perovskite solar cell	33
3. RESULTS AND DISCUSSION	35
3.1 Properties of Low Temperature Processable Carbon Based Inks.....	35
3.2 Properties of Environmentally Friendly Coffee Waste Carbon-Based Inks.....	37

3.2.1 BET, DFT and Raman analysis results of carbonized coffee particles	37
3.2.2 MC 30/70 results.....	39
3.2.3 TC 1:1 30/70 results.....	41
3.2.4 TC 2:1 30/70 results.....	44
3.2.5 TC 1:2 30/70 results.....	46
3.2.6 TC 1:2 10/90 results.....	48
3.2.7 TC 1:2 50/50 results.....	50
3.3 Properties Of Polymer-Doped Low Temperature Processable Carbon-Based Conductive Ink.....	53
3.3.1 FTIR results of PVDF, silver-doped PVDF and silver nitrate-doped PVDF films.....	53
3.3.2 Silver nanoparticles doped polymer-based carbon ink results	55
3.3.2.1 0.25 mM silver nanoparticles doped PVDF results	55
3.3.2.2 0.5 mM silver nanoparticle doped PVDF results	58
3.3.2.3 0.75 mM silver nanoparticle doped PVDF results	60
3.3.2.4 1.0 mM silver nanoparticle doped PVDF results	62
3.3.3 Silver nitrate doped polymer-based carbon ink results.....	64
3.3.3.1 0.25 mM silver nitrate doped PVDF results	64
3.3.3.2 0.5 mM silver nitrate doped PVDF results	66
3.3.3.3 0.75 mM silver nitrate doped PVDF results	68
3.3.3.4 1.0 mM silver nitrate doped PVDF results	70
3.4 Properties Of Environmentally Friendly and Polymer-Doped Low Temperature Processable Carbon-Based Conductive Ink	72
3.5 Comparison of Perovskite Solar Cell Performance with Different Inks	74
4. CONCLUSIONS AND RECOMMENDATIONS	77
REFERENCES	79
APPENDICES	87
APENDIX A.....	87
CURRICULUM VITAE.....	95

ABBREVIATIONS

- MC 1:1** : Espresso coffee particles carbonized with ZnCl_2 at 1:1 ratio
- TC 1:1** : Turkish coffee particles carbonized with ZnCl_2 at 1:1 ratio
- TC 2:1** : Turkish coffee particles carbonized with ZnCl_2 at 2:1 ratio
- TC 1:2** : Turkish coffee particles carbonized with ZnCl_2 at 1:2 ratio
- MC 1:1 30/70** : Carbonized espresso coffee particles (MC 1:1) to total carbon material ratio is 30/70 in the conductive carbon ink
- TC 1:1 30/70** : Turkish coffee particles carbonized with ZnCl_2 at 1:1 ratio carbonized Turkish coffee particles ratio to total carbon material is 30/70 in conductive carbon ink
- TC 2:1 30/70** : Turkish coffee particles carbonized with ZnCl_2 at 2:1 ratio carbonized Turkish coffee particles ratio to total carbon material is 30/70 in conductive carbon ink
- TC 1:2 30/70** : Turkish coffee particles carbonized with ZnCl_2 at 1:2 ratio carbonized Turkish coffee particles ratio to total carbon material is 30/70 in conductive carbon ink
- TC 1:2 10/90** : Turkish coffee particles carbonized with ZnCl_2 at 1:2 ratio carbonized Turkish coffee particles ratio to total carbon material is 10/90 in conductive carbon ink
- TC 1:2 50/50** : Turkish coffee particles carbonized with ZnCl_2 at 1:2 ratio carbonized Turkish coffee particles ratio to total carbon material is 50/50 in conductive carbon ink
- BET** : Brunauer–Emmett–Teller theory
- FTIR** : Fourier-transform infrared spectroscopy
- SEM** : Scanning electron microscopy
- PVDF** : Polyvinylidene fluoride
- ETHOCEL** : Ethylcellulose



SYMBOLS

ρ	: Bulk resistivity
V	: Voltage
I	: Current
t	: Thickness
k	: Correction factor
σ	: Sheet resistance
AM	: Air Mass
I_D	: Diode current
I_{SH}	: Shunt current
R_S	: Series resistor
R_{SH}	: Shunt resistance
V_{oc}	: Open circuit voltage
I_{sc}	: Short circuit current
FF	: Fill factor
PCE	: Power conversion efficiency



LIST OF TABLES

	<u>Page</u>
Table 1.1 : Resistivity and conductivity of some materials at 20 °C [80].	19
Table 2.1 : Type of solar spectrum and filters with power density and transmission capacity [96].	30
Table 2.3 : Illustration of type of coffee waste carbon and denotation.	33
Table 3.1 : Resistivity results of low temperature procesable carbon ink.....	37
Table 3.2 : Resistivity results of MC 30/70 carbon ink.	41
Table 3.3 : Resistivity results of TC 1:1 30/70 carbon ink.	43
Table 3.4 : Resistivity results of TC 2:1 30/70 carbon ink.	46
Table 3.5 : Resistivity results of TC 1:2 30/70 carbon ink.	48
Table 3.6 : Resistivity results of TC 1:2 10/90 carbon ink.	50
Table 3.7 : Resistivity results of TC 1:2 50/50 carbon ink.	52
Table 3.8 : Polymorph structures of PVDF and their properties [101].	54
Table 3.9 : Wavenumber of polymorph structures of PVDF [101], [103], [104].	55
Table 3.10 : Resistivity results of 0,25mM Ag doped-PVDF carbon ink.	58
Table 3.11 : Resistivity results of 0,5 mM Ag-doped PVDF carbon ink.....	60
Table 3.12 : Resistivity results of 0,75 mM Ag doped-PVDF carbon ink.....	62
Table 3.13 : Resistivity results of 1.0 mM Ag doped PVDF carbon ink.	64
Table 3.14 : Resistivity results of 0,25 mM AgNO ₃ doped PVDF carbon ink.	66
Table 3.15 : Resistivity results of 0,5 mM AgNO ₃ doped PVDF carbon ink.	68
Table 3.16 : Resistivity results of 0,75 mM AgNO ₃ doped PVDF carbon ink.	70
Table 3.17 : Resistivity results of 1,0 mM AgNO ₃ doped PVDF carbon ink.	72
Table 3.18 : Resistivity results of TC 1:2 30:70 & 1,0 mM Ag doped PVDF carbon ink.....	74
Table 3.19 : Comparison of the photovoltaic results of perovskite solar cells with carbon electrodes.	75



LIST OF FIGURES

	<u>Page</u>
Figure 1.1 : World energy demand (2016-2040) [1].	1
Figure 1.2 : World energy consumption in 2016 [2].	1
Figure 1.3 : World energy growing demand (1990-2016) [2].	2
Figure 1.4 : Consumption rate of energy sources [2].	2
Figure 1.5 : Regional solar installed capacity [3].	3
Figure 1.6 : SEM images a) untreated cotton fabric b) the conductive cotton fabric of hybrid PANI/CB at 9.34wt% [35].	6
Figure 1.7 : Carbon ink for various sensor applications.	7
Figure 1.8 : Solar cell structure [55].	10
Figure 1.9 : Classification of solar cell.	10
Figure 1.10 : Efficiency diagram of different type solar cells [56].	11
Figure 1.11 : Structure of perovskite [58].	11
Figure 1.12 : Structures of perovskite solar cell with HTM [58].	12
Figure 1.13 : HTM-free perovskite solar cell with a) m-carbon b) p-carbon structure. c) Working principle of the perovskite solar cell with carbon electrode [62].	14
Figure 1.14 : m-carbon based perovskite solar cell [63].	14
Figure 1.15 : a) Configuration b) working principle of the perovskite solar cell [66].	15
Figure 1.16 : Carbon electrode a) with printed on the FTO and clamping b) printed on the perovskite and clamping c) printed on the PbI ₂ [72].	17
Figure 1.17 : Working principle of perovskite solar cell with thermoelectric device [75].	18
Figure 1.18 : Illustration of conduction and valance band of a) insulator b) semiconductor c) conductor [84].	22
Figure 2.1 : Main components of SEM [86].	24
Figure 2.2 : BET plot [87].	25
Figure 2.3 : Four-point probe test circuit [88].	26
Figure 2.4 : Mechanism of UV/Ozone cleaning system [90].	27
Figure 2.5 : Spin coating mechanism [92].	28
Figure 2.6 : Doctor blading technique with frame apperture [93].	28
Figure 2.7 : Doctor blading technique with spiral aperture [93].	29
Figure 2.8 : Schematic illustration of vacuum evaporation method [94].	29
Figure 2.9 : Solar cell circuit diagram [97].	31
Figure 3.1 : Images of the low temperature processable carbon ink with a) 45 μm b) 130 μm and c) 255 μm thickness.	35
Figure 3.2 : Optic microscope results of low temperature processable carbon ink with a) 45 μm b) 130 μm and c) 255 μm thickness.	35
Figure 3.3 : SEM images of low temperature processable carbon ink wit a)500x b)5.00kx magnification.	36

Figure 3.4 : EDAX results of low temperature processable carbon ink.	36
Figure 3.5 : Resistivity diagram of low temperature procesable carbon ink.	37
Figure 3.6 : BET surface area analysis for carbonized coffee particles.	38
Figure 3.7 : DFT test results of carbonized particles for a) cumulative surface volume and b) cumulative surface area.	38
Figure 3.8 : Raman results of carbonized coffee particles.....	39
Figure 3.9 : Images of the MC 30/70 carbon ink with a) 45 μm b) 130 μm and c) 255 μm thickness.	39
Figure 3.10 : Optic microscope images of MC 30/70 carbon ink with a) 45 μm b) 130 μm and c) 255 μm thickness.....	40
Figure 3.11 : SEM images a) 500x b) 5.00kx magnification of MC 30/70 carbon ink.	40
Figure 3.12 : EDAX results of MC 30/70 carbon ink.....	41
Figure 3.13 : Images of the TC 1:1 30/70 carbon ink with a) 45 μm b) 130 μm and c) 255 μm thickness.	42
Figure 3.14 : Optic microscope images of TC 1:1 30/70 carbon ink with a) 45 μm b) 130 μm and c) 255 μm thickness.....	42
Figure 3.15 : SEM images a) 500x b) 5.00kx magnification of TC 1:1 30/70 carbon ink.	43
Figure 3.16 : EDAX results of TC 1:1 30/70 carbon ink.	43
Figure 3.17 : Images of the TC 2:1 30/70 carbon ink with a) 45 μm b) 130 μm and c) 255 μm thickness.	44
Figure 3.18 : Optic microscope images of TC 2:1 30/70 carbon ink with a) 45 μm b) 130 μm and c) 255 μm thickness.....	44
Figure 3.19 : SEM images a) 500x b) 5.00kx magnification of TC 2:1 30/70 carbon ink.	45
Figure 3.20 : EDAX results of TC 2:1 30/70 carbon ink.	45
Figure 3.21 : Images of the TC 1:2 30/70 carbon ink with a) 45 μm b) 130 μm and c) 255 μm thickness.	46
Figure 3.22 : Optic microscope images of TC 1:2 30/70 carbon ink with with a) 45 μm b) 130 μm and c) 255 μm thickness.....	46
Figure 3.23 : SEM images a) 500x b) 5.00kx magnification of TC 1:2 30/70 carbon ink.	47
Figure 3.24 : EDAX results of TC 1:2 30/70 carbon ink.	47
Figure 3.25 : Images of the TC 1:2 10/90 carbon ink with a) 45 μm b) 130 μm and c) 255 μm thickness.	48
Figure 3.26 : Optic microscope images TC 1:2 10/90 carbon ink with a) 45 μm b) 130 μm and c) 255 μm thickness.....	48
Figure 3.27 : SEM images a) 500x b) 5.00kx magnification of TC 1:2 10/90 carbon ink.	49
Figure 3.28 : EDAX results of TC 1:2 10/90 carbon ink.	49
Figure 3.29 : Images of the TC 1:2 50/50 carbon ink with a) 45 μm b) 130 μm and c) 255 μm thickness.	50
Figure 3.30 : Optic microscope results of TC 1:2 50/50 carbon ink with a) 45 μm b) 130 μm and c) 255 μm thickness.....	50
Figure 3.31 : SEM images a) 500x b) 5.00kx magnification of TC 1:2 50/50 carbon ink.	51
Figure 3.32 : EDAX results of TC 1:2 50/50 carbon ink.	51
Figure 3.33 : Resistivity comparison of low temperature processable and biowaste carbon inks.	53

Figure 3.34 : FTIR results of PVDF/silver-doped PVDF and silver nitrate-doped PVDF.	55
Figure 3.35 : Images of the 0,25 mM Ag doped-PVDF carbon ink with a) 45 μm b) 130 μm and c) 255 μm thickness.	56
Figure 3.36 : Optic microscope images of 0,25 mM Ag doped-PVDF carbon ink with a) 45 μm b) 130 μm and c) 255 μm thickness.	56
Figure 3.37 : SEM images a) 500x b) 5.00kx magnification of 0,25mM Ag doped-PVDF carbon ink.	57
Figure 3.38 : EDAX results of 0,25mM Ag doped-PVDF carbon ink.	57
Figure 3.39 : Images of the 0,5 mM Ag doped-PVDF carbon ink with a) 45 μm b) 130 μm and c) 255 μm thickness.	58
Figure 3.40 : Optic microscope images of 0,5 mM Ag doped-PVDF carbon ink with a) 45 μm b) 130 μm and c) 255 μm thickness.	58
Figure 3.41 : SEM images a) 500x b) 5.00kx magnification of 0,5mM Ag doped-PVDF carbon ink.	59
Figure 3.42 : EDAX results of 0,5mM Ag doped-PVDF carbon ink.	59
Figure 3.43 : Images of the 0,75 mM Ag doped-PVDF carbon ink with a) 45 μm b) 130 μm and c) 255 μm thickness.	60
Figure 3.44 : Optic microscope images of 0,75 mM Ag doped-PVDF carbon ink with a) 45 μm b) 130 μm and c) 255 μm thickness.	60
Figure 3.45 : SEM images a) 500x b) 5.00kx magnification of 0,75mM Ag doped-PVDF carbon ink.	61
Figure 3.46 : EDAX results of 0,75mM Ag doped-PVDF carbon ink.	61
Figure 3.47 : Images of the 1,0 mM Ag doped-PVDF carbon ink with a) 45 μm b) 130 μm and c) 255 μm thickness.	62
Figure 3.48 : Optic microscope images of 1,0 mM Ag doped-PVDF carbon ink with a) 45 μm b) 130 μm and c) 255 μm thickness.	62
Figure 3.49 : SEM images a) 500x b) 5.00kx magnification of 1,0mM Ag doped-PVDF carbon ink.	63
Figure 3.50 : EDAX results of 1,0mM Ag doped-PVDF carbon ink.	63
Figure 3.51 : Images of the 0,25 mM AgNO ₃ doped-PVDF carbon ink with a) 45 μm b) 130 μm and c) 255 μm thickness.	64
Figure 3.52 : Optic microscope images of 0,25 mM AgNO ₃ doped-PVDF carbon ink with a) 45 μm b) 130 μm and c) 255 μm thickness.	64
Figure 3.53 : SEM images a) 500x b) 5.00kx magnification of 0,25mM AgNO ₃ doped-PVDF carbon ink.	65
Figure 3.54 : EDAX results of 0,25mM AgNO ₃ doped-PVDF carbon ink.	65
Figure 3.55 : Images of the 0,5 mM AgNO ₃ doped-PVDF carbon ink with a) 45 μm b) 130 μm and c) 255 μm thickness.	66
Figure 3.56 : Optic microscope images of 0,5 mM AgNO ₃ doped-PVDF carbon ink with a) 45 μm b) 130 μm and c) 255 μm thickness.	66
Figure 3.57 : SEM images a) 500x b) 5.00kx magnification of 0,5mM AgNO ₃ doped-PVDF carbon ink.	67
Figure 3.58 : EDAX results of 0,5mM AgNO ₃ doped-PVDF carbon ink.	67
Figure 3.59 : Images of the 0,75 mM AgNO ₃ doped-PVDF carbon ink with a) 45 μm b) 130 μm and c) 255 μm thickness.	68
Figure 3.60 : Optic microscope images of 0,75 mM AgNO ₃ doped-PVDF carbon ink with a) 45 μm b) 130 μm and c) 255 μm thickness.	68
Figure 3.61 : SEM images a) 500x b) 5.00kx magnification of 0,75mM AgNO ₃ doped-PVDF carbon ink.	69

Figure 3.62 : EDAX results of 0,75mM AgNO ₃ doped-PVDF carbon ink.	69
Figure 3.63 : Images of the 1,0 mM AgNO ₃ doped-PVDF carbon ink with a) 45 μm b) 130 μm and c) 255 μm thickness.....	70
Figure 3.64 : Optic microscope images of 1,0 mM AgNO ₃ doped-PVDF carbon ink with a) 45 μm b) 130 μm and c) 255 μm thickness.	70
Figure 3.65 : SEM images a) 500x b) 5.00kx magnification of 1,0 mM AgNO ₃ doped-PVDF carbon ink.	71
Figure 3.66 : EDAX results of 1,0 mM AgNO ₃ doped-PVDF carbon ink.	71
Figure 3.67 : Images of the TC 1:2 30:70 & 1,0 mM Ag doped-PVDF carbon ink with a) 45 μm b) 130 μm and c) 255 μm thickness.	72
Figure 3.68 : Optic microscope images of TC 1:2 30:70 & 1,0 mM Ag doped-PVDF carbon ink with a) 45 μm b) 130 μm and c) 255 μm thickness.	72
Figure 3.69 : SEM images a) 500x b) 5.00kx magnification of TC 1:2 30:70 & 1,0 mM Ag doped-PVDF carbon ink.....	73
Figure 3.70 : EDAX results of TC 1:2 30:70 & 1,0 mM Ag doped-PVDF carbon ink.	73
Figure 3.71 : Resistivity comparision of low temperature and doped polymer carbon inks.....	74
Figure A.1 : SEM images of unball milled coffee-waste carbon particles with 500x magnification.	87
Figure A.2 : SEM images of ball milled coffee-waste carbon particles with 50.00kx magnification.	88
Figure A.3 : Particle size of unball milled and ball milled coffee-waste carbon particles.	88
Figure A.4 : Bulk resistivity comparision of all inks.	89
Figure A.5 : a) Perovksite solar cell with low temperature processable carbon ink, and b) Low temperature processable carbon ink coated perovskite solar cell current density-voltage diagram.....	89
Figure A.6 : a) Perovksite solar cell with TC 1:2 30/70 carbon ink, and b) TC 1:2 30/70 carbon ink coated perovskite solar cell current density-voltage diagram.	89
Figure A.7 : a) Perovksite solar cell with 0,25mM Ag doped-PVDF carbon ink, and b) 0,25mM Ag doped-PVDF carbon ink coated perovskite solar cell current density-voltage diagram.....	90
Figure A.8 : a) Perovksite solar cell with 0,5mM Ag doped-PVDF carbon ink, and b) 0,5mM Ag doped-PVDF carbon ink coated perovskite solar cell current density-voltage diagram.....	90
Figure A.9 : a) Perovksite solar cell with 0,75mM Ag doped-PVDF carbon ink, and b) 0,75mM Ag doped-PVDF carbon ink coated perovskite solar cell current density-voltage diagram.....	90
Figure A.10 : a) Perovksite solar cell with 1,0mM Ag doped-PVDF carbon ink, and b) 1,0mM Ag doped-PVDF carbon ink coated perovskite solar cell current density-voltage diagram.....	91
Figure A.11 : a) Perovksite solar cell with 0,25mM AgNO ₃ doped-PVDF carbon ink, and b) 0,25mM AgNO ₃ doped-PVDF carbon ink coated perovskite solar cell current density-voltage diagram.	91
Figure A.12 : a) Perovksite solar cell with 0,5mM AgNO ₃ doped-PVDF carbon ink, and b) 0,5mM AgNO ₃ doped-PVDF carbon ink coated perovskite solar cell current density-voltage diagram.	91

Figure A.13 : a) Perovksite solar cell with 0,75mM AgNO3 doped-PVDF carbon ink, and b) 0,75mM AgNO3 doped-PVDF carbon ink coated perovskite solar cell current density-voltage diagram.....**92**

Figure A.14 : a) Perovksite solar cell with 1,0mM AgNO3 doped-PVDF carbon ink, and b) 1,0mM AgNO3 doped-PVDF carbon ink coated perovskite solar cell current density-voltage diagram.**92**

Figure A.15 : a) Perovksite solar cell with TC 1:2 30:70 & 1,0 mM Ag doped PVDF carbon ink, and b) TC 1:2 30:70 & 1,0 mM Ag doped PVDF carbon ink coated perovskite solar cell current density-voltage diagram.**92**

Figure A.16 : Comparision of solar cell efficiency.**93**





DESIGN AND CHARACTERIZATION OF CARBON INKS FOR PEROVSKITE SOLAR CELL

SUMMARY

Energy demand in the world has been increasing in every day because of increasing human population and improving technology. Between the 2016 and 2040 it is estimated that energy needs of the humanity will expand 30%. Traditional energy sources couldn't meet the demand so researchers have focused on the new and renewable energy sources.

Solar energy is one of the important renewable energy source can decrease the energy needs in the world. Especially in the improved countries many researches have focused on this topic to improve the efficiency and getting commercialization. According to World Energy Council data at the end of the 2016, Germany is the leader solar installed capacity of the world. In this area, Turkey doesn't have sufficient installed solar capacity, however, installed solar capacity are growing day by day.

Solar cell converts sunlight to the electricity with semiconductor materials and part of the solar energy sources. It can be divided into three categories and perovskite solar cell is the latest and encouraging generation of this solar cells because of their low cost, easy to produce and high efficiency.

Perovskite solar cell structure is based on with hole transport layer and without hole transport layer. For hole transport layer generally has been used spiro-Ometad which is high cost material. On the other hand, in the HTM-free perovskite solar cell, perovskite acts as a hole transport layer and conductivity is supplied from carbon electrode or gold electrode. Carbon electrode has been preferred because of its high conductivity, low cost, abundant in nature and environmentally friendly properties. Electrode can be obtained from bare carbon type or carbon ink/paste.

Carbon ink generally contains carbon material, binder and solvent. Carbon material can be different type of carbon such as activated carbon, carbon black, graphite, graphene, carbon nanotubes etc. In the ink formulation, carbon supply electrical conductivity of the ink and binder is responsible for the ink stability. According to

solvent type carbon ink may be dissolved in water based or polymer based solvents. Carbon ink is preferred while the high conductivity is requested. Solar cell, supercapacitor, bioelectronic, textile, tissue engineering and sensor are main application areas of the carbon ink.

In this thesis, carbon inks were designed and characterized. First carbon ink was processed at room temperature on the FTO substrate and its electrical conductivity and morphologic structures were determined. Moreover, it was applied on the perovskite solar cell and measured the photovoltaic properties. As second type, carbon inks containing carbon particles obtained by carbonization of two different type of coffee waste with different ratio of activation material were prepared and their resistivity and morphology were investigated. In the third type of carbon inks, doped polymer structures were used and processed at low temperature on FTO surface in order to measure their electrical resistivity and to determine their morphologic structures. The lowest resistivity inks obtained from all the ink types were applied by doctor blade method as electrodes on perovskite solar cell and the performance of the cells were tested.

PEROVSKİTE GÜNEŞ PİLLERİ İÇİN KARBON MÜREKKEP TASARIMI VE KARAKTERİZASYONU

ÖZET

Dünyada artan insan popülasyonu ve birliktelik enerji ihtiyacı da katlanarak artmaktadır. Ayrıca gelişen teknolojinin getirdiği enerjiye bağımlılık kullanılan geleneksel enerji kaynaklarının tükenmesine neden olmaktadır. Buna ek olarak geleneksel enerji kaynaklarının özellikle petrol bazlı kaynaklar Dünya üzerindeki karbon ayak izini arttırmakta ve çevreyi olumsuz yönde etkilemektedir. Bu nedenlerle araştırmacılar yeni, çevreye zarar vermeyen ve yenilenebilir enerji kaynaklarını araştırmaya başladılar. Güneş enerjisi, rüzgar enerjisi, hidrolik enerji, jeotermal enerji, biyokütle enerjisi, hidrojen enerjisi, dalga enerjisi, gelgit enerjisi vb. gibi konularda birçok araştırma yapılmaktadır. Bunların arasında Güneş enerjisi özellikle ev sistemlerinde, taşıt sistemlerinde ve daha birçok alanda kullanılmaya başlanmış ve gün geçtikçe hem akademide hem de ticari alanda artan verimlilikle önemini arttırmaktadır.

Güneş enerjisinden yararlanmak için kullanılan fotovoltaik piller (güneş pilleri) Güneş'ten gelen ışınların bir yarı iletken yardımıyla elektrik enerjisine dönüşmesini sağlayan pillerdir. Bu sistemler uzay teknolojisinde uzay gemilerinde yada uydularda, evlerde su ısıtma yada ev elektrik enerjisinin karşılanması, yollarda aydınlatma sistemlerinde veya yol kenarındaki işaret lambalarında, arabalarda, teknelerde gibi birçok alanda kullanılmaktadır. Üretilmeye başlandıktaki maliyetlerinin hızla düşmesi ve özellikle gelişmiş ülkelerde güneş enerjisinin kullanılması için verilen teşviklerle gün geçtikçe kullanımları artmaktadır. Almanya 2016 yıl sonunda 39.6 GW kurulu Güneş enerjisi kapasitesi ile Dünya'da başı çekmektedir, onu daha sonra Çin, Japonya, İtalya ve Amerika Birleşik Devletleri izlemektedir. Türkiye'de ise kurulu Güneş enerjisi kapasitesi 2016 yılı sonu verilerinde 249 MW olarak kayda geçmiştir.

Fotovoltaik pillerin gelişimi genel olarak üç gruba ayrılmaktadır. İlk jenerasyon piller kristalin silikon piller olup, üretim aşaması zorlu ve maliyeti yüksektir. İkinci jenerasyon piller amorf Si, polikristaline Si ve bakır indiyum galyum selenit Güneş pilleridir. Birinci jenerasyon pillerle karşılaştırıldığında verimliliği yüksek olmasına

rağmen, tekrarlanabilirliği ve yüzey düzgünlülüğü açısından ticarileşmeye yeteri kadar uygun değillerdir. Bunun üzerine üçüncü jenerasyon piller geliştirilmiştir. Bu tür piller esnek yüzeylere uygulanabilirliği, düşük maliyet ve üretim yöntemlerinin kolaylığı açısından ticari olarak avantaj sağlamaktadırlar.

Perovskit güneş pilleri de üçüncü jenerasyon güneş pillerinden olup, araştırılmaya başlandığı günden itibaren kısa bir sürede 22% verimliliğe ulaşmıştır. Perovskit yapısında iki tip katyon ve bir tip anyon bulundurmaktadır. Yapıdaki katyon veya anyonun değiştirilmesiyle optik ve elektriksel özellikleri değişmektedir. Kontrol edilebilen enerji bant aralığı, geliştirilebilen verimliliği ve üretim kolaylığı açısından Güneş pillerinde tercih edilmektedir. Perovskit güneş pilleri boşluk taşıma katmanı bulunduran ve bulundurmayan olarak ikiye ayrılmaktadır. Boşluk taşıma katmanı bulunduran pillerde bu katman genel olarak Spiro-Ometad yapısından yapılmaktadır. Spiro-Ometad'ın yüksek maliyetli olması nedeniyle araştırmacılar bu katmansız piller üretmeye başlamışlardır. Boşluk taşıma katmanı olmayan perovskitli güneş pillerinde başlıca altın veya karbon olarak iki tip elektrot kullanılmaktadır. Altının doğada nadir bulunması ve pahalı olması nedeniyle ve karbonun doğada bol bulunması, çevre dostu olması ve yüksek elektrik iletkenliği nedeniyle araştırmalar karbon elektrot üzerine yoğunlaşmıştır. Karbon elektrot için oluşturulan katman karbonun direk uygulanması veya bir mürekkep yada pasta olarak güneş pilline uygulanmasıyla elde edilir.

Karbon mürekkep genel olarak karbon malzeme, bağlayıcı malzeme ve çözücü ortamı içermektedir. Elektrik iletkenliği karbon malzeme tarafından sağlanırken, stabilitesi bağlayıcı malzeme tarafından sağlanmaktadır. İçerdiği karbon malzeme karbon siyahı, grafit, karbon nanotüp gibi farklı karbon kaynakları olabilir. Çözüldüğü malzeme açısından ise su bazlı veya organik çözücü olmak üzere ikiye ayrılabilir. Karbon mürekkep sıklıkla yüksek iletkenliğin istenildiği alanlarda kullanılmaktadır ve düşük maliyeti açısından tercih edilmektedir. Sensör, güneş pilleri, biyoelektronikler, tekstil, süperkapasitörler, doku mühendisliği gibi uygulama alanları bulunmaktadır.

Bu tez kapsamında, üç ayrı başlıkta oluşturulan karbon mürekkep özellikleri incelenmiştir. İlk tip karbon mürekkep oda sıcaklığında FTO yüzeye uygulanarak elektrik iletkenliği ve morfolojik özellikleri incelenmiştir. Ayrıca perovskit güneş pillerinde verimliliği ve uygulanabilirliği araştırılmıştır. İkinci tip karbon mürekkep, iki farklı kahve atığının farklı oranlarda aktive edici malzemeyle karbonize edilmesi sonucu elde edilen karbondan oluşturulmuştur. Elde edilen karbonların parçacık

büyüklikleri mürekkepte kullanılmak için büyük olduğu saptanmıştır. Bunun üzerine karbonlar bilyalı öğütücüde öğütülerek hem parçacık boyutları küçültülmüş hem de daha homojen bir dağılım oluşturulmuştur. Daha sonra SEM, DFT, BET ve Raman analizleri ile morfolojik ve fiziksel özellikleri hakkında analizler yapılmıştır. Yapılan analizler sonunda öğütülen karbonlardan, karbon mürekkepler yapılmıştır ve mürekkeplerin elektrik iletkenlik ve morfolojik değerleri incelenmiştir. En düşük direnç değerini veren mürekkep ile perovskit güneş pili denemesi yapılmıştır. Üçüncü tip karbon mürekkep de ise polimer malzeme katkılanmıştır. Yapılan literatür çalışması sonunda PVDF polimerinin perovskit güneş pillerinde kullanılmadığı ve bunun nedeninin ise PVDF'in çözücü ortamı olarak DMF'in tercih edilmesidir. DMF ise perovskit malzemeye uygulandığında, perovskit yapısını çözerek güneş piline zarar vermektedir. Fakat bu tez kapsamında çözücü ortamı olarak DMF kullanılmayıp, perovskit malzemeyi deforme etmeyen etil asetat kullanılmıştır. Polimer malzemenin katkılanarak elektriksel özelliklerinin geliştirilmesi için ise gümüş nanopartikül ve gümüş nitrat olmak üzere iki farklı katkı maddesiyle çalışılmıştır. Sadece PVDF film, gümüşle katkılanan PVDF film ve gümüş ntratla katkılanan PVDF filmin FTIR sonuçları alınarak kristallite özellikleri araştırılmıştır. Gümüş naopartikül ve gümüş nitrat malzemenin PVDF'in kristalin özelliklerini geliştirdiği görülmüş ve değişik miktarlarda katkılama yapılarak optimum oran bulunulmaya çalışılmıştır. Farklı oranlarda katkılanan polimerle karbon mürekkepler yapılarak, deneyler sonucu elde edilen mürekkeplerin elektrik iletkenlik ve morfolojik özellikleri araştırılmıştır. Düşük direnç değeri veren mürekkepler düşük sıcaklıkta perovskit güneş piline uygulanarak, çalışılabilirliği araştırılmıştır.

1. INTRODUCTION

In every year population of humanity is increasing, correspondingly energy demand in the world is growing tremendously. However, traditional energy sources couldn't satisfy the need. According to International Energy Agency energy demand will extend 30% over the world and below figure shows the energy demand growing rate in million tones of oil equivalent in countries until the 2040 [1].

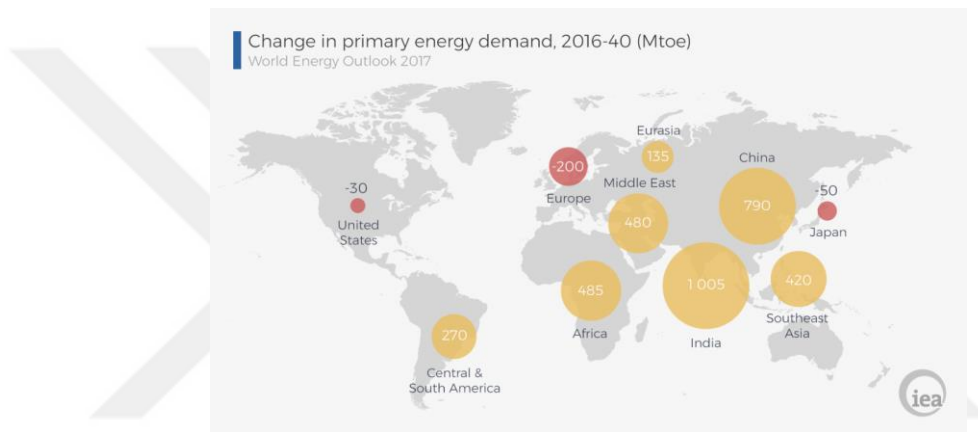


Figure 1.1 : World energy demand (2016-2040) [1].

The figure below shows energy consumption (Mtoe) in 2016. According to data China, USA and India lead the way as 3123 Mtoe, 2204 Mtoe and 884 Mtoe respectively [2].

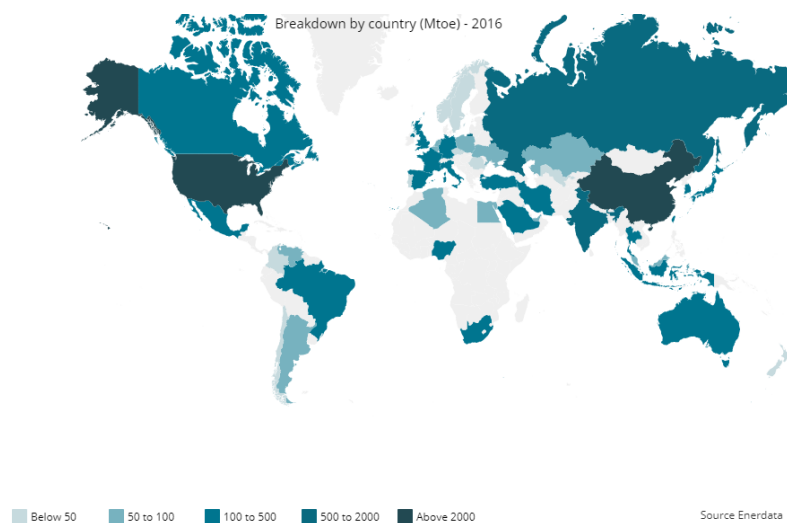


Figure 1.2: World energy consumption in 2016 [2].

Since 1996 energy consumption is expanding rapidly, unfortunately oil sources that are the most harmful source to the environment are the most popular source to supply energy demand. Figure 1.3 demonstrate the growing demand in Mtoe and Figure 1.4 consumption of energy sources rate [2].

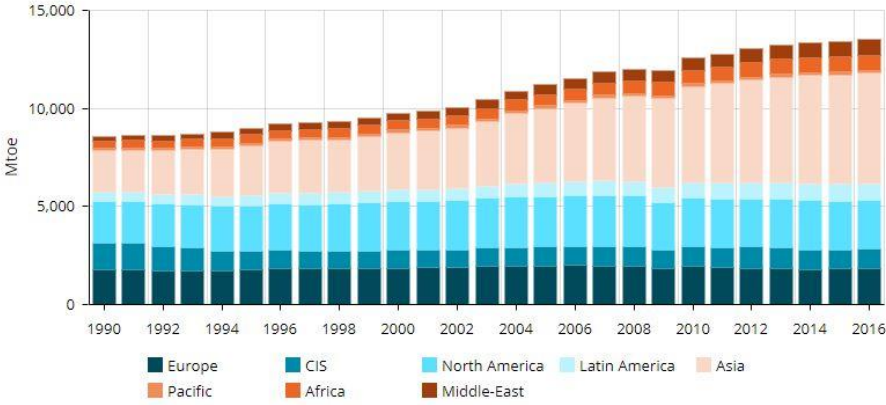


Figure 1.3 : World energy growing demand (1990-2016) [2].

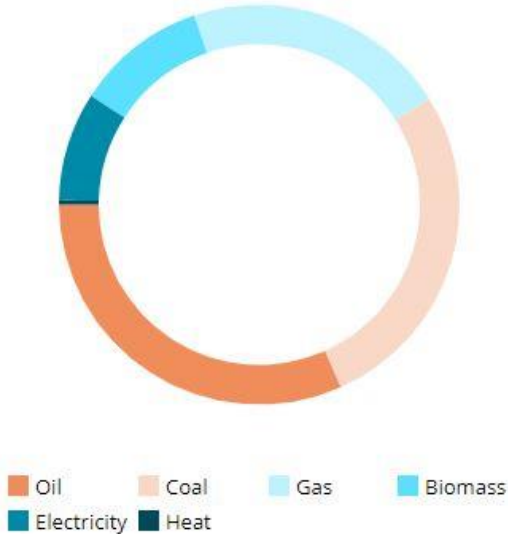


Figure 1.4 : Consumption rate of energy sources [2].

To decrease the usage of oil sources and energy demand new renewable energy sources have been investigated. In recent researches, sunlight, wind, rain, tides and geothermal heat are the important topics for obtaining electricity, heating and transportation service [3].

Solar energy is a renewable energy source causes to decrease carbon emissions. Moreover, it can reduce the usage of traditional energy sources which are hazardous

for the environment. For instance, 200 kg of coal, 140 m³ of natural gas or a barrel of oil consumption can be met the global average solar energy. Solar energy is obtaining from sun in two ways; photovoltaic and thermal collector. The main working principle of the device is sunlight irritates the device and stimulated device generate electricity with supporting equipment like thermal collector or without any supporting equipment as a photovoltaic. At the end of the 2015, in global installed capacity for solar-powered electricity has been arrived at approximately 227GWe and Germany has been leader to installed PV capacity. Below Figure 1.5 illustrate the solar installed capacity by region according to World Energy Council's data [3].

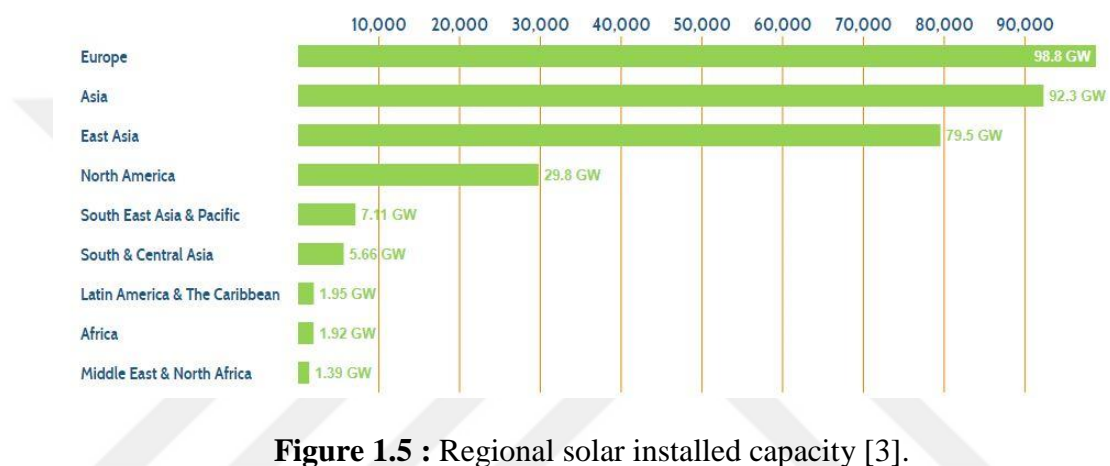


Figure 1.5 : Regional solar installed capacity [3].

To get more power supply from PV many studies have been conducted in academia. Perovskite solar cell application have aroused attention due to its improved efficiency. Perovskite solar cell can be divided in two categories as with HTM and HTM-free solar cell. For hole transporting layer, generally is used spiro-OMETAD which is very expensive material. On the other hand, HTM-free solar cell are based on the Au electrode and carbon electrode which is made from carbon ink or rare carbon. However, Au is rare and high cost material compare to carbon. Moreover, carbon is abundant in nature and it is environmentally friendly material.

With developing of technologies new and smart materials are hot topic in the world. Smart textiles which show human blood pressure or temperature, paper-based conductive materials, conductive pens and etc. are new and popular materials. Carbon ink may used as a conductive material for these devices. It can be applied in textile, solar cell, sensor, bioelectronic and tissue engineering. It basically consists of carbon material, solvent and binders. Carbon ink is preferred due to its high conductivity, low cost, environmentally friendly and easy to process properties.

1.1 Purpose of Thesis

Purpose of this thesis is production of low temperature carbon-based conductive ink and its application as electrode in perovskite solar cell. According to this purpose, three types of carbon-based conductive inks were produced, as follows:

- 1) low temperature carbon-based conductive ink, using commercial carbon particles
- 2) environmentally friendly low temperature carbon-based conductive ink, using coffee waste as carbon source, and
- 3) doped polymer low temperature carbon-based conductive ink.

All types of inks were characterized with scanning electron microscopy (SEM) and their conductivity was measured with four-probe method. Moreover, for the carbonized coffee wastes particles were characterized with BET and Raman spectroscopy, while FTIR spectroscopy was used for characterization of the doped polymer.

Perovskite solar cell was chosen as application area. The as prepared conductive inks were used as an electrode on the solar cells. Photovoltaic performance of cells were determined and compared with commonly used silver electrode.

1.2 Literature Review

1.2.1 Conductive inks

Conductive ink is aroused interest of researchers due to its easy to apply and low cost [4]. Basically, conductive inks can be divided in three categories; conductive polymer inks, metal based inks, and carbon-based inks [4]. To compare the metal based inks with polymer based inks, metal based inks are generally preferred when require high conductivity [4]. However, metal based conductive inks are more expensive. On the other hand, carbon based conductive inks both have high conductivity and are low cost [4]. Conductive inks can be applied with different techniques such as gravure printing, screen printing, inkjet printing, flexographic printing, spray coating, knife coating, slot-die coating, double slot-die printing [5]

1.2.1.1 Metal based inks

Conductive ink consists of polymer matrix, conductive ingredient, solvent and additives [6]. For metal based inks, conductivity is supplied from metal nanoparticles or nanomaterials. Metal based conductive inks can be termed according to their metal ingredient. Gold [7], silver [8–16], copper [17–26] and aluminum [27] are most important and popular metals for conductive inks due to their high conductivity. Metal based conductive inks can be applied in a sensor, electronics application field, communication, energy transformation devices, MEMS/NEMS devices, display devices and computer equipments [5].

1.2.1.2 Organic inks

Organic conductive inks consist of conductive polymer which supply electrical conductivity instead of metal or carbon. Comparing metal based or carbon based conductive inks organic conductive inks have some advantages. For instance, thin film formation can not be regular with metal or carbon based ink if particles don't be distributed homogeneously in the ink. However, homogenous and regular film formation can be obtained from organic conductive inks [28]. The most common used conductive polymer is poly(3,4-ethylenedioxythiophene) and polystyrene sulfonate (PEDOT:PSS) due to its high conductivity, high chemical and thermal stability and flexibility [28]. It can be combine with different particles or materials such as Tungsten oxide (WO₃) [29] and carbon nanotubes [28] or can be used alone [30].

1.2.1.3 Carbon based inks

Carbon-based ink may contains different types of carbon materials such as carbon black, graphite, carbon nanotubes etc. and can be applied in various application areas as textile, solar cell, sensor, bioelectronic, supercapacitor and tissue engineering. Carbon materials are generally considered as an ingredient of ink because of their high conductivity and low cost compared to other types of conductive inks [4]. Carbon based inks may contain carbon particles, a polymeric binder and a solvent [31]. Electrical conductivity of the ink is supplied by carbon particles, stability of the ink is preserved by polymeric binder and solvent is the solution media of the ink [31]. Solvent types of carbon-based ink can be classified as water-based solvent and organic-based solvents [31]. However, in some application areas such as biosensor

using organic solvents have some drawbacks. For instance, while enzymes are solving in the organic solvent, their structures can be changed and lost their properties [31]. Also, dissolving process or curing process generally need high temperature which can also affect the properties of the enzymes [31]. On the other hand, water based soluble inks may result dissolution of electrode material [31].

Application areas of carbon based inks

Textile

Textile that applied carbon-based ink can be considered as conductive textiles. Conductive textiles mean when applied electricity on textile structure it can conduct electric [32]. Carbon based conductive inks are printed on the textile surfaces and make a conductive pattern by some printing techniques such as doctor blade method, screen printing, ink-jet printing [4], dipping method [33,34], drop casting method [35], or spray coating [36]. Carbon types in the ink and applied carbon amount affect the textile morphological structure and electrical conductivity. Alamer et al. shows SEM images (Figure 1.6) of not coated and coated cotton fabric with PANI/carbon black and he claimed that not coated fabric demonstrated smoother surface instead of coated surface. Moreover, 3.36 wt% concentration of CB coated fabric conductivity is 8.37 k Ω /sq on the other hand 22.66 wt% concentration of CB coated fabric conductivity is 0.494 k Ω /sq [35].

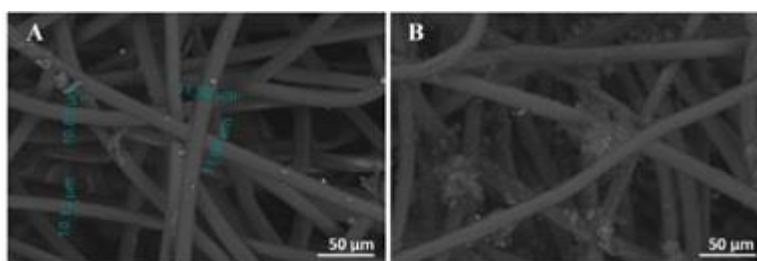


Figure 1.6 : SEM images a) untreated cotton fabric b) the conductive cotton fabric of hybrid PANI/CB at 9.34wt% [35].

According to application areas, carbon types can vary. Manufacturing antenna for satellite communication, graphene based carbon inks can be good alternatives because graphene is biocompatibility, low cost and need low temperature for processing [4]. Carbon nanofibers based inks [37], activated carbon [36], and carbon nanotubes [34] can be used in supercapacitor textile applications. Thangakameshwaran et al. investigated CNT ink dipped cotton fabric morphological, mechanical and electrical

conductivity properties for high-tech uniforms [33]. Pang et al. worked on the microbial fuel cell which contain silver thread and carbon ink as electrodes. Moreover, carbon based coated textiles can be used in a sensor applications [38], waste water treatment [39] and thermoelectric applications [40].

Sensor

A device which transform physical stimulation into an electrical signal is called a sensor [41]. In order to achieve accurate detection of the target molecule or signal, one sensing device needs specific sensitivity, response and recovery time, as well as reproducibility [42]. Carbon-based inks are generally used as a electrode for sensor applications.

The chart in Figure 1.7 shows the classification of the various application areas of carbon based ink sensors.

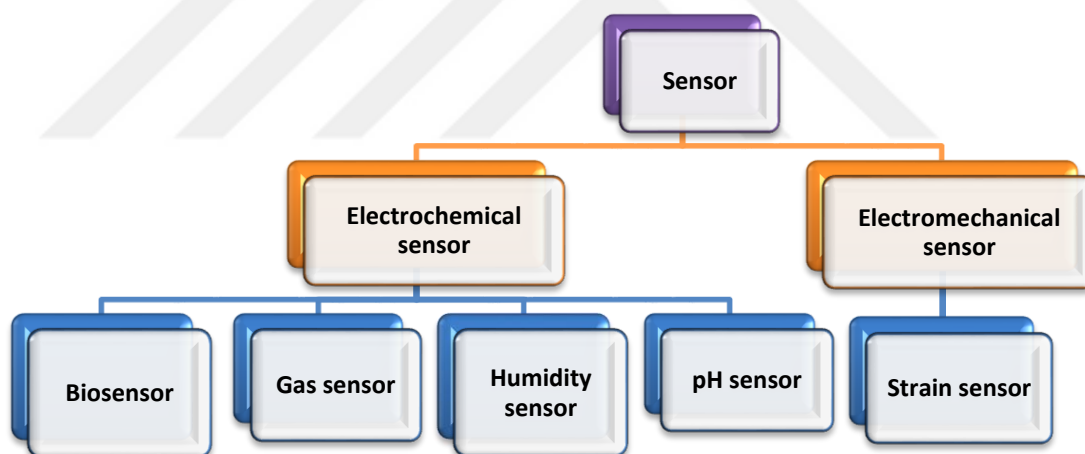


Figure 1.7 : Carbon ink for various sensor applications.

To determine gas, molecules, humidity or pH values electrochemical sensor are used. Carbon based ink electrochemical sensors can be divided in five groups as biosensor, gas sensor, humidity sensor, and pH sensor. Biosensors can transform the biologic data into electric display [43]. Role of the carbon based ink for biosensor application is increase the electrical conductivity to enhance sensor ability. According to literature Chen et al. investigated uric acid values in the human blood with carbon-based ink

electrodes which are working and counter electrodes [44]. Crouch et al. used water soluble screen-printed carbon ink to determine glucose values [31], Dias and co-workers prepared carboxylated carbon nanotubes inks as a working electrode to specify dengue virus NS1 protein which is the vital medical problem in tropical regions [45]. To prevent the enzyme denaturalization meanwhile curing process Wang et al. researched sol-gel enzyme-containing carbon inks which contains graphite powders to determine glucose [46]. Another type of electrochemical sensor is gas sensor. Gas sensor is vital for medical monitoring and food quality control [47]. Conventional gas sensor application suffers from low sensitivity and long response time, however carbon based ink electrodes show high sensitivity and quick response time due to their high electrical conductivity [47]. Humidity sensor is the other type of electrochemical sensor which detect water contamination [48]. In the recent years carbon based especially graphene based inks are aroused attention as a electrode in the humidity sensor application because its morphologic (2D) structure, electrical conductivity, giving response to many materials and high carrier mobility [48]. Moreover carbon based inks are used in the pH sensing device as enhancing electrical conductivity of sensor [49].

Electromechanical sensor converts physical signal to electrical output. Strain sensor is a electromechanical sensor which give response to stress deformation. It is important that strain sensor should be flexible and sensitive to force changes which make them long term and high cycle usable sensor. To improve these properties of strain sensor, carbon based inks can be used. Carbon materials can sense low level stress deformation and show high stability under bending conditions [50].

Bioelectronics

Bioelectronics can be defined as they conduct or give response to biological signals. Biological sensors and medical instruments are main subgroups of these devices [51]. Carbon –based inks are preferred for bioelectronic application because it is convenient for a flexible device. However, carbon-based inks have some disadvantages. For instance, graphene based carbon ink shows high electrical conductivity and biological activity which make hard to control stem-cell spreading and orientation. Moreover, carbon-based inks are generally dissolved in the toxic solvents that prevent them to be used in the medical device [52]. However, recent researches promise hopes to enhance

their stability , control activity and conductivity and to discover new non-toxic homogenous solutions.

Tissue engineering

Tissue engineering has vital importance in the medicine. It can be used as generating organ or modified them. Moreover, because of ethical issues, testing drugs on people and animals are restricted so generated organs or tissues can be used for testing purpose [53]. Improving in technologies give a chance to produce 3D scaffold which they give more accurate results than 2D scaffold. 3-D printing is one of the important technologies to obtain 3D scaffolds. For producing tissues natural polymer based ink and synthetic polymer based ink are may used in 3D printing technologies. However, especially for neural cell scaffolds need to conduct electricity. For this purpose, researchers have started to investigate carbon-based inks. Carbon nanotubes, graphene, carbon fiber etc. based ink in polymer matrix are some carbon-based inks application for enhance scaffolds electrical conductivity properties [53].

Supercapacitor

In industrial devices, renewable energy sector and electrical vehicles applications supercapacitors find a research area due to their high power density, fast cycling and long term life. Electrochemical double layer capacitor (EDLC) , pseudocapacitor and hybrid capacitor are types of supercapacitors. EDLC electrodes type is generally made from carbon, however in the pseudocapacitor electrodes are prepared by redox metal oxide or redox polymer. Moreover, for hybrid supercapacitors carbon can be used as an anode or cathode that depends on types of the hybrid capacitors. When metal oxides are applied alone as an electrode, they may show high resistivity which decrease power density and rate capability, cause to crack on the electrode that decline life cycle of the capacitor and have low surface area and porosity [54]. However, carbon provides high surface area, different pore size distribution, high conductivity, enhance rate capability, good stability and low cost. Carbon black, carbon nanospheres, carbon nanotubes, carbon nanofibers, graphene, carbon foams or sponges based conductive inks improve the properties of supercapacitors [54].

Solar cell

Photovoltaic cell, also called solar cell, transforms light energy to electrical energy [55]. Main structure of the solar cell are showed below Figure 1.8.

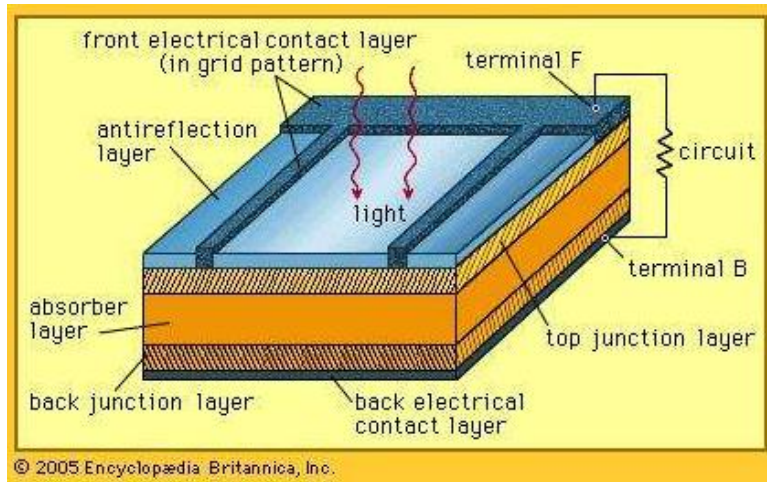


Figure 1.8 : Solar cell structure [55].

General classification of solar cell can be shown as below Figure 1.9.

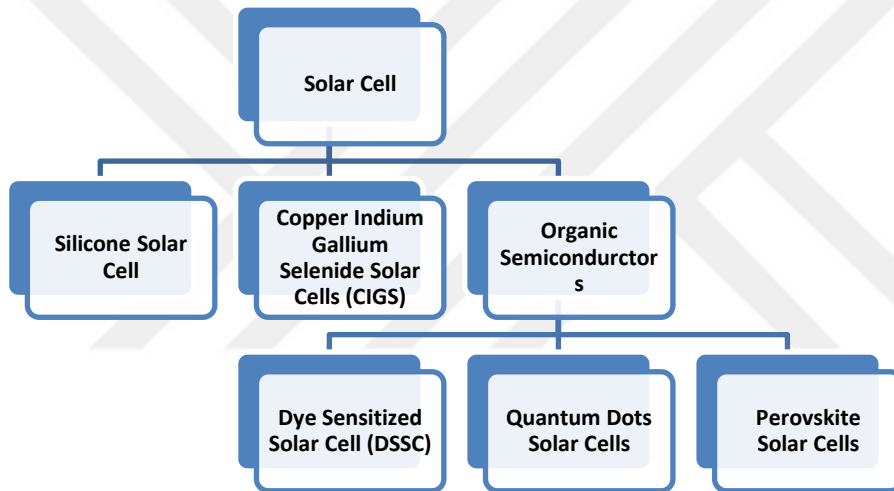


Figure 1.9 : Classification of solar cell.

The history of solar cell based on the crystalline silicone solar cell. Crystalline silicone solar cells are the first generation of the photovoltaic cells which the production process are challenging and limited for the commercialization because of their high cost production process. Second generation of solar cells is produced by amorphous-Si, polycrystalline-Si and CIGS that applied on low cost substrates. Compare to first generation of solar cells second generation solar cells show improved efficiency, however, lack of duplicability and surface uniformity prevent them to commercialize. To overcome all these problems, researchers introduced the third generation of the solar cells. Third generation of solar cells is compatible with flexible materials, has low-cost and easy production process against first and second generation of solar cells [56]. Efficiency results of different solar cells can be seen below Figure 1.10.

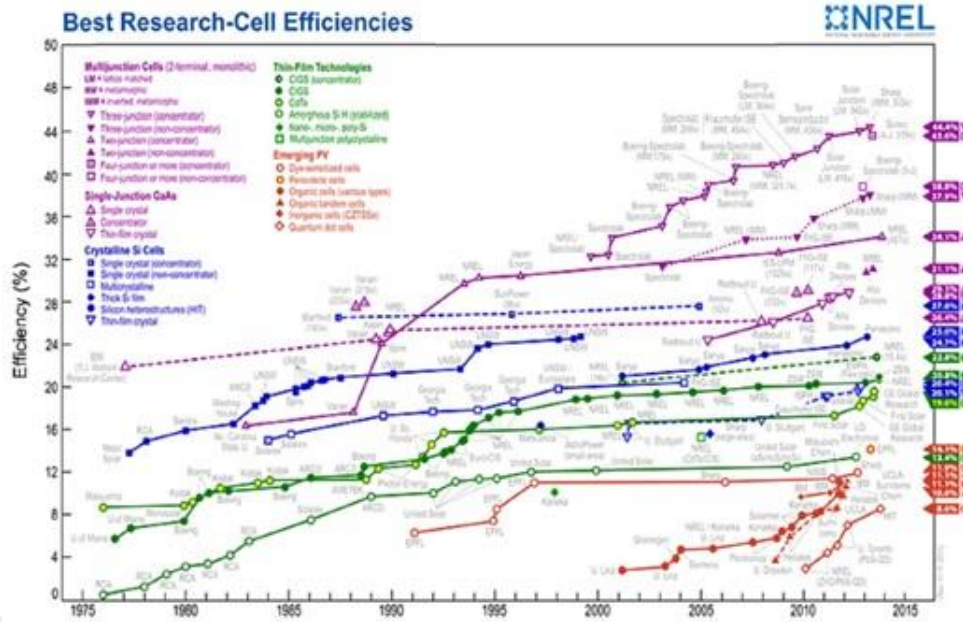


Figure 1.10 : Efficiency diagram of different type solar cells [56].

Perovskite Solar cells

Lev A. Perovski was found the perovskite, however early application of perovskite on the solar cell was done by Miyasaka et al. and reached 3.8% PCE [57].

Structure of a perovskite: Structure of perovskite is shown as below Figure 1.11 and formula of perovskite is ABX_3 , which A and B are various size of cations like A is as $CH_3NH_3^+$ (MA), $HC(NH_2)_2^+$ (FA), Cs^+ and Rb^+ ; B is a metallic cation, such as Pb^{2+} and Sn^{2+} and X is an anion, such as Cl, Br, and I [58].

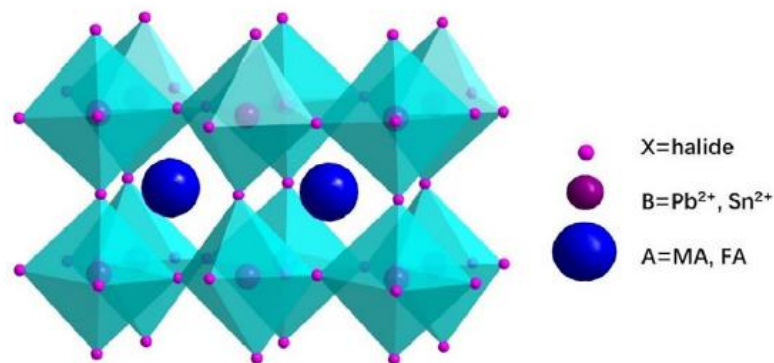


Figure 1.11: Structure of perovskite [58].

Different type of cations and anion can change the electrical and optical properties of the perovskite [58]. The reasons for preference of perovskite for solar cell application are controllable band gap, improved efficiency and effortlessly production process

[59]. However, its degradation and stability problem cause to decrease of perovskite solar cell life time [59].

Perovskite solar cell can be divided in two categories as with hole transporting materials (HTM) and HTM-free.

Perovskite solar cell with HTM: Park et al. investigated a spiro-MeOTAD (2,2',7,7'-tetrakis(N,N-di-p-methoxyphenylamine)-9,9'-spirobifluorene) to enhance the perovskite stability and increase the lifetime of solar cell [60]. They reached the 9% PCE with HTM layer. In recent year, power conversion efficiency of the perovskite solar cell was increased 22% by Yang et al. and co-workers [61].

Perovskite solar cell with HTM consists of well-known four different types of structure (Figure 1.12) [58]. First structure is based on the dye-sensitized solar cell which include FTO/compact-TiO₂ /mesoscopic-TiO₂ /CH₃NH₃PbI₃ /2,2', 7,7'-tetrakis-(N,N -di- p methoxyphenyl-amine)-9,9'-spirobifluorene(spiro-MeOTAD)/Au(metal layer). Second type of structure is made without mesoscopic-TiO₂ which needs to high process temperature. Beginning to use organometal trihalide perovskites in the solar cell, perovskite shows capability to transport holes. In the third structure, p-i-n configuration is used that perovskite ITO/HTM/perovskite/electron transporting layer/metal. Hole transporting layer can be PEDOT:PSS, NiO or MoO₃ and an electron-transport material can be PCBM or ZnO. In the fourth structure, mesoporous material is applied into perovskite [58].

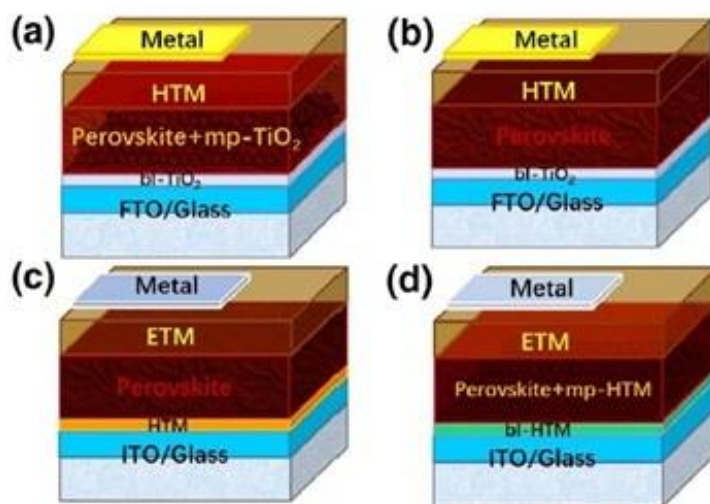


Figure 1.12 : Structures of perovskite solar cell with HTM [58].

HTM-free perovskite solar cell: Hole transport layers which used in perovskite solar cells are expensive and may obstruct the electrons that cause the decrease of the power efficiency of solar cell. Because of these reasons researchers investigated the elimination way of HTM layer. Inherent properties of the perovskites led this process possible due to the fact that perovskite is able to transport of electrons [62].

HTM-free perovskite solar cell can be divided in two categories; Au-based and carbon-based HTM-free perovskite solar cell. However, because of the high cost of Au material carbon structures are more preferred according to their low cost, easy to produce, environmentally friendly, resistivity to chemicals and huge electrical conductivity [62].

Two types of carbon structure (Figure 1.13a) and (Figure 1.13b) may use for the HTM-free perovskite solar cell application that mesoscopic carbon and planar carbon electrode. In the first type, there are three different mesoscopic layer. Mesoscopic TiO₂ behave as an electron transporting layer, m-ZrO₂ act as a spacer layer and m-carbon perform as an hole collector. After these three layer, perovskite are applied and penetrate into these layers. On the other hand, in the planar carbon electrode based perovskite solar cell is formed by m-TiO₂ and perovskite layer under the planar carbon layer. First two layer of FTO and compact TiO₂ are same for both mesoscopic and planar carbon-based perovskite solar cell. Moreover, spacer layer in the m-carbon-based perovskite solar cell separates the m-TiO₂ and m-carbon to prevent the short circuit. However, for the planar carbon-based solar cell thick perovskite layer assumes to hinder short circuit [62].

According to conduction and valance band edges values, solar cell working principle can be explained in Figure 1.13c). m-TiO₂ conduction band edge is -4.0 eV, perovskite CBE is -3.9 eV and valance band edges is -5.4 eV and the carbon has -5.0 eV VBE. When the perovskite layer is exposed to light, because of its ambipolar nature it produces both electrons and holes. Electrons move to lower CBE level which means from perovskite CBE to m-TiO₂ CBE and holes pull out to higher VBE from perovskite VBE to carbon VBE [62].

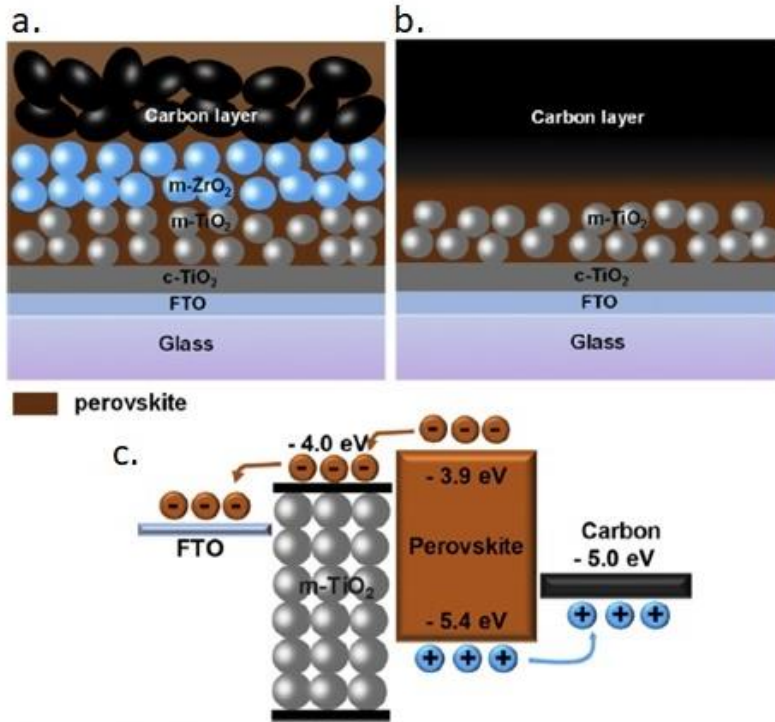


Figure 1.13 : HTM-free perovskite solar cell with a) m-carbon b) p-carbon structure. c) Working principle of the perovskite solar cell with carbon electrode [62].

According to literature Han et al. was the first time announced the m-carbon electrode application in the perovskite solar cell (Figure 1.14). They improved the carbon black/spheroidal graphite CE instead of the flaky graphite and reached the 6.4% PCE [63]. Moreover, they improved PCE to 12.84% by using (5-AVA)_x(MA)_(1-x)PbI₃ with carbon electrode [64] and applied the same structure for commercial size of solar cell module (10*10 cm²) which gave the more than 10% PCE [65].

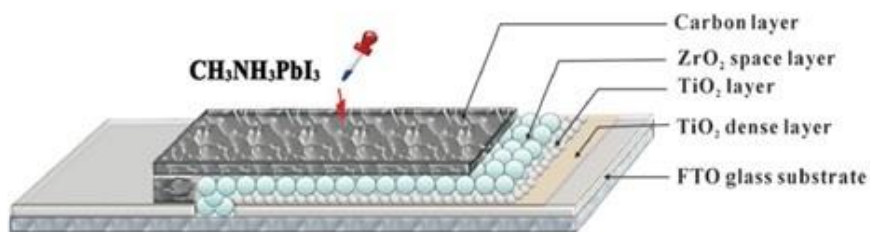


Figure 1.14 : m-carbon based perovskite solar cell [63].

Liu et al. studied on reducing carbon counter electrode thickness, therefore, instead of traditional carbon black/graphite CE they used SWCNT/NiO layer with approximately

1.8 μm thickness. The configuration of the solar cell (Figure 1.15) is FTO/TiO₂/Al₂O₃/NiO/SWCNT(MAPbI₃). They reached the 12.7%, 10.5% and 6.2% with 1.8 μm -thick NiO/SWCNT, 10 μm -thick carbon black/graphite and 1.8 μm -thick carbon black/graphite layer, respectively [66].

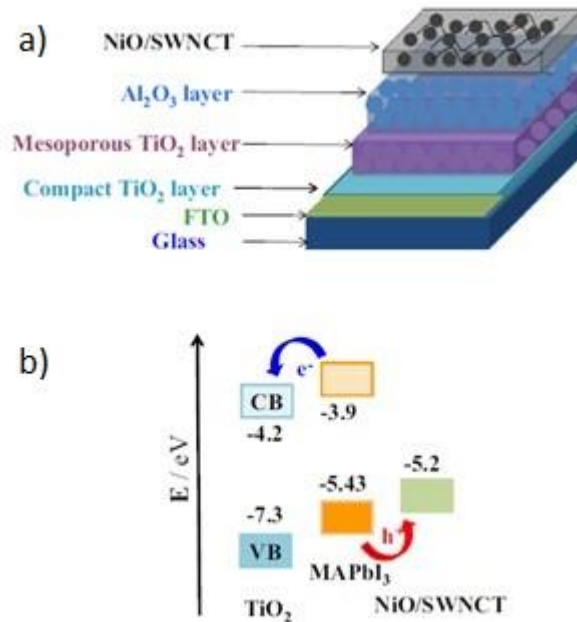


Figure 1.15 : a) Configuration b) working principle of the perovskite solar cell [66].

Duan et al. compared the efficiency of carbon black/graphite CE and carbon black/ultrathin graphite CE on the mesoporous perovskite solar cell. CB/Ultrathin graphite CE based perovskite solar cell has 22.97 mA/cm² J_{sc}, 901 mV V_{oc}, 0.68 FF and 14.07% PCE. However, CB/graphite CE based perovskite solar cell gave 22.89 mA/cm² J_{sc}, 893 mV V_{oc}, 0.62 FF and 12.63% PCE. They claimed that because of the high surface area of the ultrathin graphite, hole collection capability was increased while charge transfer resistance was decreased in the carbon counter electrode which improved efficiency of the perovskite solar cell [67].

Jiang et al. prepared low temperature carbon electrode based on graphite, CB, a-terpineol, Titanium (IV) isopropoxide (TTIP) and acetic acid (Hac). They applied carbon ink at 70°C and 400°C on a glass and PET surface. Low temperature ink showed higher conductivity compared to high temperature conductive carbon ink. Moreover, in solar cell application, the perovskite solar cell which contains both high temperature carbon electrode and low temperature carbon electrode enhanced PCE of 1.2% and get 14.04% PCE [68].

Yue et al. studied on the how carbon black and graphite percentage affect on the low temperature carbon ink resistivity and perovskite solar cell efficiencies. They used ethyl cellulose as a binder and isopropyl alcohol as a solvent media. Carbon inks with 0% of graphite and 0% of CB decline the power efficiencies of solar cells and also increase the resistivity of conductive inks. However, they found that 75wt% graphite and 25wt% carbon black enhanced a conductivity of carbon ink and improve the PCE to 7.29% [69].

Tao et al. tried to enhance permeability of the carbon electrode cause to improve the penetration of perovskite layer into solar cell. Polystyrene spheres were added into high temperature carbon ink with different ratios and conductivity of carbon ink and photovoltaic performance of perovskite solar cell were investigated. Adding polystyrene spheres increased the carbon ink resistivity. On the other hand, optimum ratios of polystyrene sphere addition increased solar cell average efficiency 3.36% to 4.10% because at 400°C polystyrene spheres decomposed and formed channels in the carbon electrode [70].

Mali et al. inserted methylammonium lead iodide (MAI) into the commercial carbon ink and organized perovskite solar cell structure as a Glass/FTO/mp-TiO₂/MAPbI₃-xCl_x/carbon+MAI/Carbon. The photovoltaic properties of the solar cell are 13.87% power conversion efficiency (PCE) with open circuit voltage (VOC) 0.997 V, current density (JSC) 21.41 mA/cm² and fill factor (FF) 0.65. They also claimed that improved carbon layer with solar cell also showed water resistivity and air stability [71].

Gopi et al. investigated the production method and clamping effect on the solar cell efficiency with single wall carbon nanotubes carbon CE. They studied on three different method which can be seen from Figure 1.16. In the first method, they applied the carbon CE on the FTO then clamped the solar cell. In the second method, carbon counter electrode was printed on the CH₃NH₃PbI₃ layer by doctor blade method and then FTO was clamped on the CE. In the final method, SWCNT ink was applied on to th PbI₂ layer, perovskite was coated with spin coating method and for final step FTO put onto solar cell. They obtained 7.83% PCE while Voc is 0.703V, Jsc is 18.54 mA/cm² and FF is 0.60 with exceed stability over 50h [72].

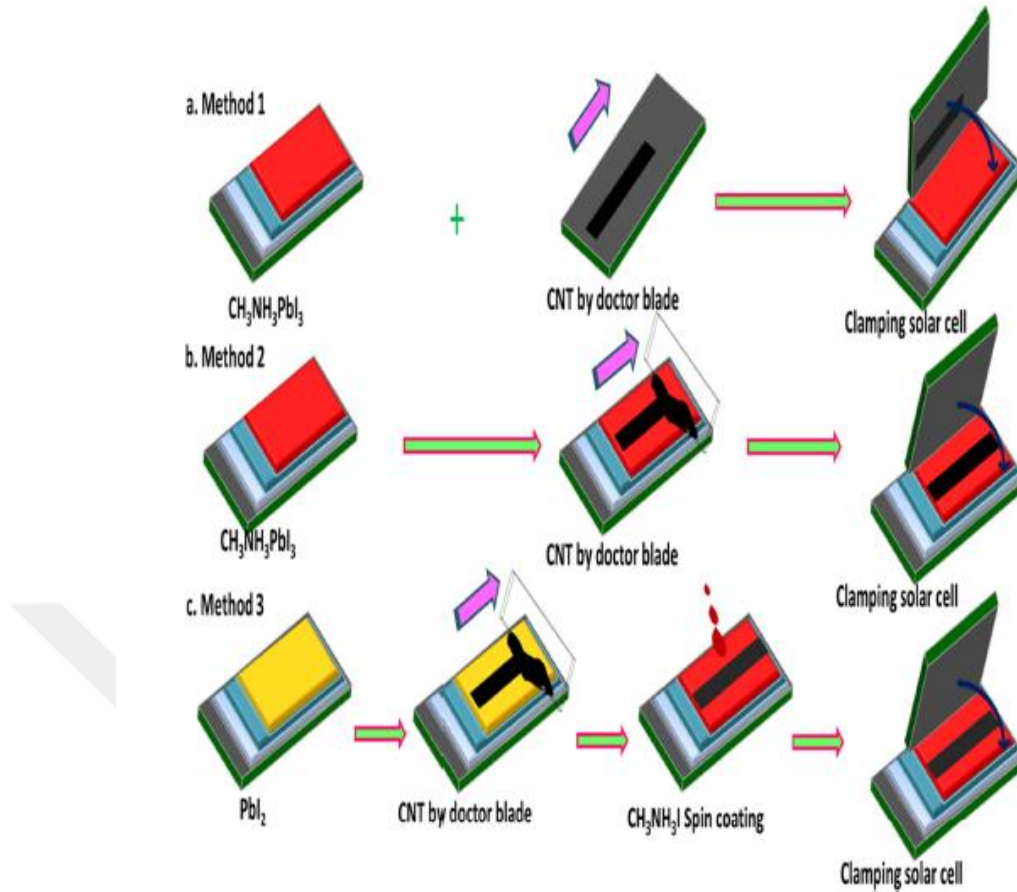


Figure 1.16 : Carbon electrode a) with printed on the FTO and clamping b) printed on the perovskite and clamping c) printed on the PbI_2 [72].

Zhang et al. used graphene/functional carbon nanotubes in DMF solution as a hole transporting layers in the perovskite solar cell. The configuration of the solar cell is ITO/HTLs/Perovskite/PC61BM/Ag and they obtained 14.8% PCE with high stability [73].

Chu et al. improved the drying process of the carbon electrode by using gas pump to get uniform surface area. They applied commercial carbon paste onto the perovskite layer with screen printed method then dried at 100°C under 100 Pa. Photovoltaic properties of the solar cell are 12.30% PCE with open circuit voltage is 1.03 V, J_{sc} is 21.4 and FF is 0.56 [74].

Liu et al. brought a new perspective to the carbon electrode based perovskite solar cell application as shown as below Figure 1.17. They banded together thermoelectric device and perovskite solar cell. During electricity production in solar cell perovskite temperature increases by light and that cause the degradation of the perovskite. To prevent this, Liu and co-workers treated thermoelectric device with ice bed which also

Electrical resistivity is multiply of the electrical resistance (R) and the cross-sectional area (A) to the length of the material (l);

$$\rho = \frac{RA}{l} \quad (1.2)$$

Electrical conductivity is related with the band electrons or holes in material and in electrolytes it is about the concentration of ions and movements [78]. Silver, copper and gold are most conductive materials respectively [79]. Because its about their crystal structure and valance which provide electron movement freely [79]. Some materials conductivity and resistivity are shown in Table 1.1

Table 1.1: Resistivity and conductivity of some materials at 20 °C [80].

Material	Resistivity ρ ($\Omega \cdot m$)	Conductivity σ (S/m)
Silver	1.59×10^{-8}	6.30×10^7
Copper	1.68×10^{-8}	5.96×10^7
Annealed copper	1.72×10^{-8}	5.80×10^7
Gold	2.44×10^{-8}	4.10×10^7
Aluminum	2.82×10^{-8}	3.5×10^7
Calcium	3.36×10^{-8}	2.98×10^7
Tungsten	5.60×10^{-8}	1.79×10^7
Zinc	5.90×10^{-8}	1.69×10^7
Nickel	6.99×10^{-8}	1.43×10^7
Lithium	9.28×10^{-8}	1.08×10^7
Iron	1.0×10^{-7}	1.00×10^7
Platinum	1.06×10^{-7}	9.43×10^6
Tin	1.09×10^{-7}	9.17×10^6
Carbon steel	10^{10}	1.43×10^{-7}
Lead	2.2×10^{-7}	4.55×10^6
Titanium	4.20×10^{-7}	2.38×10^6
Grain oriented electrical steel	4.60×10^{-7}	2.17×10^6
Manganin	4.82×10^{-7}	2.07×10^6
Constantan	4.9×10^{-7}	2.04×10^6
Stainless steel	6.9×10^{-7}	1.45×10^6
Mercury	9.8×10^{-7}	1.02×10^6
Nichrome	1.10×10^{-6}	9.09×10^5

Table 1.1(continued) : Resistivity and conductivity of some materials at 20 °C [80].

GaAs	5×10^{-7} to 10×10^{-3}	5×10^{-8} to 10^3
Carbon (amorphous)	5×10^{-4} to 8×10^{-4}	1.25 to 2×10^3
Carbon (graphite)	2.5×10^{-6} to 5.0×10^{-6} //basal plane 3.0×10^{-3} \perp basal plane	2 to 3×10^5 //basal plane 3.3×10^2 \perp basal plane
Carbon (diamond)	1×10^{12}	$\sim 10^{-13}$
Germanium	4.6×10^{-1}	2.17
Sea water	2×10^{-1}	4.8
Drinking water	2×10^1 to 2×10^3	5×10^{-4} to 5×10^{-2}
Silicon	6.40×10^2	1.56×10^{-3}
Wood (damp)	1×10^3 to 4	10^{-4} to 10^{-3}
Deionized water	1.8×10^5	5.5×10^{-6}
Glass	10×10^{10} to 10×10^{14}	10^{-11} to 10^{-15}
Hard rubber	1×10^{13}	10^{-14}
Wood (oven dry)	1×10^{14} to 16	10^{-16} to 10^{-14}
Sulfur	1×10^{15}	10^{-16}
Air	1.3×10^{16} to 3.3×10^{16}	3×10^{-15} to 8×10^{-15}
Paraffin wax	1×10^{17}	10^{-18}
Fused quartz	7.5×10^{17}	1.3×10^{-18}
PET	10×10^{20}	10^{-21}
Teflon	10×10^{22} to 10×10^{24}	10^{-25} to 10^{-23}

Electrical conductivity can be affected by different parameters [79], such as:

Temperature: Generally increasing temperature, decline the conductivity of the materials because of the thermal excitation of the atoms.

Impurities: Impurities prevent the electron flow and decrease the conductivity.

Crystal structure and phases: Different phase and crystalline structure of material can show variable resistivity. For example, graphite and diamond have same element carbon but their structures and bond types are different from each other which cause to graphite is a conductive material and diamond is a insulator material.

Electromagnetic fields: While conductors allow to flow electrical current, they also produce magnetic fields which is perpendicular the electrical field. If external

magnetic field is applied to the conductor, magnetoresistance will occur and may decrease the conductivity of the material.

Frequency: At high frequency, the skin depth is getting smaller to cause the increase of electrical resistance of the material which hinder or slow down the flow of current.

1.2.2.1 Electronic conductivity

Electronic conductivity means electrical charge is carried by electrons and holes in the material [81]. Especially in solid conductors such as metals and semiconductors use this principle to conduct electricity.

Band theory: In solid-state physics, band theory can be described as electrons stay at specific range of energy. Allowed band and forbidden band are which the energy ranges of electron can be exist and the range of between two allowed bands, respectively. In the forbidden band electrons couldn't have this energy. The electronic and thermal behavior of materials depend on band theory [82].

Valance band: Atoms comprise of discrete allowed energy levels and when atoms get together and form a solid, this quantum mechanical effect is occurred because of discrete energy levels. Electrons fill up some energy bands which is named as a valance band [82].

Conduction band: Empty energy levels which are not occupied by electrons are called conduction band [82].

Fermi level: Fermi level is the highest energy level of electrons at absolute zero temperature. Due to the Pauli exclusion principle fermions can't stay at same energy level so at absolute zero temperature they form a Fermi sea which is the lowest energy state electrons can exist [83].

In insulator, there is a huge energy gap between the conduction band and valance band, so electrons could not rise up to the conduction band. In semiconductors, energy gap between is smaller than the insulators so electrons can jump to the conduction band. In conductors, here is not any energy gap between the valance band and conduction band hence electrons can reach the conduction band easily [84]. The demonstration of energy gap between conduction band and valance band for insulator, semiconductor and conductor materials can be seen from below Figure 1.18.

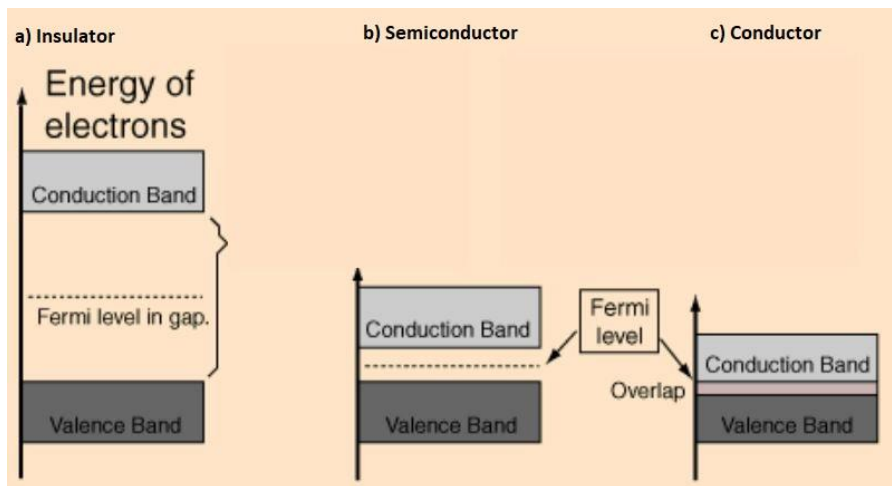


Figure 1.18: Illustration of conduction and valance band of a) insulator b) semiconductor c) conductor [84].

1.2.2.2 Ionic conductivity

Ionic conductivity occurs with movement of ionic charge in the liquid electrolyte solution. Ionic conductivity can be expressed as product of the carrier charge (q), the concentration (n), and the mobility (b) which gives the specific conductivity [85].

$$\sigma = qnb \quad (1.3)$$

In electrochemistry, ionic mobility is equal to λ_i ;

$$\lambda_i = \frac{\sigma_i}{|Z_i|c_i} = Fb_i \quad (1.4)$$

where c_i is the molar concentration, Z_i is the charge number and F is the Faraday's constant. The total ionic conductivity is;

$$\sigma = \sum q_i n_i b_i = \sum |Z_i| c_i \lambda_i \quad (1.5)$$

1.3 Hypothesis

Conductive inks such as metal-based, polymer-based and carbon-based are preferred when high conductive materials are need. However, compared to polymer-based conductive ink, metal- and carbon-based conductive inks exhibit enhanced conductivity. Moreover, carbon-based ink is less expensive than metal-based ink, plus carbon is more abundant in environment. Carbon-based conductive ink can be used for solar cell application. However, this type of ink may be prepared and applied at both, high and low temperatures. Low temperature-based ink has advantages because it requires low energy demand and easier application process. Moreover, it is used for wide range of commercial applications.

2. EXPERIMENTAL TECHNIQUES & METHODS

In this chapter, experimental techniques and methods which were used in this thesis will be discussed.

2.1 Experimental Techniques

Experimental techniques that were used in this thesis can be divided as in three main group which are material characterization, photovoltaic device fabrication techniques and photovoltaic performance evaluation techniques.

2.1.1 Material characterization

To determine carbon particles and carbon inks morphological and physical properties SEM and BET method were used. For resistivity measurement of inks four-point probe technique was preferred.

2.1.1.1 Scanning electron microscope (SEM)

Scanning electron microscopy (SEM) (Figure 2.1) consists of two main components as microscope column which comprises filament, electron gun, electron beam, electron lenses, scan coil, specimen stage, electron detector and if it exits specimen and control console that consists viewing screens, camera and control keyboard. The major function of electron gun and lenses generate electrons and generated electrons are accelerated between 0.1-30 keV. Electron beam pass through the lenses and collect in the specimen chamber to irradiates specimen. Moreover, it produces signals from specimen to create image. Scan coils move the beam and adjust the magnification of scanning. When beam irradiates specimen, backscattered and secondary electrons signals are occurred and detector system collect them point-by-point to produce an image. While camera records the image, from viewing screen image can be seen [86].

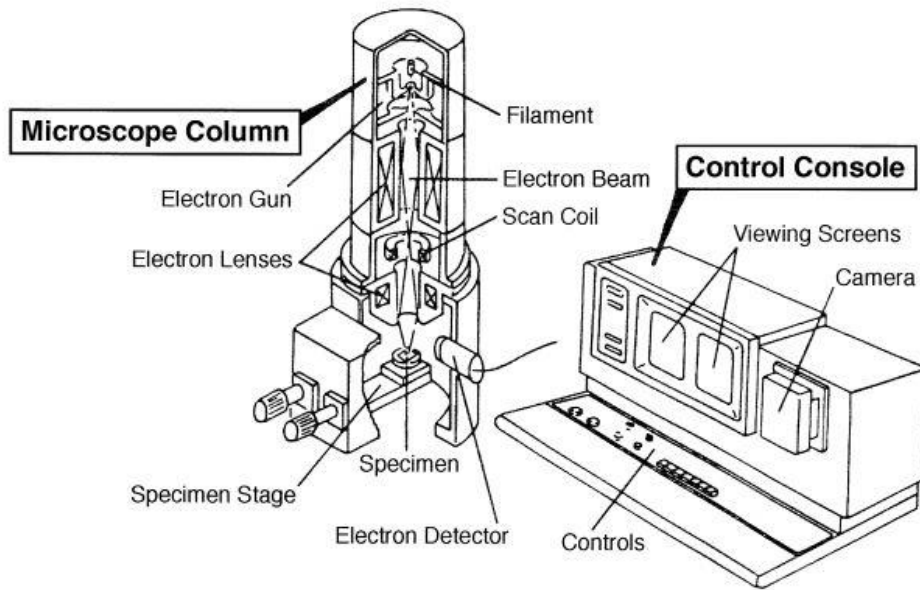


Figure 2.1 : Main components of SEM [86].

In this thesis, SEM device was used for investigation of carbon inks morphology and surface properties in resolution mode and electrons were accelerated with 15 kV by TESCAN Vega3. Moreover, EDAX program was used for determined the element contents and distributions.

2.1.1.2 BET analysis

Brunauer–Emmett–Teller (BET) theory measures the specific surface area of materials by the absorption of gas molecules on a porous materials. For this purpose nitrogen is the most using gases in BET analyses. The BET equation is [87];

$$\frac{1}{W[P/P_0-1]} = \frac{1}{W_m C} + \frac{C-1}{W_m C} \left(\frac{P}{P_0} \right) \quad (2.1)$$

The BET plot is shown in Figure 2.2

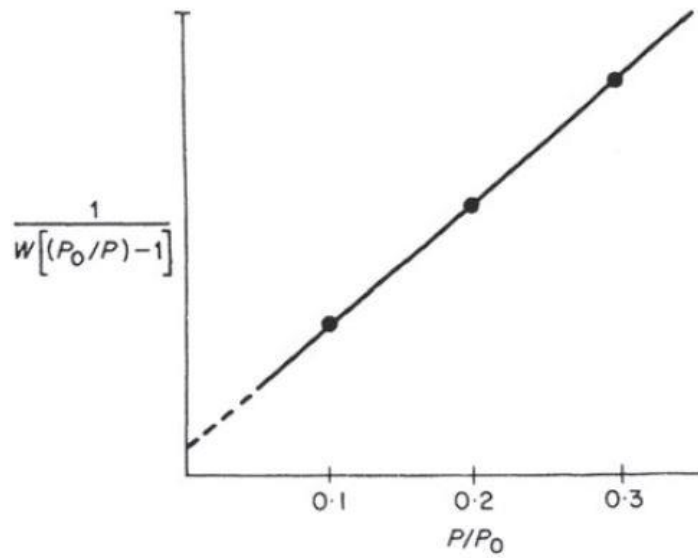


Figure 2.2 : BET plot [87].

The slope s ;

$$s = \frac{C-1}{W_m C} \quad (2.2)$$

The intercept i ;

$$i = \frac{1}{W_m C} \quad (2.3)$$

The weight absorbed in monolayer W_m ;

$$W_m = \frac{1}{s+i} \quad (2.4)$$

BET constant C ;

$$C = \frac{s}{i} + 1 \quad (2.5)$$

Total surface area can be calculated as;

$$S_t = \frac{W_m N A_x}{M} \quad (2.6)$$

where,

A_x = the cross-sectional adsorbate area,

M = the adsorbate molecular weight,

N = Avogadro's number

2.1.1.3 Four-point probe method

In the four-point probe measurement technique (Figure 2.3) basically four equally positioned tips contact with the sample. A DC current is applied from 1 and 4 probes and inner probes 2 and 3 measure the voltage differences on the sample surface [88].

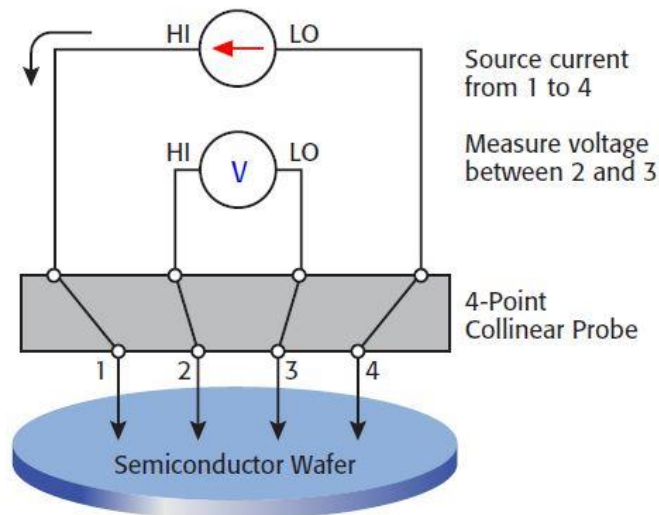


Figure 2.3 : Four-point probe test circuit [88].

The bulk (volume) resistivity (ρ) can be measured from below equation;

$$\rho = \frac{\pi}{\ln 2} \frac{V}{I} t k = 4.532 \frac{V}{I} t k \quad (2.7)$$

ρ = the bulk resistivity (Ω -cm),

V = the measured voltage (voltage),

I = the magnitude of the source current (amps),

t = the sample thickness (cm)

k = a correction factor

For thin materials such as films or coatings, thickness is not calculated that gives the sheet (surface) resistivity of the material. The sheet resistance (σ) is measured as below,

$$\sigma = \frac{\pi}{\ln 2} \frac{V}{I} k = 4.532 \frac{V}{I} k \quad (2.8)$$

σ = sheet resistance (Ω /square or just Ω)

V = the measured voltage (voltage),

I = the magnitude of the source current (amps),

t = the sample thickness (cm)

k = a correction factor

In my thesis, four-point probe measurement technique was studied for measuring the carbon inks resistivity by the Model 2450 SourceMeter SMU Instrument with 10.0 mA ampere source and 21.0V voltage limit.

2.1.2 Photovoltaic device fabrication technique

2.1.2.1 UV-Ozone cleaning

UV-Ozone cleaning system is easy, less expensive and effective to remove contaminants from the surface of substrate [89]. The mechanism of the system (Figure 2.4) is, first using ultraviolet rays oxygen is turned into ozone, then generated ozone produce oxygen to absorb 253.7 nm and above ultraviolet rays and finally decomposition occur between organic compound and unstable oxygen [90].

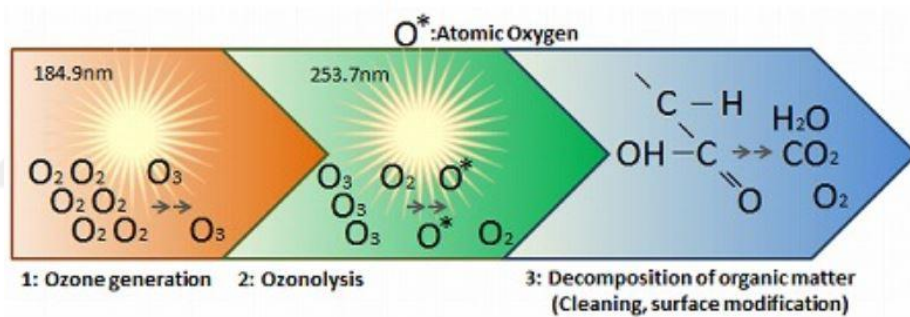


Figure 2.4 : Mechanism of UV/Ozone cleaning system [90].

2.1.2.2 Spin coating

Spin coating is generally used for forming a thin film with thickness of micrometer or nanometer [91]. The mechanism (Figure 2.5) of the method benefits from centrifugal forces. First, solution is deposited on the spin coating system substrate, then substrate starts to rotate in high speed, the result of rotation in high speed air flow is formed and helps drying solvent [92].

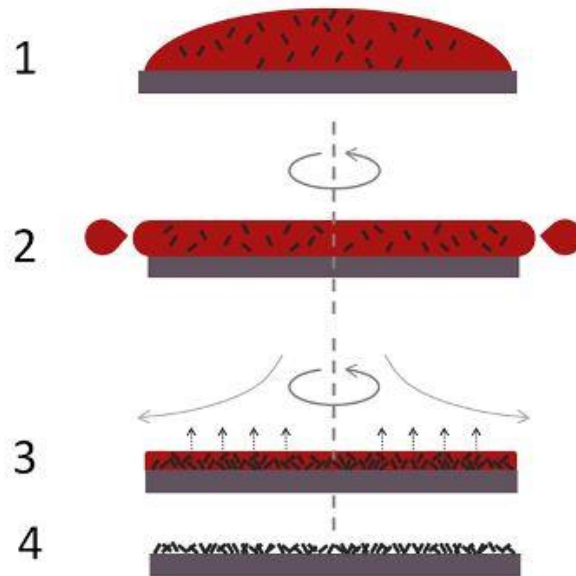


Figure 2.5 : Spin coating mechanism [92].

2.1.2.3 Doctor blading

One of the simple and inexpensive method to produce thin film is doctor blading technique. It is based on solution or slurry is placed beyond the blade and blade spread it with constant speed to form a thin film. Thickness of thin film can be obtained with different micrometers which rely on doctor blade height and geometry, coating speed, solution surface tension and rheological properties. Doctor blading method can be divided in two main categories depend on coating device; doctor blade (frame) (Figure 2.6) and a spiral film applicator (Figure 2.7) [93].

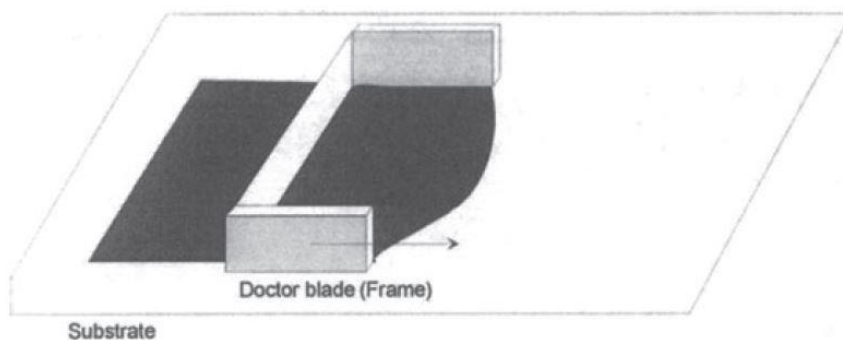


Figure 2.6 : Doctor blading technique with frame apparatus [93].

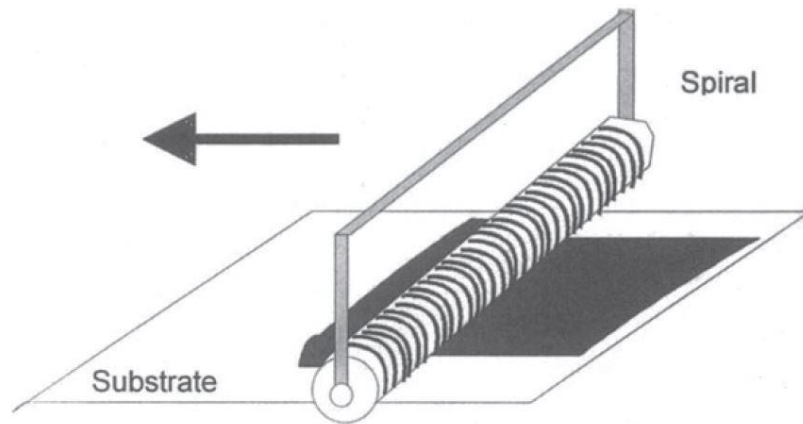


Figure 2.7 : Doctor blading technique with spiral aperture [93].

2.1.2.4 Vacuum thermal evaporation

Vacuum thermal evaporation is generally used for metal coating on the organic thin film for perovskite solar cells. The technique (Figure 2.8) basically consists of source, substrate and vacuum evaporator [94]. When the source is heated, atoms or molecules separate from source and they start to travel in the chamber. While heated atoms and molecules are travelling they hit the substrate and transfer their energy to the lower energetic substrate for stabilize themselves and adhere the substrate. Thickness of the deposition layer depends on the evaporation rate, the geometry of the source and the substrate, and the evaporation time [95].

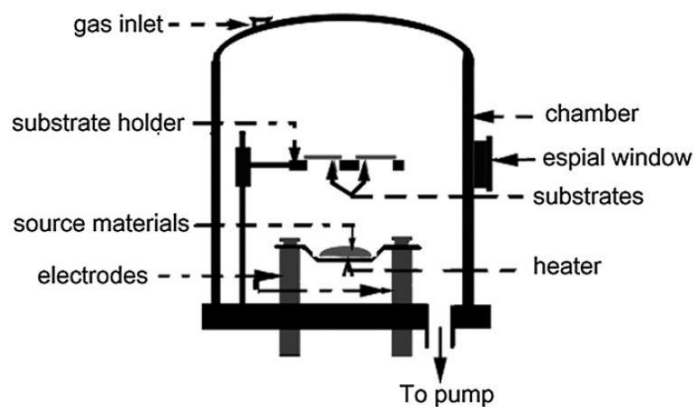


Figure 2.8 : Schematic illustration of vacuum evaporation method [94].

2.1.3 Photovoltaic performance evaluation

2.1.3.1 Solar simulator

Solar simulator illuminate the natural sunlight. Sunlight irradiate the Earth with different intensity because of they are affected by different conditions while reaching

the Earth. Sunlight radiation on the Earth can be divided in two main groups; direct radiation which is emitted sunlight directly from the Sun and scattered radiation which consists passing lights from sky and reflected from the ground. Solar simulators can be applied for different spectral distribution of sunlight by using xenon arc lamp source and Air Mass (AM) filters [96]. Different type of solar spectrum and filters are shown in below Table 2.1.

Table 2.1 : Type of solar spectrum and filters with power density and transmission capacity [96].

Solar Spectrum	Filter	Power Density (mW/cm ²)	Transmission %
In Space	AM0	137	61.3%
Direct solar spectrum at 0° zenith angle	AM1.0D	104	67 %
Global solar spectrum at 0° zenith angle	AM1.0G	100	66.7%
Direct solar spectrum at 48.2° zenith angle	AM1.5D	93	65%
Global solar spectrum at 48.2° zenith angle	AM1.5G	100	58.5%
Direct solar spectrum at 60.1° zenith angle	AM2.0D	71	57.3%

2.1.3.2 Current-voltage (JV) curves and power conversion efficiency (PCE)

In basic solar cell application circuit (Figure 2.9) consists of output current (I), diode current (I_D), shunt current (I_{SH}), series resistor (R_S) and shunt resistance (R_{SH}). The circuit current can be illustrated as [97] ;

$$I = I_L - I_D - I_{SH} \quad (2.9)$$

To measure the photovoltaic performance of the solar cells, voltage is applied and IV curves give data about performance of the solar cell.

Open circuit voltage (V_{OC}): The maximum voltage can be obtained from solar cell without any loading [97].

Short circuit current (I_{SC}): The maximum current of the solar cell under zero resistance [97].

Fill factor (FF): It can be defined as maximum power from solar cells [97].

$$FF = \frac{V_{max} * I_{max}}{V_{oc} * I_{sc}} \quad (2.10)$$

Power conversion efficiency (PCE): It illustrates efficiency of solar cells [97].

$$PCE = \frac{I_{sc} * V_{oc} * FF}{P_{light}} \quad (2.11)$$

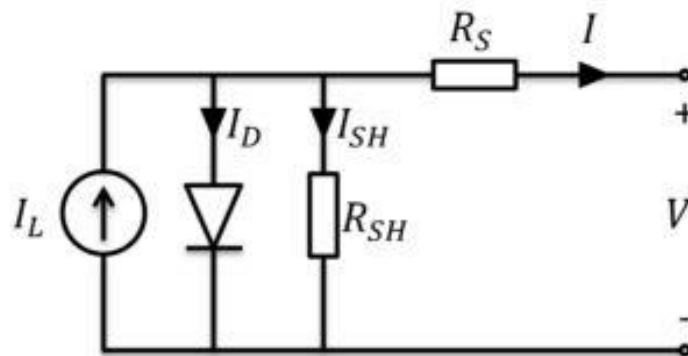


Figure 2.9 : Solar cell circuit diagram [97].

2.2 Experimental Methods

2.2.1 Materials

Espresso machine coffee was purchased from local firm in Turkey, graphite particles (40nm and 5 μ m), Carbon powder (50nm), ZrO₂ (40-50nm) were purchased from SATNANO Technology Material Co. Ltd., China and ethocell Standard 10 Industrial was purchased from DOW.

Ethyl Acetate (99,5%) was purchased from Tekim Kimya Sanayi Tic. Ltd. Sti, PVDF (copolymer) was purchased from Kynar LBG, chlorobenzene (>99%), DMF, ZnCl₂ (>98%) and AgNO₃ (crystal extra pure) were bought from Merck, Ag nanoparticles (99%, 150-190nm) was purchased from Nano Technology Inc., Korea, FTO glass were purchased from Teknoma and TiO₂ paste was purchased from Dysol and Ti(OPr)₂ (acetylacetonate)₂, PbI₂ and HI %wt 57 were purchased from Sigma-Aldrich.

2.2.2 Methods

2.2.2.1 Preparation of carbon-based conductive ink

Firstly, 10wt% ethocell and 2,5wt% polyvinylidene fluoride(PVDF) copolymer were separately dissolved in the ethyl acetate at 80° C. Then, 0,5 gram graphite 40 nm, 0,258g carbon black (CB), 0,258 g graphite 5µm and 0,121g ZrO₂ nanoparticles were measured and mixed. For solvent media 6,06 g chlorobenzene was used and all ingredients were put together. On magnetic stirrer, carbon ink was mixed for two days with 300 rpm.

2.2.2.2 Preparation of environmentally friendly carbon-based conductive ink

In this research, espresso machine coffee and Turkish coffee wastes were used for carbonization process. First, coffee wastes were dried at 100° C to evaporate humidity. Then, dried coffee wastes treat with ZnCl₂ with different ratios, added sufficient distilled water and stayed at rest for 4 hours. 4 different ratios and type of solution was prepared. Machine coffee- ZnCl₂ ratio is 1:1 (MC), Turkish coffee- ZnCl₂ ratio is 1:1 (TC 1:1), Turkish coffee- ZnCl₂ ratio is 2:1 (TC 2:1) and Turkish coffee- ZnCl₂ ratio is 1:2 (TC 1:2). All samples were dried again at 100° C. To obtain carbon, all dried samples were treated at 900° C for 1 hour with 5° C/min heating rate in tubular furnace separately. After carbonization all samples were grinding by manual and for getting smaller size distilled water added samples grinded by ball miller with 400 rpm for 24 hours.

Carbon inks were prepared as described in Chapter 2.2.2.1 with different amounts of coffee waste carbon, as shown in Table 2.2.

Table 2.2 : Illustration of type of coffee waste carbon and denotation.

Type of coffee waste carbon	Weight ratio of Coffee waste carbon	Weight ratio of Graphite 5 μ m, CB, and graphite 40nm	Denotation
MC 1:1	30	70	MC 30/70
TC 1:1	30	70	TC 1:1 30/70
TC 2:1	30	70	TC 2:1 30/70
TC 1:2	30	70	TC 1:2 30/70
TC 1:2	10	90	TC 1:2 10/90
TC 1:2	50	50	TC 1:2 50/50

2.2.2.3 Preparation of doped polymer carbon-based conductive ink

Firstly, 2,5wt% polyvinylidene fluoride(PVDF) copolymer and different ratios of Ag (0.25 mM, 0.50 mM, 0.75 mM and 1.0 mM) and AgNO₃ (0.25 mM, 0.50 mM, 0.75 mM and 1.0 mM) were separately dissolved in the ethyl acetate at 80° C. Then, 10wt% ethocell was dissolved in the ethyl acetate at 80° C. 0,5 gram graphite 40 nm, 0,258g carbon black (CB), 0,258 g graphite 5 μ m and 0,121g ZrO₂ nanoparticles were measured and mixed. For solvent media 6,06 g chlorobenzene was used and all ingredients were put together. On magnetic stirrer, carbon ink was mixed for two days with 300 rpm at 60° C.

2.2.2.4 Preparation of perovskite solar cell

Firstly, FTO glass substrates were covered with band mask. Uncovered areas were etched with Zn and HCl solution. After etching process, they were ultrasonicated in water detergent mixture, water, ethanol, acetone and IPA, respectively. Later, washed substrates were cleaned with UV ozone for 15 minutes. Then, one drop (aprox. 1 ml) 0.1M Ti(OPr)₂(acetylacetonate)₂ /ethanol solution was applied by spray pyrolysis at 450° C in order to obtain TiO₂ compact layer.

Perovskite solution was prepared using the following procedure: 12 ml HI (57wt%) and 24 ml CH_3NH_2 (33wt% ethanol) were mixed with 100 ml ethanol for two hours in ice bath. Liquid part of the solution was removed by rotary evaporation and MAI was synthesized. MAI was washed with diethyl ether three times and crystallized in ethanol. Then it was dried in vacuum oven and white MAI crystals were obtained. MAI and PbI_2 were mixed in 1:1 molar ratio in DMF in order to obtain 40wt% perovskite solution.

To obtain mesoporous TiO_2 layer, TiO_2 paste (18 NRT Dysol) was diluted with ethanol as a mass ratio of 1:6 and deposited on the compact TiO_2 layer by spin coating at 5000 rpm for 30s. Four different annealing temperature were applied at 80° C, 125° C, 325° C and 500° C for 30 min each one, and cooled down to room temperature. Samples were put into glovebox and covered with perovskite by two steps spin coating at 500 rpm/3 seconds and then 4000 rpm/7 seconds. To improve homogeneity and surface distribution of perovskite layer, approximately 100 μl chlorobenzene was dropped onto perovskite layer by spin coating at 4000 rpm 2 sec.. Covered glasses were kept on heater at 100° C for 10 min and then cooled down on a metal surface. As last step of production, carbon counter electrode was applied by doctor blade method onto the perovskite layer.

3. RESULTS AND DISCUSSION

3.1 Properties of Low Temperature Processable Carbon Based Inks

Low temperature carbon based ink was applied on the FTO substrate with different thickness by doctor blading method. The Figure 3.1 shows real images of carbon ink applied on FTO. They confirm that proper surface was obtained from the carbon ink. Optic microscope images on Figure 3.2 from films with different thicknesses also prove the regular surface. Moreover, increasing thickness of the film improves the surface smoothness.

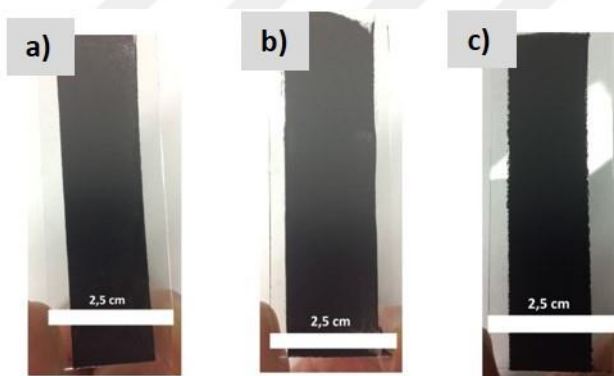


Figure 3.1 : Images of the low temperature processable carbon ink with a) 45 μm b) 130 μm and c) 255 μm thickness.

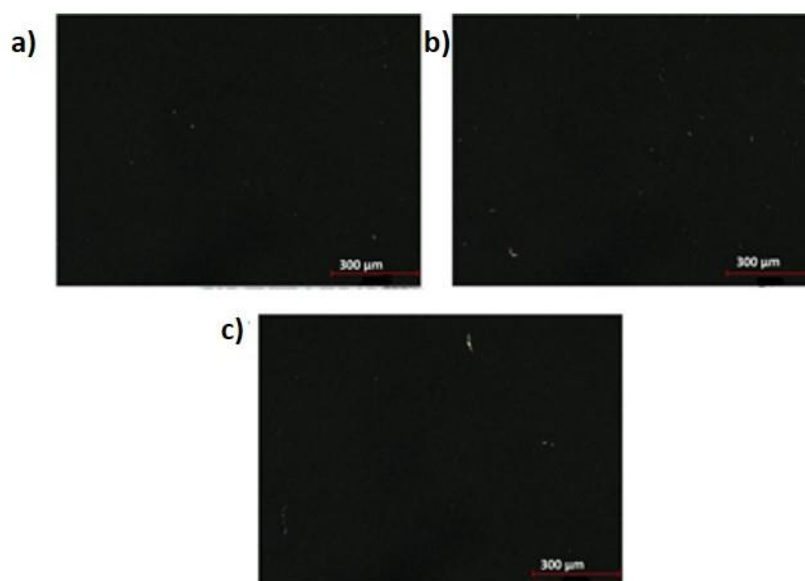


Figure 3.2 : Optic microscope results of low temperature processable carbon ink with a) 45 μm b) 130 μm and c) 255 μm thickness.

Figures below illustrate the SEM and EDAX results. From SEM images (Figure 3.3) with 500x magnification, we can see that the surface of the printed carbon ink is smooth and crackless. With increased magnification up to 5.00kx it can be clearly seen that carbon black, ZrO₂ nanoparticles and graphite particles are mixed homogeneously and make a planar surface. According to EDAX images (Figure 3.4) all types of ingredients such as carbon, flour from PVDF and Zr are distributed regularly in the ink, which proves homogeneity of the carbon ink prepared at low temperature.

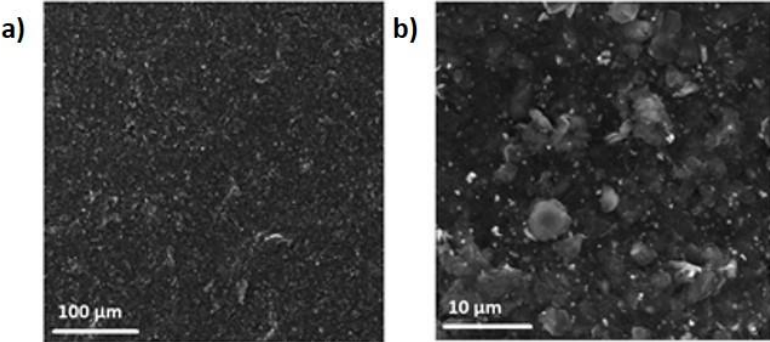


Figure 3.3 : SEM images of low temperature processable carbon ink with a) 500x b) 5.00kx magnification.

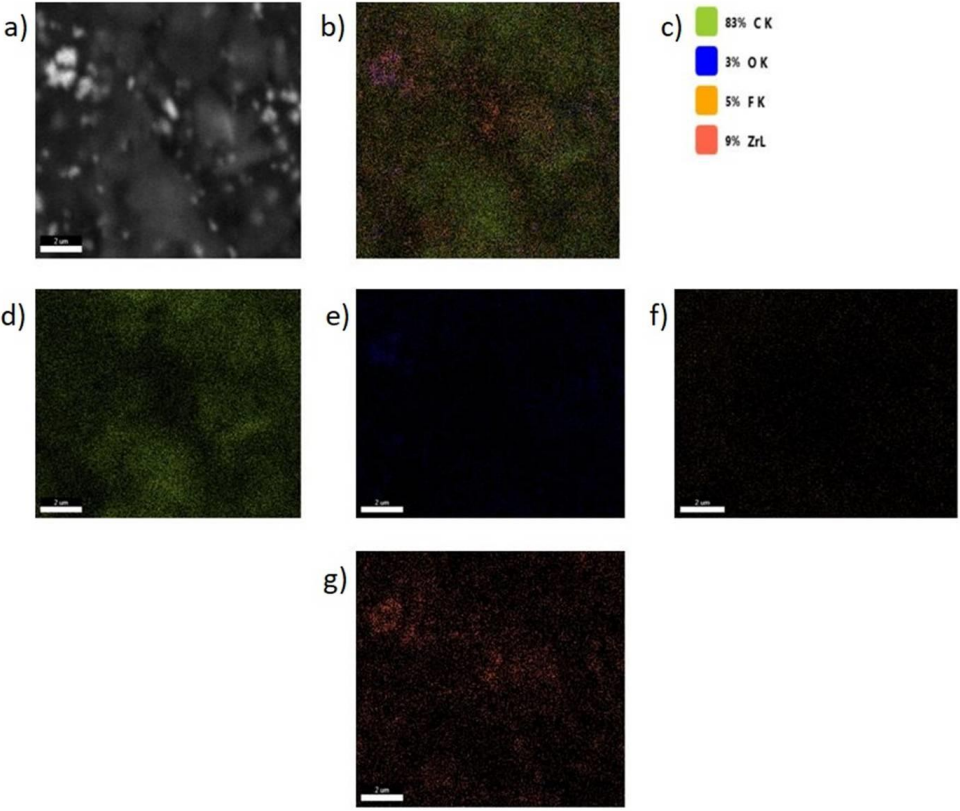


Figure 3.4 : EDAX results of low temperature processable carbon ink.

Resistivity results of the carbon ink can be seen on the Table 3.1 and Figure 3.5. According to results, increased layer thickness enhances the conductivity of the carbon ink because better uniformity of the layer, which cohere with literature.

Table 3.1 : Resistivity results of low temperature procesable carbon ink.

Thickness	Results (ohm)	Sheet Resistance	Bulk Resistance (ohm*cm)
45 μm	137	620,88	1,61
130 μm	46,76	211,92	0,87
255 μm	33,29	150,89	0,78

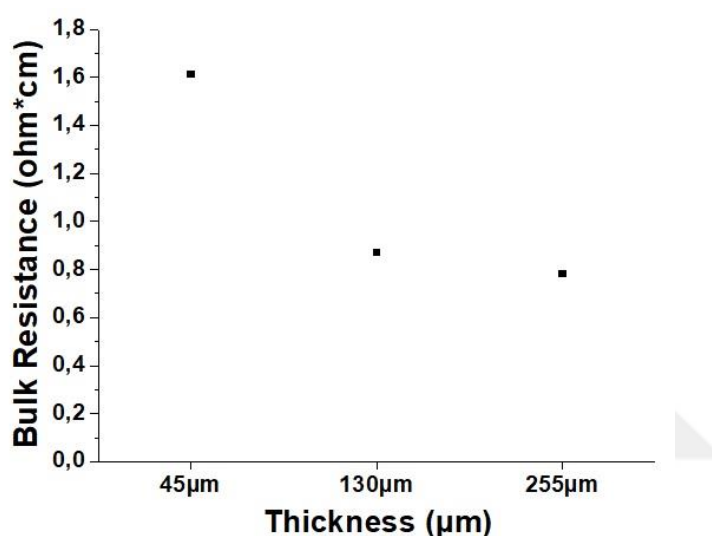


Figure 3.5 : Resistivity diagram of low temperature procesable carbon ink.

3.2 Properties of Environmentally Friendly Coffee Waste Carbon-Based Inks

3.2.1 BET, DFT and Raman analysis results of carbonized coffee particles

BET surface area result illustrated that highest surface area belongs to TC 1:1 carbon particles. Then CM 1:1, TC 2:1 and TC 1:2 carbon particles follow the TC 1:1 carbon particles, respectively.

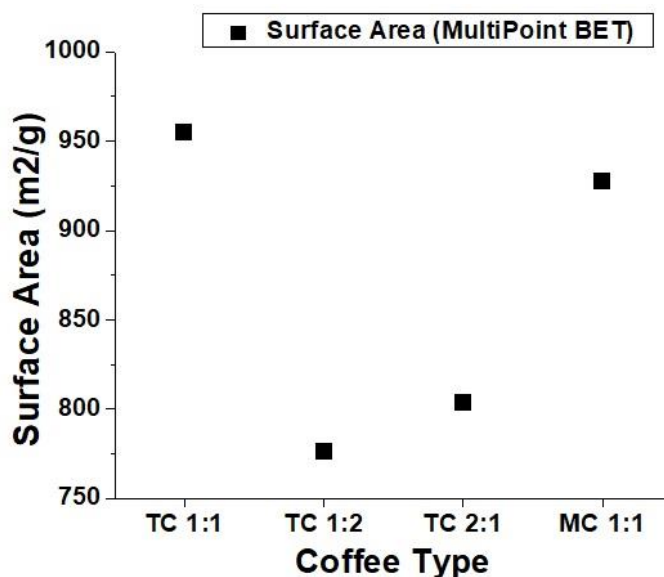


Figure 3.6 : BET surface area analysis for carbonized coffee particles.

DFT test results shown in Figure 3.7 reveal that TC 1:1 carbon particles have the highest microporosity, while TC 1:2 carbon particles have the lowest microporosity. On the other hand, highest mesoporosity is observed in the TC 1:2 carbon particles, which results into low cumulative surface area, as shown in Figure 3.6 and Figure 3.7 b). The high surface area of TC 1:1 is consequence of its large amount of micropores. The highest mesoporous carbon ink showed the highest conductivity result, because mesoporosity act as electron transporting channel in the carbon and enhanced the electrical conductivity of the ink.

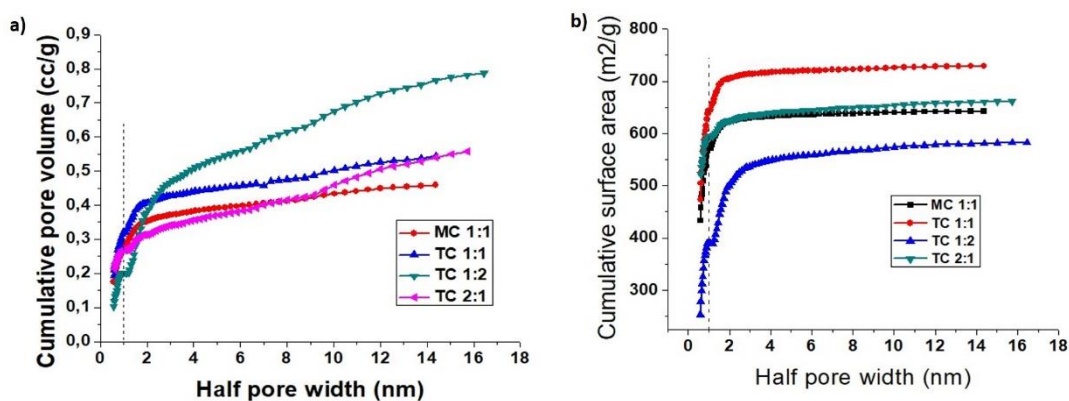


Figure 3.7 : DFT test results of carbonized particles for a) cumulative surface volume and b) cumulative surface area.

The G band of the Raman spectrum demonstrates the order of graphitic planes into the carbon structure, while D band shows their disorder. D' peak is also a disorder-induced double resonance process that indicates nano-crystalline graphite [98]. The area below G and D peaks, more precisely the G/D fraction gives quantitative information about

the ordered-to-disordered phase of carbon particles. From Raman results (Figure 3.8) can be observed that only MC 1:1 particles have D' band which means that nano-crystalline graphite structure exists in this sample. Comparing the G/D results, TC 1:2 particles have the highest value followed by TC 2:1, TC 1:1 and MC 1:1, respectively. This means that among the four samples, TC 1:2 particles have the highest ordered structure, which further leads to highest conductivity.

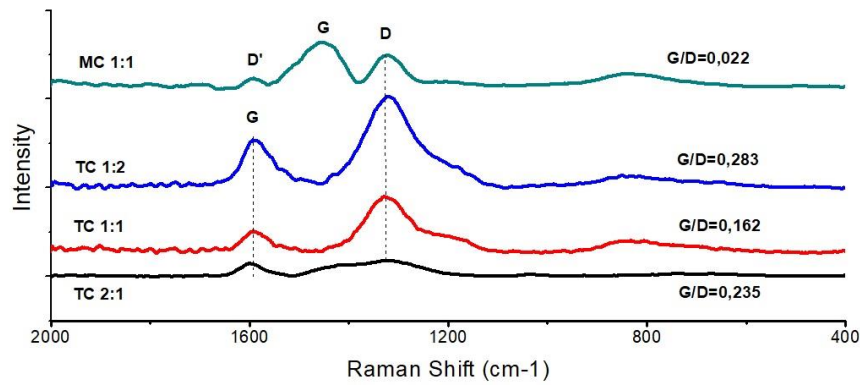


Figure 3.8 : Raman results of carbonized coffee particles.

3.2.2 MC 30/70 results

Espresso coffee waste based carbon ink was applied on FTO surfaces with different thickness. It can be clearly seen from images that regular surface in every part of the glass could not be obtained from this ink. This can be attributed to the irregular and large particle size. These results were also confirmed from optic microscope images.

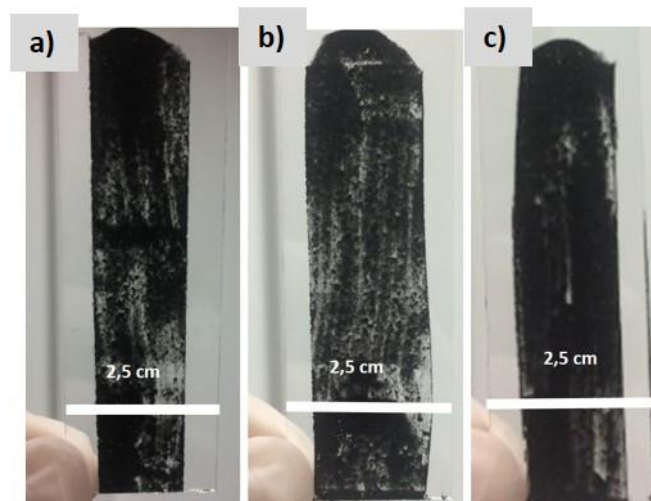


Figure 3.9 : Images of the MC 30/70 carbon ink with a) 45 μm b) 130 μm and c) 255 μm thickness.

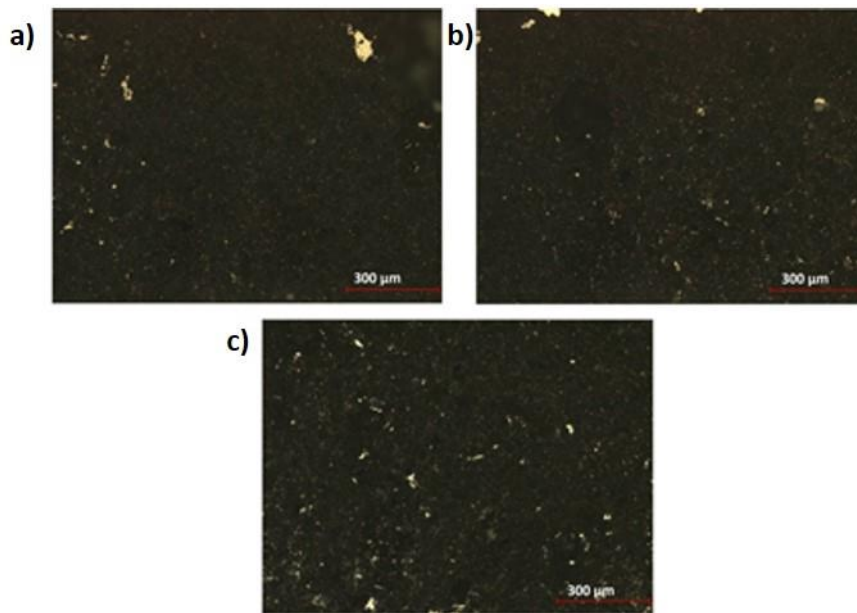


Figure 3.10 : Optic microscope images of MC 30/70 carbon ink with a) 45 μm b) 130 μm and c) 255 μm thickness.

SEM images (Figure 3.11) and EDX results (Figure 3.12) show that MC 1:1 ink was mixed homogenously. However, because of the size of the espresso coffee waste carbon, the surface of the applied ink is characterized with micro-gaps as illustrated in the SEM images. As a consequence of these micro-gaps, the electrical conductivity of this ink also decreases, as shown in Table 3.2.

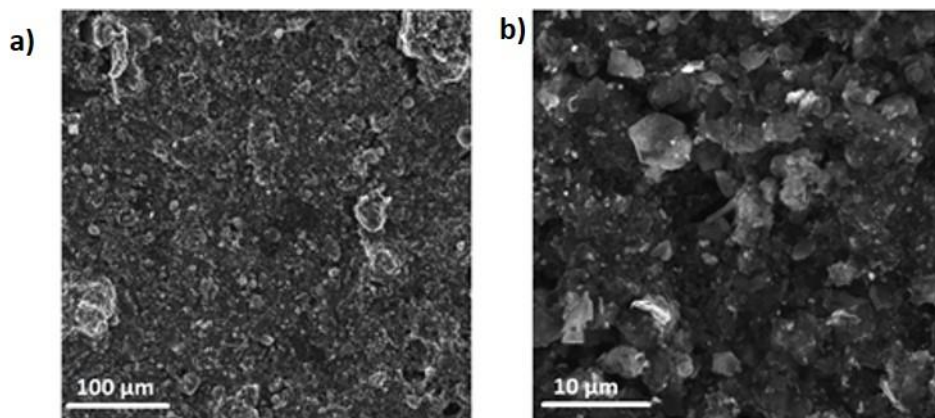


Figure 3.11 : SEM images a) 500x b) 5.00kx magnification of MC 30/70 carbon ink.

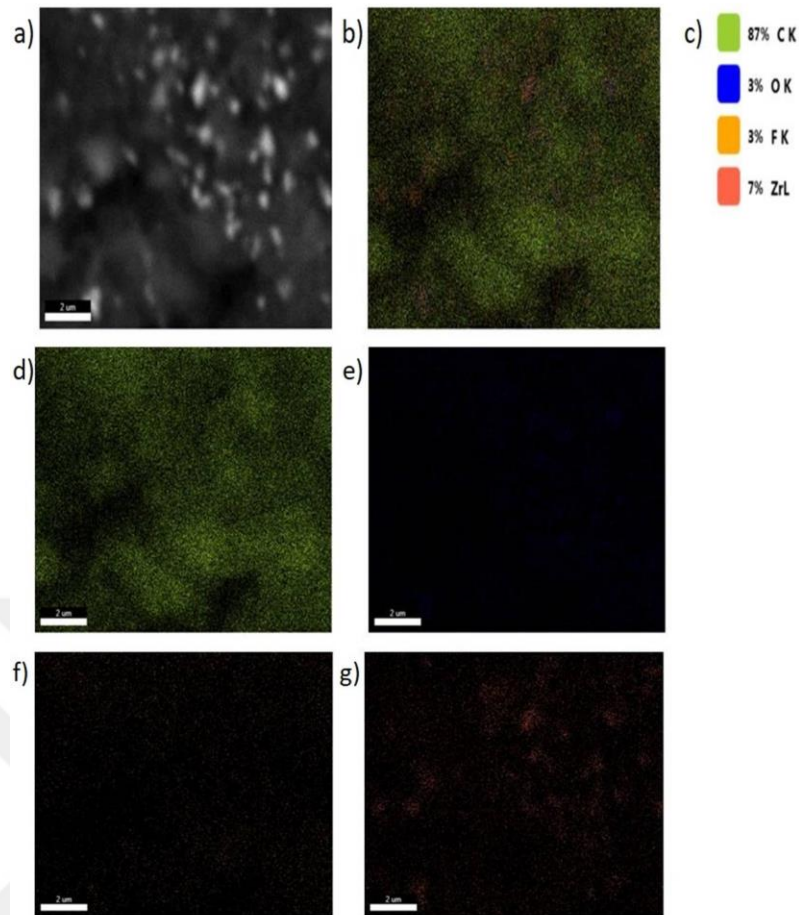


Figure 3.12 : EDAX results of MC 30/70 carbon ink.

Table 3.2 : Resistivity results of MC 30/70 carbon ink.

Thickness	Results	Sheet Resistance	Bulk Resistance (ohm*cm)
45 μm	6550	29684,6	480,89
130 μm	24653,33	111728,91	2089,33
255 μm	6633,33	30062,27	892,85

3.2.3 TC 1:1 30/70 results

TC 1:1 30/70 conductive ink was applied on the FTO surface with different thickness by doctor blading. From the real and optic microscope images, shown on Figure 3.13 and Figure 3.14, respectively we can observe that increased thickness enhances continuous surface of the ink, compared to MC 1:1. This can be attributed to the smaller particle size of this carbon type.

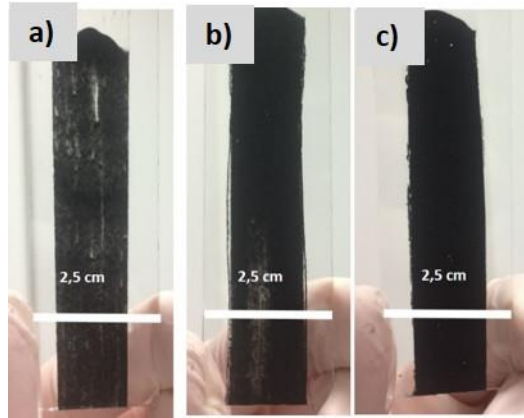


Figure 3.13 : Images of the TC 1:1 30/70 carbon ink with a) 45 μm b) 130 μm and c) 255 μm thickness.

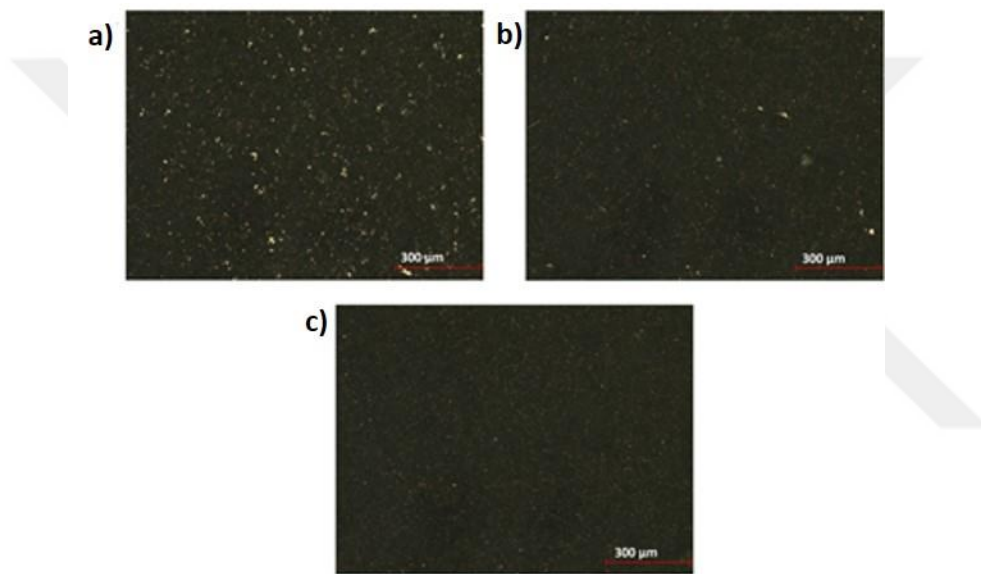


Figure 3.14 : Optic microscope images of TC 1:1 30/70 carbon ink with a) 45 μm b) 130 μm and c) 255 μm thickness.

However, from SEM images (Figure 3.15) some micro size cracks can be observed on the film surface. That cause decline of the conductivity of the film made with this ink, which can be seen from Table 3.3. Despite this, EDAX results (Figure 3.16) show that carbon, flour from PVDF and ZrO_2 particles were distributed homogenously. Resistivity results of the carbon ink are illustrated in Table 3.3. To compare the MC 1:1 carbon, TC 1:1 carbon has smaller particle size and large mesoporous structure which lead the enhance the conductivity of the carbon ink. Moreover, TC 1:1 30/70 carbon ink created a smoother surface when applied on the FTO. This cause to better electron transportation and reduce the resistivity of the ink.

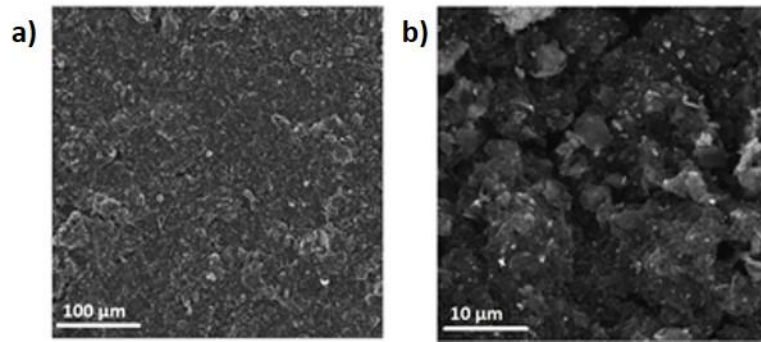


Figure 3.15 : SEM images a) 500x b) 5.00kx magnification of TC 1:1 30/70 carbon ink.

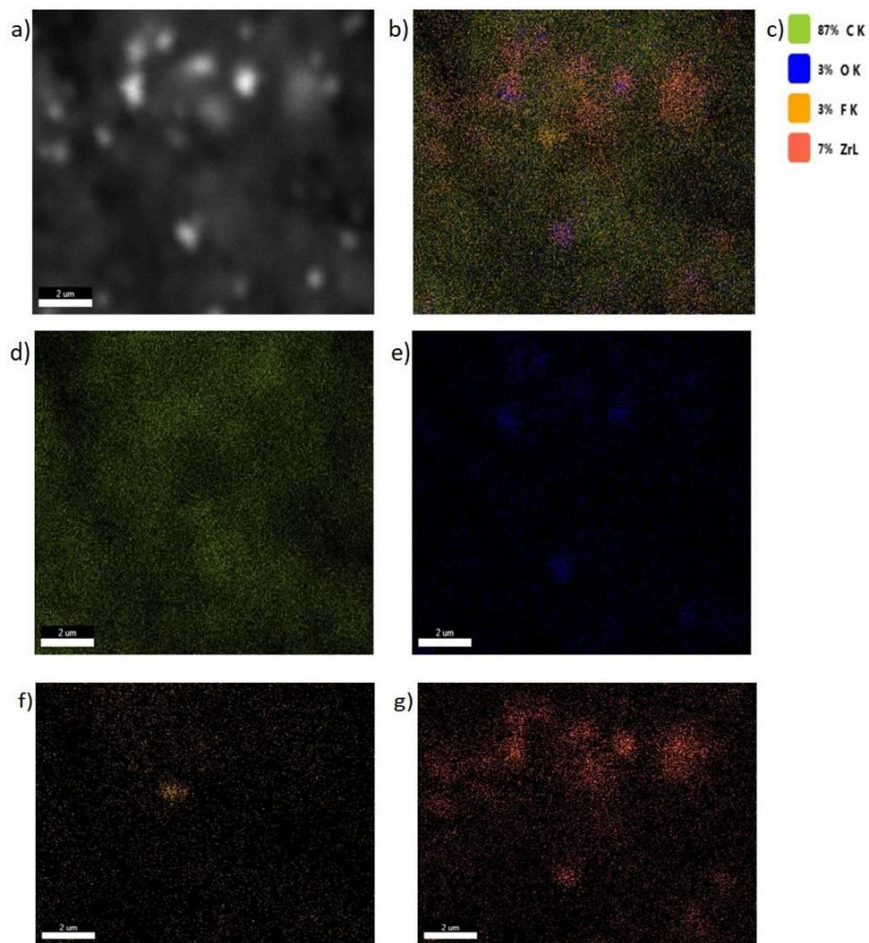


Figure 3.16 : EDAX results of TC 1:1 30/70 carbon ink.

Table 3.3 : Resistivity results of TC 1:1 30/70 carbon ink.

Thickness	Results	Sheet Resistance	Bulk Resistance (ohm*cm)
45 μm	12576,67	56997,45	254,59
130 μm	1570	7115,24	43,40
255 μm	1250	5665	61,56

3.2.4 TC 2:1 30/70 results

TC 2:1 30/70 carbon ink was printed on FTO glass with three different thicknesses. For all thicknesses, continuous surface was obtained and their real and optic microscope images can be seen from the figures below.

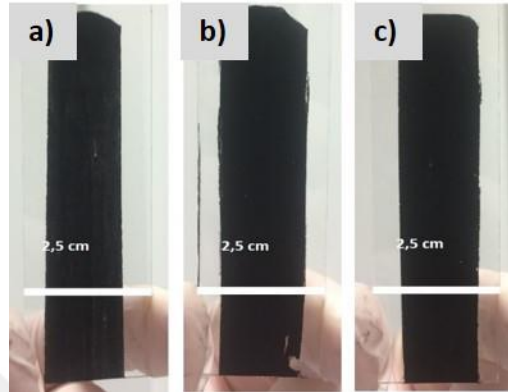


Figure 3.17 : Images of the TC 2:1 30/70 carbon ink with a) 45 μm b) 130 μm and c) 255 μm thickness.

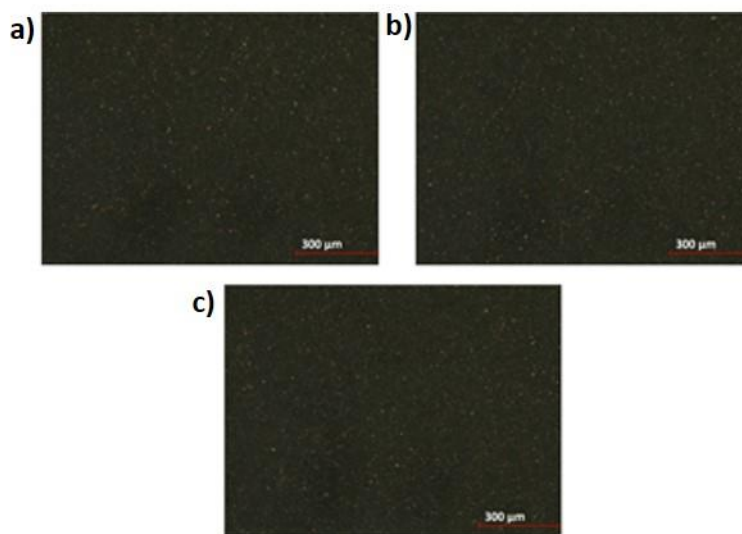


Figure 3.18 : Optic microscope images of TC 2:1 30/70 carbon ink with a) 45 μm b) 130 μm and c) 255 μm thickness.

SEM images (Figure 3.19) were taken at 500x and 5.00kx magnification and confirmed that homogenous surface without cracks was formed. Additionally, EDAX results (Figure 3.20) showed that all ingredients were distributed homogeneously. The smooth film surface and homogeneous ink lead to low resistivity of the film compared to the previous two samples, as shown in Table 3.4.

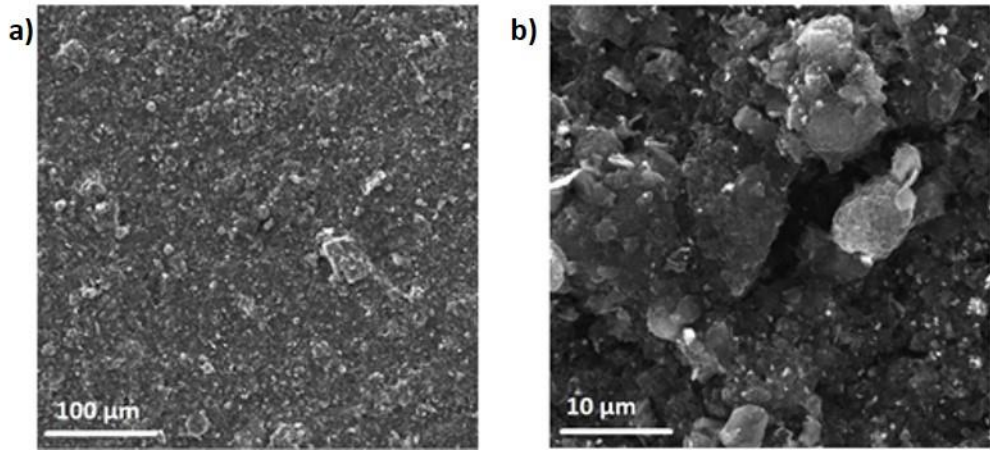


Figure 3.19 : SEM images a) 500x b) 5.00kx magnification of TC 2:1 30/70 carbon ink.

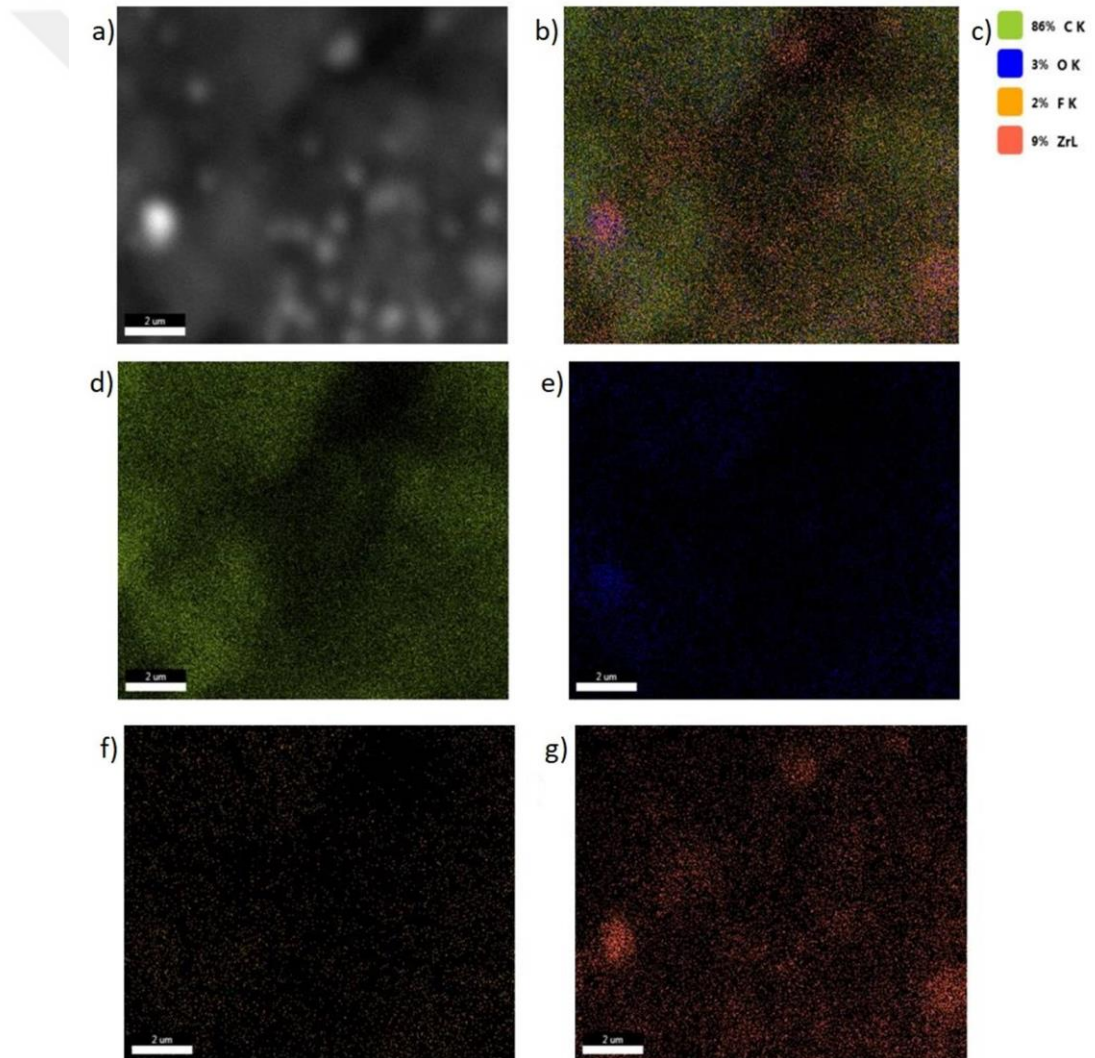


Figure 3.20 : EDAX results of TC 2:1 30/70 carbon ink.

Table 3.4 : Resistivity results of TC 2:1 30/70 carbon ink.

Thickness	Results	Sheet Resistance	Bulk Resistance (ohm*cm)
45 μm	3773,33	17100,75	43,89
130 μm	1204,67	5459,55	22,75
255 μm	758	3435,26	25,99

3.2.5 TC 1:2 30/70 results

Real and optic microscope images of the film from TC 1:2 30/70 carbon ink are demonstrated the figure below (Figure 3.21 and Figure 3.22). They are evidence for the well deposited carbon ink on FTO glass with different thicknesses. This can be result of smallest particle size of this type of coffee waste carbon.

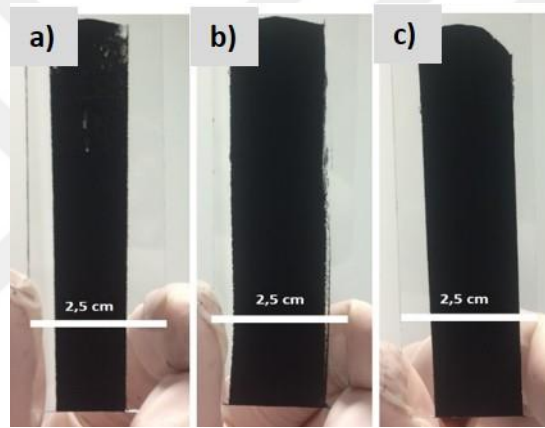


Figure 3.21 : Images of the TC 1:2 30/70 carbon ink with a) 45 μm b) 130 μm and c) 255 μm thickness.

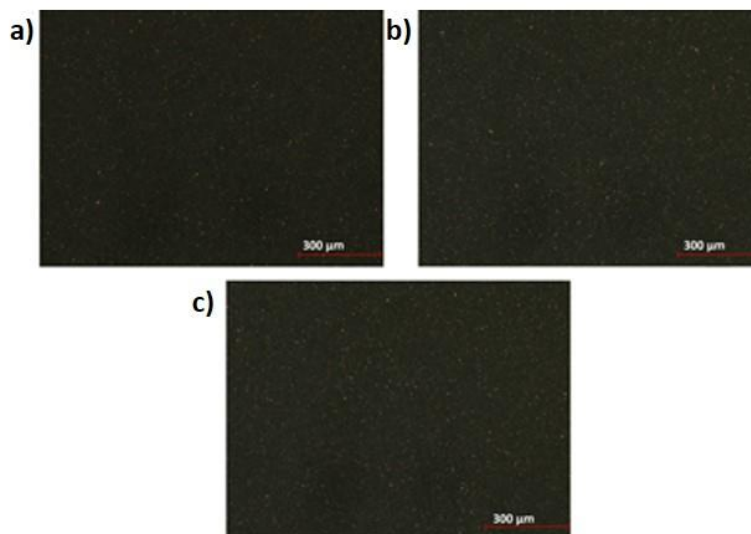


Figure 3.22 : Optic microscope images of TC 1:2 30/70 carbon ink with with a) 45 μm b) 130 μm and c) 255 μm thickness.

SEM images taken at 500x and 5.00kx magnification are shown in Figure 3.23. From 500x image, some crack from on the film surface can be seen. However, from the image at 5.00kx magnification, it can be seen that the carbon black, activated carbon and ZrO₂ nanoparticles filled the gaps between the large graphite particles, which are arranged as a plane layer into the film structure. While PVDF and ethocell hold together all nanoparticles.

The small particle size of TC 1:2 and the connection of all the ingredients within the film structure cause low resistivity (Table 3.5). The bulk resistivity of the films formed from this ink showed the lowest values compared to all the other coffee based carbon samples and gave the best photovoltaic properties of the perovskite solar cell, as shown in Table 3.19.

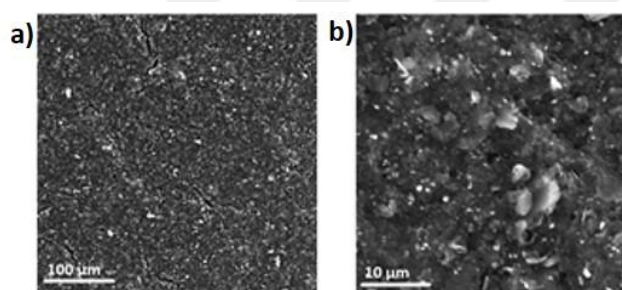


Figure 3.23 : SEM images a) 500x b) 5.00kx magnification of TC 1:2 30/70 carbon ink.

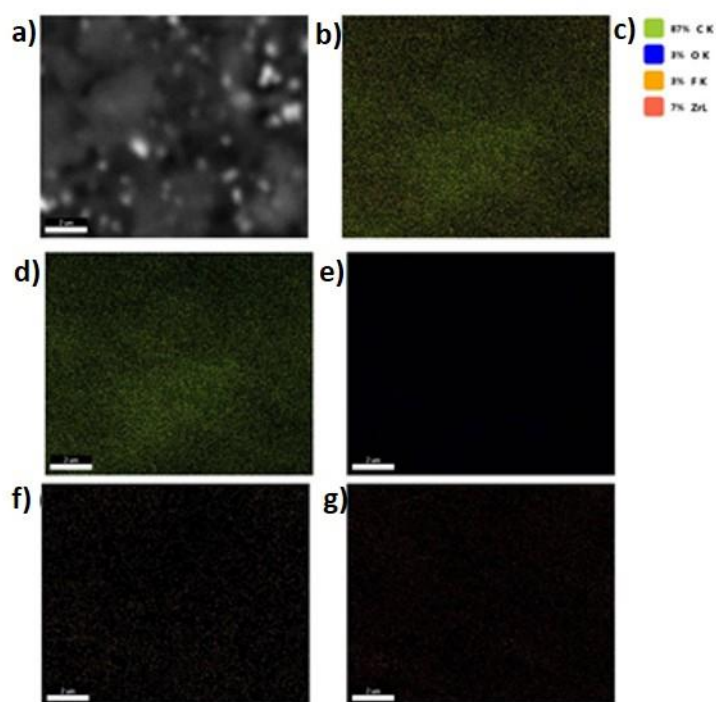


Figure 3.24 : EDAX results of TC 1:2 30/70 carbon ink.

Table 3.5 : Resistivity results of TC 1:2 30/70 carbon ink.

Thickness	Results	Sheet Resistance	Bulk Resistance (ohm*cm)
45 μm	9,33	42,27	0,11
130 μm	155,67	705,48	2,94
255 μm	57,10	258,78	1,96

3.2.6 TC 1:2 10/90 results

To investigate the effect of TC 1:2 activated carbon on conductivity results the amount of activated carbon into the ink was changed. Decreasing the amount of activated carbon affected surface morphology negatively. Real and optic microscope images can be seen from the figures below.

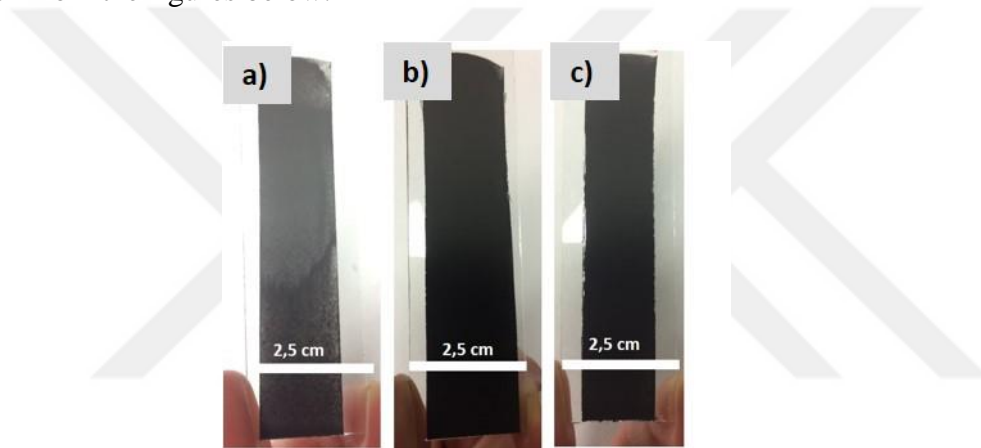


Figure 3.25 : Images of the TC 1:2 10/90 carbon ink with a) 45 μm b) 130 μm and c) 255 μm thickness.

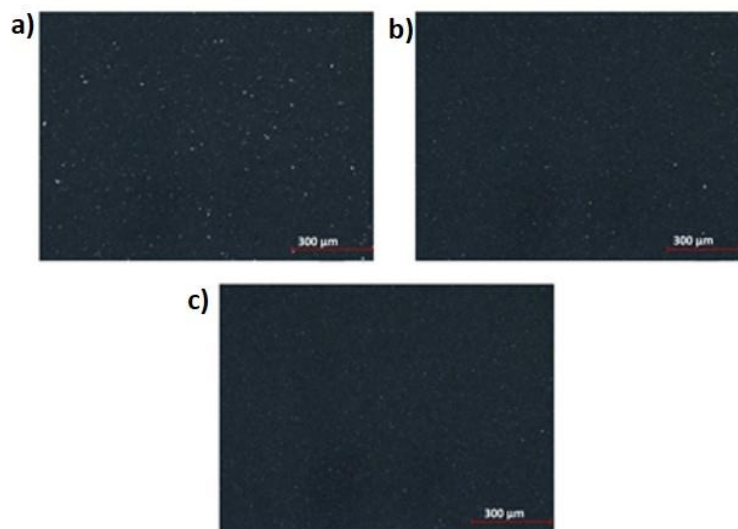


Figure 3.26 : Optic microscope images TC 1:2 10/90 carbon ink with a) 45 μm b) 130 μm and c) 255 μm thickness.

SEM images and EDAX results are illustrated below. From SEM images (Figure 3.27) it can be seen that this carbon ink formed smooth surface. EDAX results (Figure 3.28) revealed that the distribution of the carbon, ZrO₂ and PVDF was homogeneous into the ink.

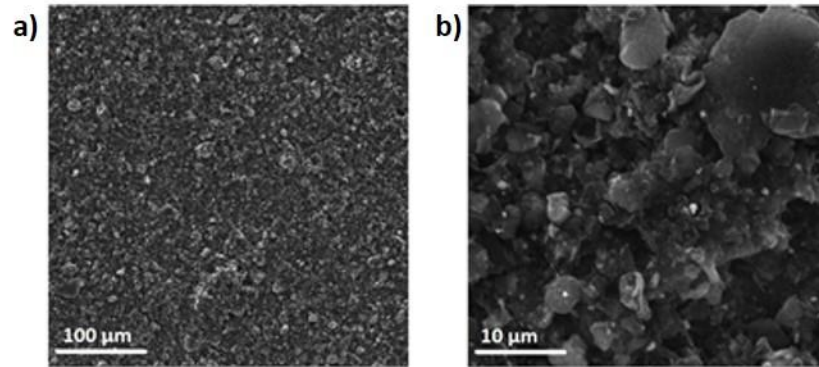


Figure 3.27 : SEM images a) 500x b) 5.00kx magnification of TC 1:2 10/90 carbon ink.

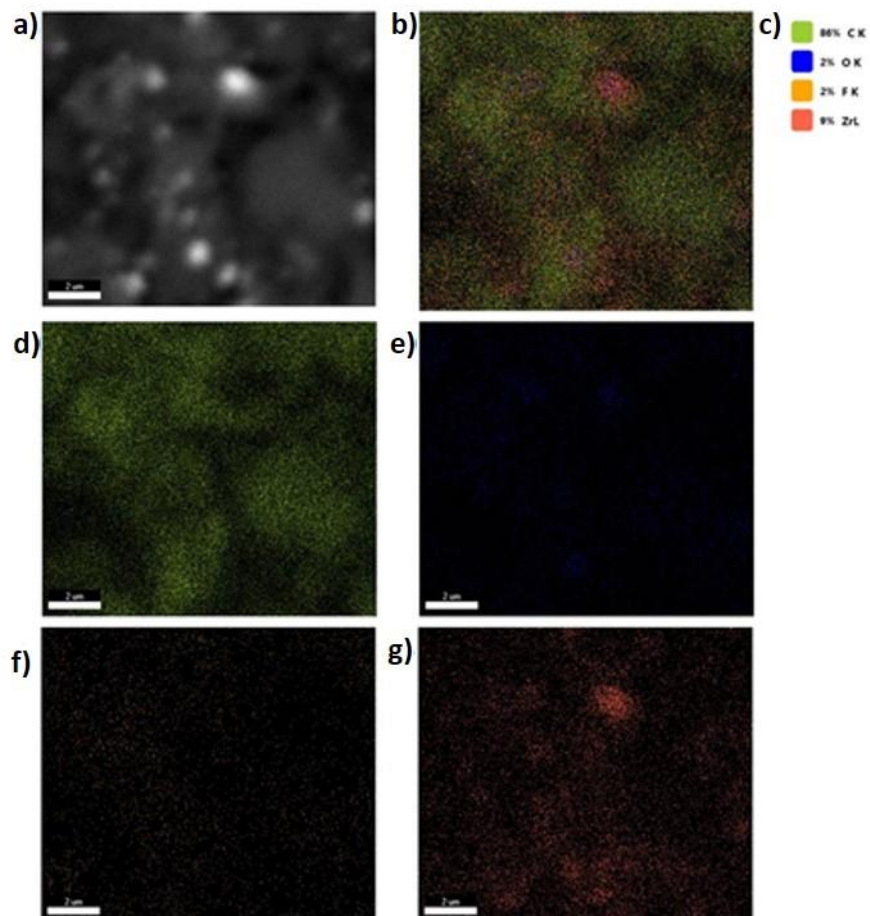


Figure 3.28 : EDAX results of TC 1:2 10/90 carbon ink.

Resistivity results (Table 3.6) are comparable with literature and show that increased layer thickness enhances the conductivity of the film. The results also demonstrated that decreased activated carbon amount also decreases the conductivity of the film.

Table 3.6 : Resistivity results of TC 1:2 10/90 carbon ink.

Thickness	Results	Sheet Resistance	Bulk Resistance (ohm*cm)
45 μm	1520	6888,64	62,23
130 μm	298	1350,54	15,40
255 μm	209,67	950,21	21,41

3.2.7 TC 1:2 50/50 results

The films formed from TC 1:2 50/50 carbon ink are shown in the real and optic microscope images below. They show that adding activated carbon more than 30wt% breaks the uniformity of the ink.

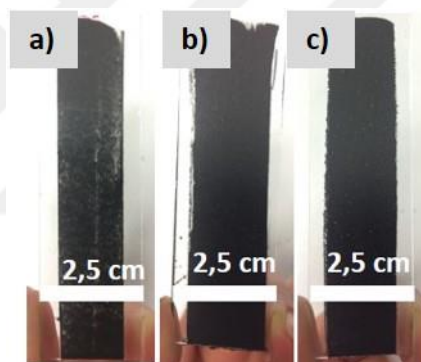


Figure 3.29 : Images of the TC 1:2 50/50 carbon ink with a) 45 μm b) 130 μm and c) 255 μm thickness.

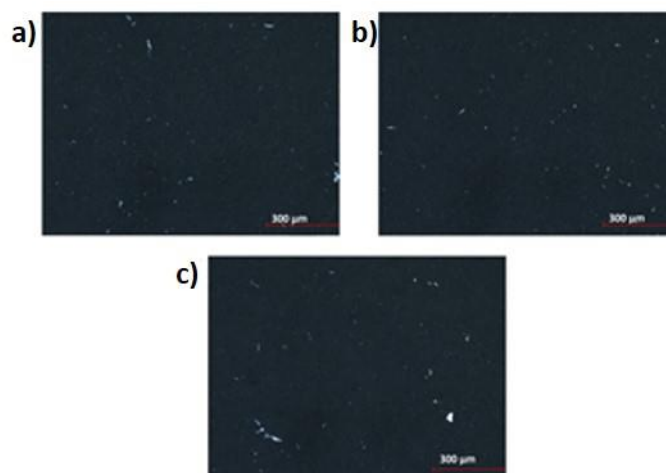


Figure 3.30 : Optic microscope results of TC 1:2 50/50 carbon ink with a) 45 μm b) 130 μm and c) 255 μm thickness.

Morphology of the film was also investigated through SEM images (Figure 3.31) while the homogeneity of the ink was determined from EDAX analysis (Figure 3.32). From both of them it can be observed that decreasing the carbon black and graphite particles affect in the ink negatively, which results in nonuniform surface morphology and thus increased of resistivity (Table 3.7).

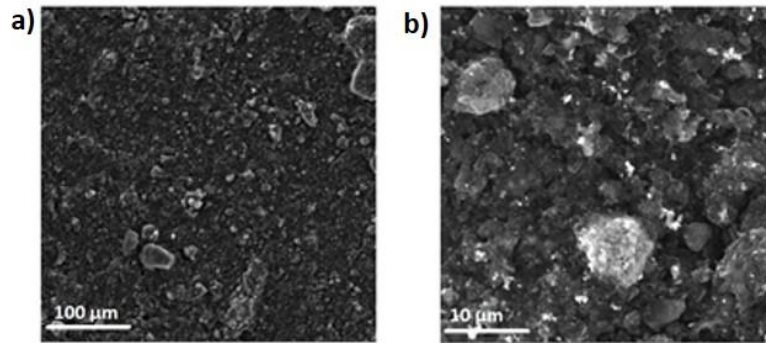


Figure 3.31 : SEM images a) 500x b) 5.00kx magnification of TC 1:2 50/50 carbon ink.

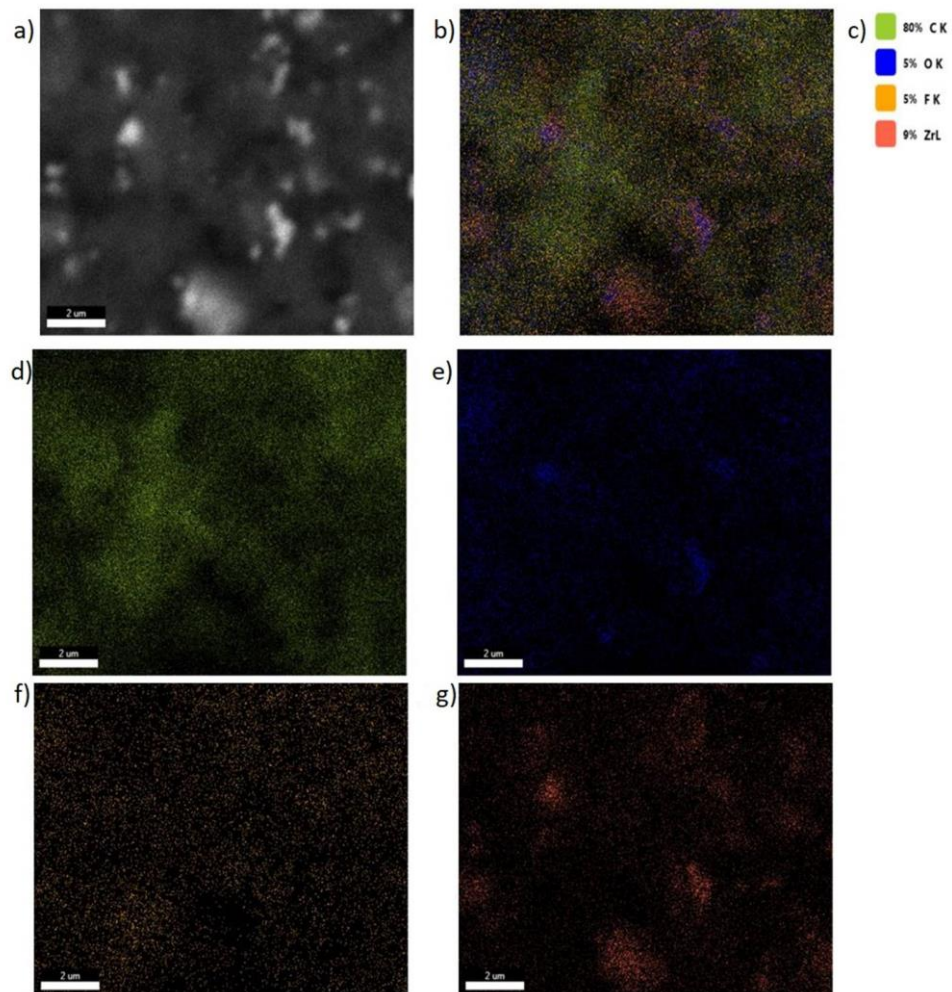


Figure 3.32 : EDAX results of TC 1:2 50/50 carbon ink.

Table 3.7 : Resistivity results of TC 1:2 50/50 carbon ink.

Thickness	Results	Sheet Resistance	Bulk Resistance (ohm*cm)
45 μm	7996,67	36240,89	407,11
130 μm	2510	11375,32	134,61
255 μm	1336,67	6057,77	117,52

BET (Figure 3.6), DFT (Figure 3.7) and Raman (Figure 3.8) results of the ball-milled biowaste carbon and resistivity comparison (Figure 3.33) of low temperature processable and biowaste carbon inks can be seen. According to the literature [99], BET does not give the accurate value to determine the surface area of the porous carbon, on the other hand DFT is more accurate than BET. In the BET method, an inert gas is released to the system until creating a monolayer on the carbon surface. Due to the existence of micropores in the carbon, gas tends to first fill these pores, so it prevents the calculate some surface area. However, in the DFT method, gas is released the system until all surface areas are covered. Therefore, in this study I am taking into account DFT results. From DFT cumulative surface area (Figure 3.7b)) result, ball milled carbons have the highest surface area TC 1:1, TC 2:1, MC 1:1 and TC 1:2, respectively. DFT cumulative pore volume (Figure 3.7a)) showed the microporous and mesoporous volume of the carbon. Microporosity is the highest in TC 1:1 and following by MC 1:1, TC 2:1 and TC 1:2. On the other hand, TC 1:2 has the highest mesoporosity and following by TC 2:1, TC 1:1 and MC 1:1. It can be said that the highest surface area of the TC 1:1 can be result of micropore volume of the structure.

Raman result showed that the highest ordered/disordered structure is obtained from TC 1:2 and following by TC 2:1, TC 1:1 and MC 1:1. Compared the MC 1:1 30/70, TC 1:1 30/70, TC 1:2 30/70 and TC 2:1 30/70 carbon ink electrical results, TC 1:2 30/70 has the highest electrical conductivity and followed by the TC 2:1 30/70, TC 1:1 30/70 and MC 1:1 30/70.

According to all results, mesoporosity and ordered structure ratio of the carbon have the main effect on the electrical conductivity. Because mesopores create transport channels for the electrons and enhance the conductivity. Also, disordered structures act as an obstacle and prevent electron transporting. That explains why the MC 1:1 30/70 carbon ink has the lowest conductivity and TC 1:2 30/70 carbon ink has the highest conductivity. Moreover, TC 1:2 30/70 carbon ink formed the most smooth

layer when applied to the FTO, which is also improves the conductivity of the ink. According to DFT, Raman and conductivity results, it can be seen that among the three physical properties (surface area, pore size and graphitic order) mesoporosity and the the order of the carbonaceous structure have highest influence on conductivity.

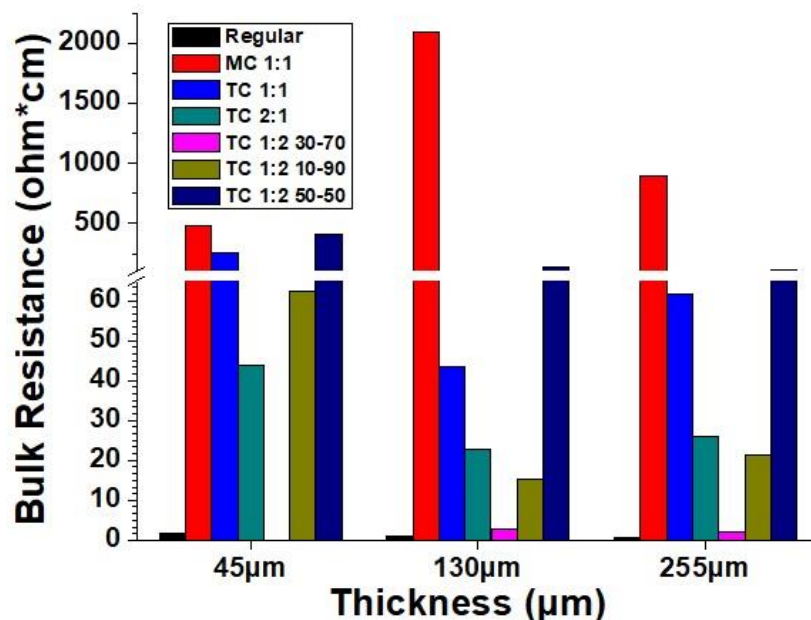


Figure 3.33 : Resistivity comparison of low temperature processable and biowaste carbon inks.

3.3 Properties Of Polymer-Doped Low Temperature Processable Carbon-Based Conductive Ink

3.3.1 FTIR results of PVDF, silver-doped PVDF and silver nitrate-doped PVDF films

Poly vinylidene fluoride (PVDF) is a semi-crystalline polymer which has a good permittivity and advanced dielectric constant [100]. Moreover, fluorine in the PVDF has high electronegative properties and CF_2 group might charge nanoparticles surface [101]. PVDF shows five different polymorphs such as $\alpha, \beta, \gamma, \delta$ and ϵ in its crystalline structure. Among them, δ and ϵ -polymorphs are polar and antipolar form of α and γ -poymorph, respectively [101]. The specific properties of the three main polymorphs are shown in Table 3.8.

Table 3.8 : Polymorph structures of PVDF and their properties [101].

Polymorph Name	Unit Cell Configuration	Chain Conformation	Electroactive Properties
α	monoclinic	TGTG	inactive
β	orthorhombic	all-trans chain	active
γ	orthorhombic	T ₃ GT ₃ G	inactive

According to FTIR results (Figure 3.34), neat PVDF, silver-doped PVDF and silver nitrate-nitrate doped PVDF illustrate peaks at 1234 cm^{-1} , 875 cm^{-1} , 839 cm^{-1} and 510 cm^{-1} which demonstrate the γ , α , β and γ and β and γ -polymorphs (Table 3.9), respectively. However, adding silver nitrate and silver increase the β -polymorph structure in PVDF. Neat PVDF film does not show any peak at 1270 cm^{-1} , but in silver- and silver nitrate doped PVDF it can be seen. Moreover, the peak at 445 cm^{-1} characteristic for β -polymorph is most prominent in silver nitrate-doped PVDF. It is less prominent in silver-soped PVDF and vanishes in the neat PVDF. On the other hand, the peak at 430 cm^{-1} that indicates γ -polymorph can not be seen in the silver nitrate-doped PVDF but it can be seen in silver doped and neat PVDF structure. The peak at 1726 cm^{-1} that illustrate the C=O bond [100,102], can be seen only in silver nitrate-doped PVDF because of the presence of O₂ element in the silver nitrate.

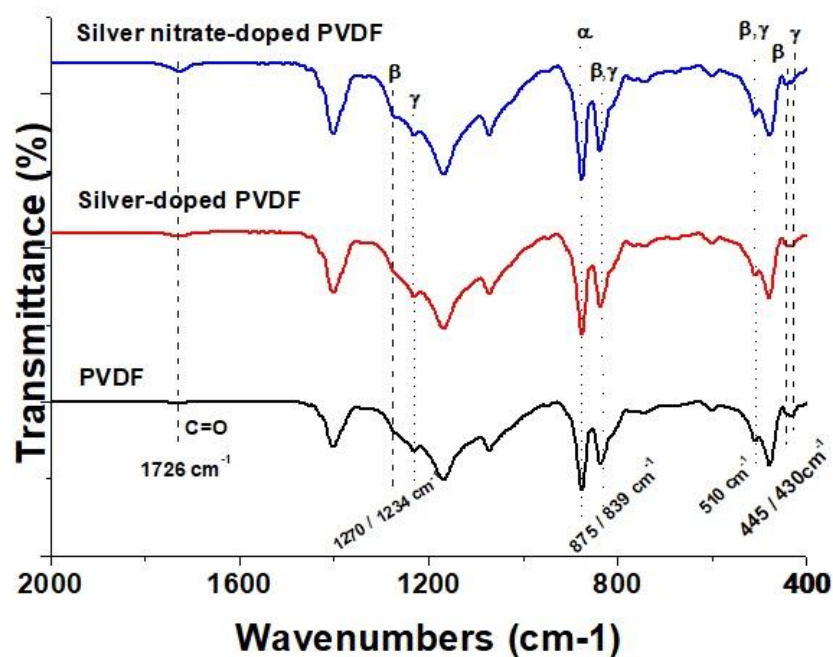


Figure 3.34 : FTIR results of PVDF/silver-doped PVDF and silver nitrate-doped PVDF.

Table 3.9 : Wavenumber of polymorph structures of PVDF [101,103,104].

Polymorph name	Wavenumber (cm ⁻¹)
α	532, 764, 796, 875, 976, 1215, 1385
β	510, 444, 467, 840, 883, 1275
γ	430, 510, 811, 840, 884, 1233

3.3.2 Silver nanoparticles doped polymer-based carbon ink results

3.3.2.1 0.25 mM silver nanoparticles doped PVDF results

Carbon ink containing 0.25 mM Ag np was applied on FTO surfaces with different thickness. From the real and optical microscope images (Figure 3.35 and Figure 3.36) irregular surface were observed for the thinnest films, which improves when the number of layers increases.

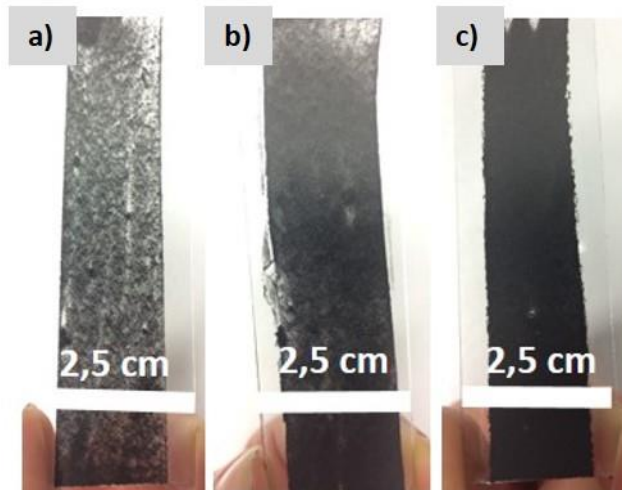


Figure 3.35 : Images of the 0,25 mM Ag doped-PVDF carbon ink with a) 45 μm b) 130 μm and c) 255 μm thickness.

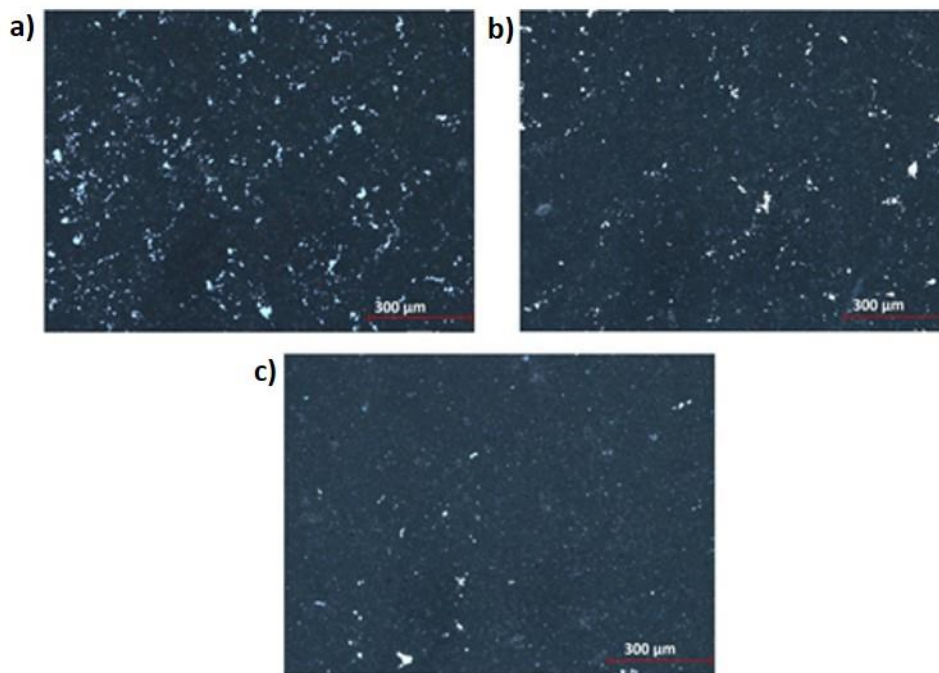


Figure 3.36 : Optic microscope images of 0,25 mM Ag doped-PVDF carbon ink with a) 45 μm b) 130 μm and c) 255 μm thickness.

SEM images (Figure 3.37) and EDX results (Figure 3.38) show that silver nanoparticles were mixed homogenously into the ink. However, the surface of the film is characterized with micro-cracks as illustrated in the SEM images. Despite these micro-cracks, the electrical conductivity of this film is less than 10 $\text{ohm}\cdot\text{cm}$, as shown in Table 3.10.

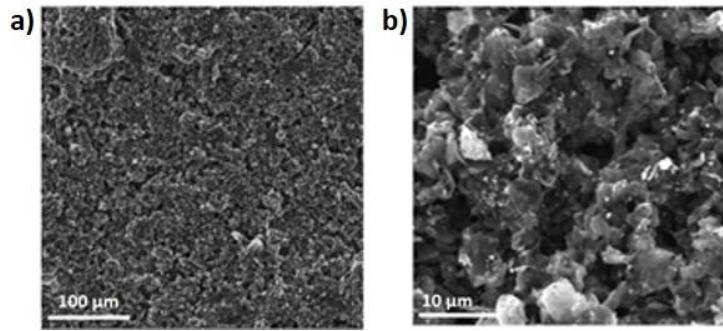


Figure 3.37 : SEM images a) 500x b) 5.00kx magnification of 0,25mM Ag doped-PVDF carbon ink.

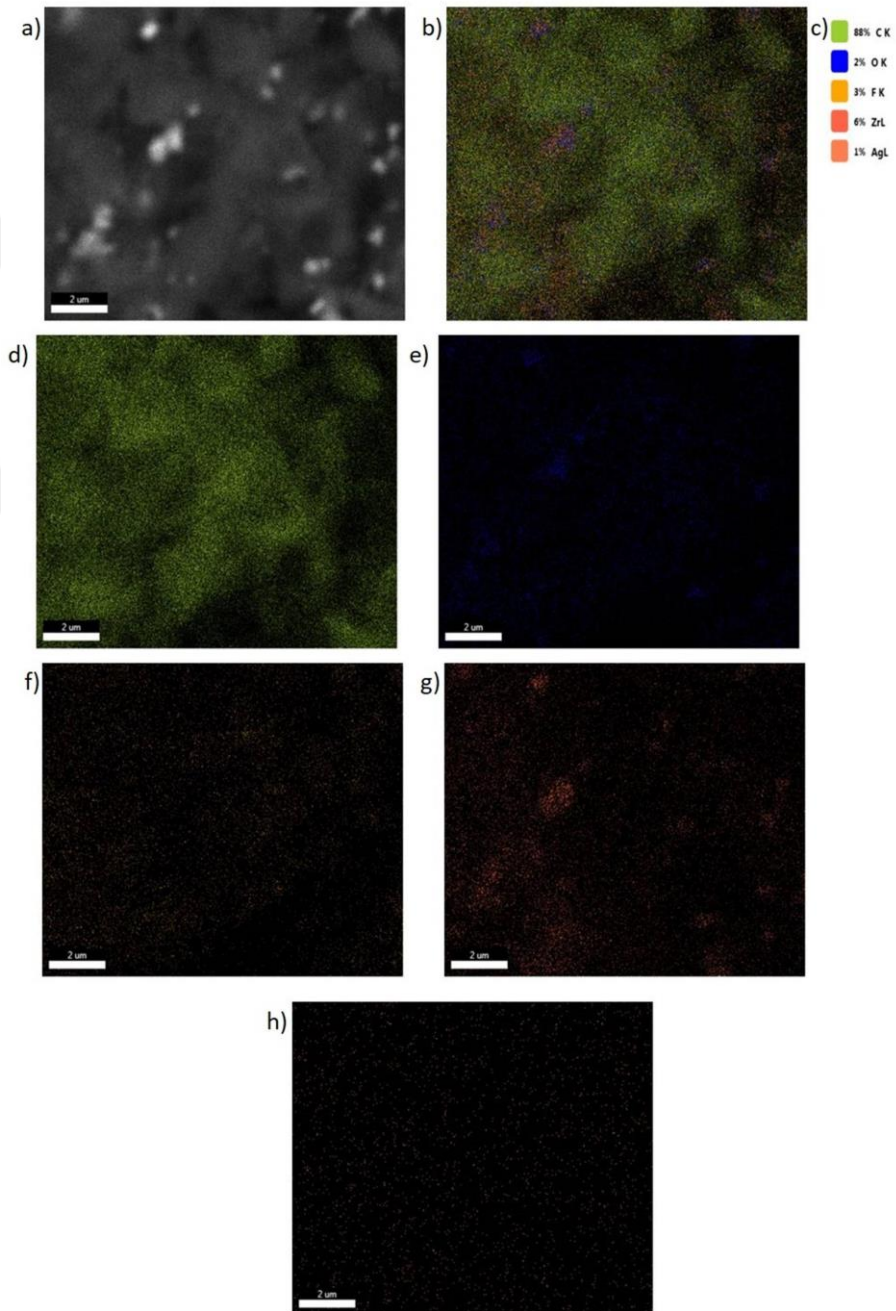


Figure 3.38 : EDAX results of 0,25mM Ag doped-PVDF carbon ink.

Table 3.10 : Resistivity results of 0,25mM Ag doped-PVDF carbon ink.

Thickness	Results	Sheet Resistance	Bulk Resistance (ohm*cm)
45 μm	870,33	3944,35	7,23
130 μm	277,33	1256,87	4,32
255 μm	154,67	700,95	3,88

3.3.2.2 0.5 mM silver nanoparticle doped PVDF results

Carbon ink containing 0.5 mM Ag np was applied on FTO surfaces with different thickness. From the real and optical microscope images (Figure 3.35 and Figure 3.36) irregular surface were observed for the thinnest films, which improves when the number of layers increases.

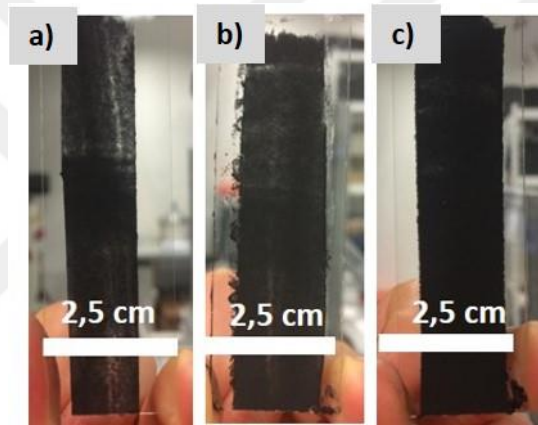


Figure 3.39 : Images of the 0,5 mM Ag doped-PVDF carbon ink with a) 45 μm b) 130 μm and c) 255 μm thickness.

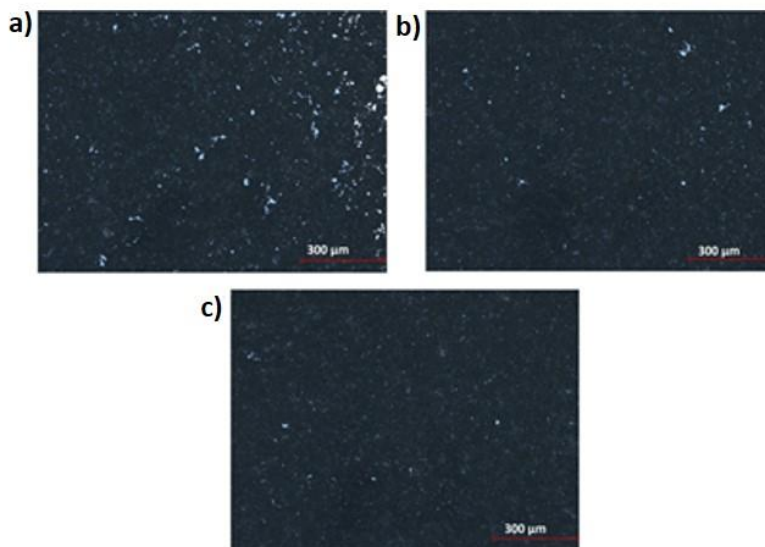


Figure 3.40 : Optic microscope images of 0,5 mM Ag doped-PVDF carbon ink with a) 45 μm b) 130 μm and c) 255 μm thickness.

From SEM (Figure 3.41) images it can be seen non-uniform surface and micro-cracks on the carbon layer. However, homogeneity of the inks were confirmed by EDAX results (Figure 3.42). Moreover, bulk resistances of the film approximately under 3 ohm*cm (Table 3.11).

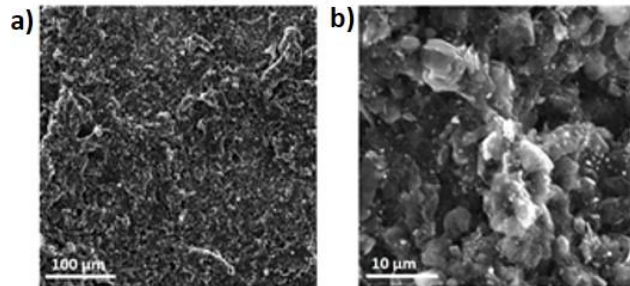


Figure 3.41 : SEM images a) 500x b) 5.00kx magnification of 0,5mM Ag doped-PVDF carbon ink.

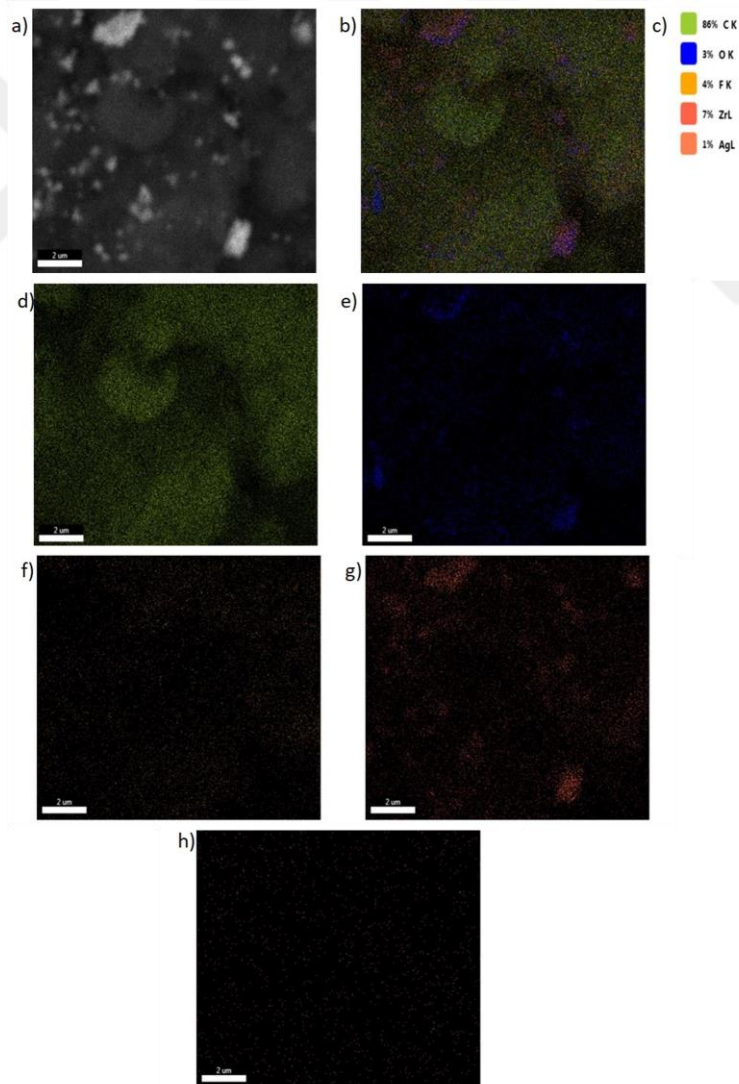


Figure 3.42 : EDAX results of 0,5mM Ag doped-PVDF carbon ink.

Table 3.11 : Resistivity results of 0,5 mM Ag-doped PVDF carbon ink.

Thickness	Results	Sheet Resistance	Bulk Resistance (ohm*cm)
45 μm	399,67	1811,29	3,08
130 μm	125,67	569,52	1,90
255 μm	80,12	363,10	1,82

3.3.2.3 0.75 mM silver nanoparticle doped PVDF results

0.75 mM silver nanoparticle doped PVDF carbon ink was applied at room temperature with 45 μm , 130 μm , and 255 μm thickness on FTO surfaces. As a result, increasing film thickness enhances thin film surface regularity, as shown in (Figure 3.43 and Figure 3.44) .

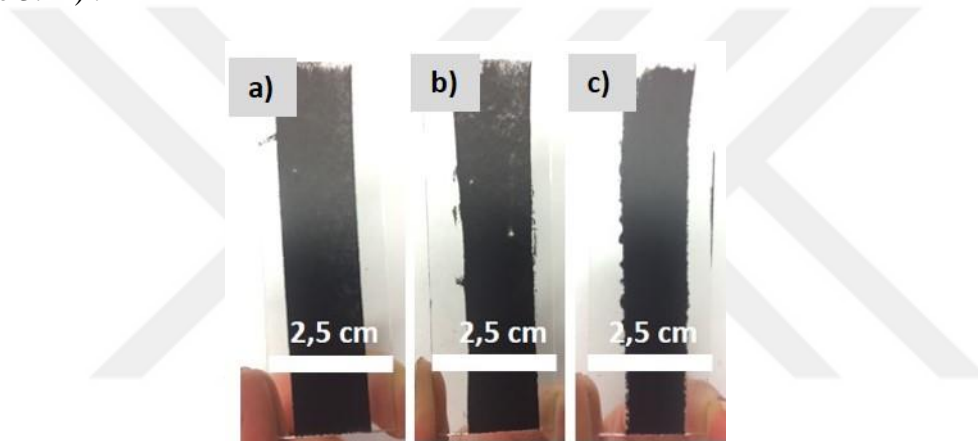


Figure 3.43 : Images of the 0,75 mM Ag doped-PVDF carbon ink with a) 45 μm b) 130 μm and c) 255 μm thickness.

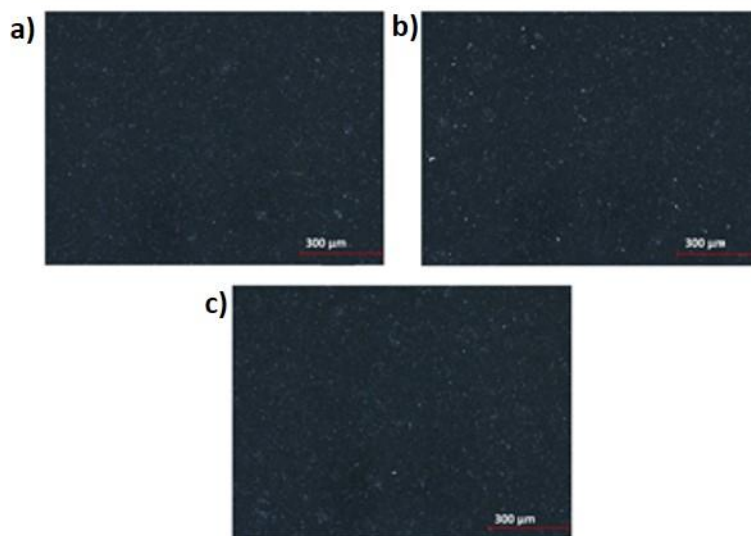


Figure 3.44 : Optic microscope images of 0,75 mM Ag doped-PVDF carbon ink with a) 45 μm b) 130 μm and c) 255 μm thickness.

SEM (Figure 3.45) images and EDAX (Figure 3.46) results illustrated non-uniform surface topography and proved the homogeneity of ingredients in the ink. The electrical resistivity of the carbon film was shown in Table 3.12.

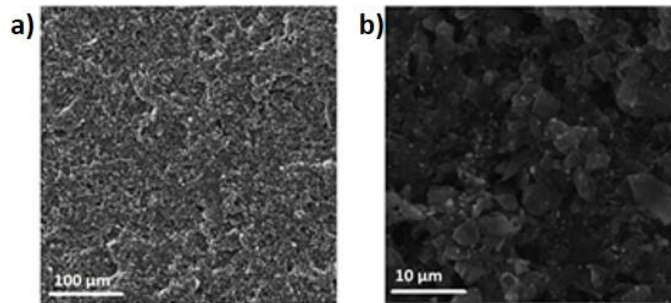


Figure 3.45 : SEM images a) 500x b) 5.00kx magnification of 0,75mM Ag doped-PVDF carbon ink.

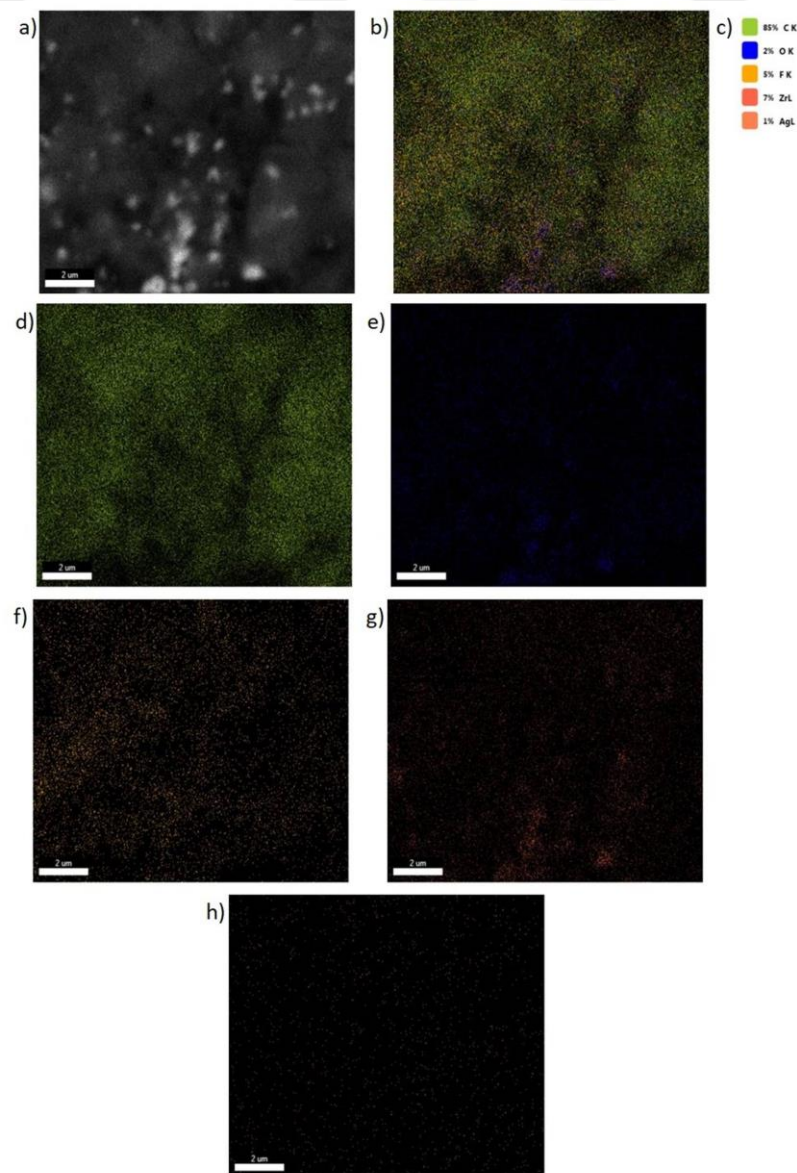


Figure 3.46 : EDAX results of 0,75mM Ag doped-PVDF carbon ink.

Table 3.12 : Resistivity results of 0,75 mM Ag doped-PVDF carbon ink.

Thickness	Results	Sheet Resistance	Bulk Resistance (ohm*cm)
45 μm	163,67	741,74	4,43
130 μm	140,33	635,99	8,16
255 μm	64,82	293,78	5,56

3.3.2.4 1.0 mM silver nanoparticle doped PVDF results

To investigate the film thickness effect on the surface regularity, carbon ink was applied in various thickness on FTO surfaces. According to real image (Figure 3.47) and optic microscope (Figure 3.48) image the most uniform surface was seen from 255 μm thick layer.

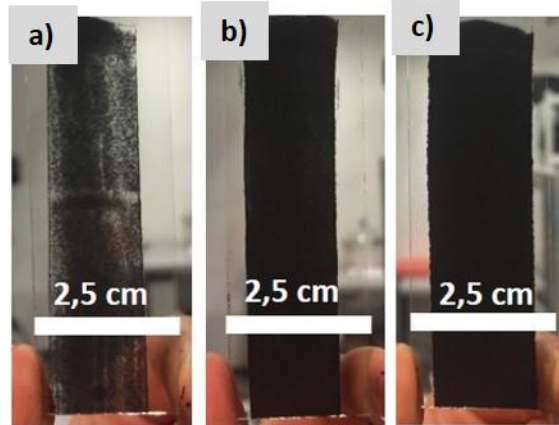


Figure 3.47 : Images of the 1,0 mM Ag doped-PVDF carbon ink with a) 45 μm b) 130 μm and c) 255 μm thickness.

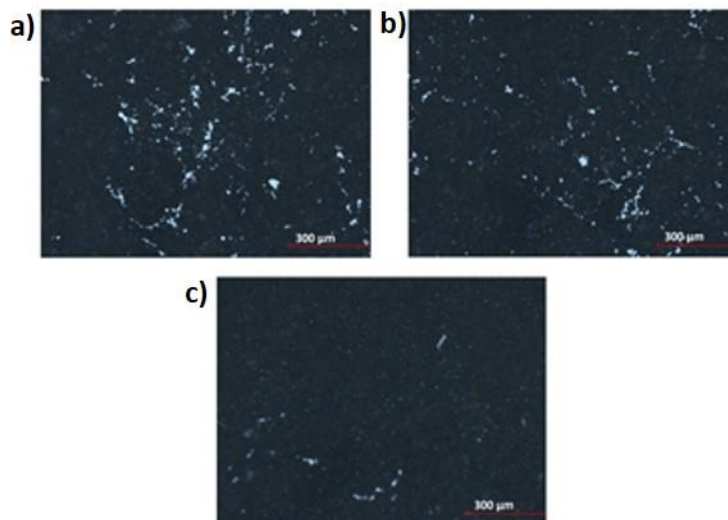


Figure 3.48 : Optic microscope images of 1,0 mM Ag doped-PVDF carbon ink with a) 45 μm b) 130 μm and c) 255 μm thickness.

Silver nanoparticles were mixed homogenously into the ink as shown in SEM images (Figure 3.49) and EDAX results (Figure 3.50). Even though lack of surface uniformity, ink gave the less than 4 ohm*cm electrical resistivity (Table 3.13).

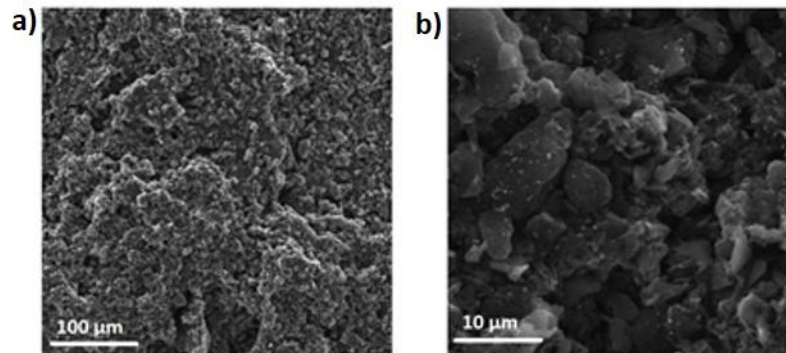


Figure 3.49 : SEM images a) 500x b) 5.00kx magnification of 1,0mM Ag doped-PVDF carbon ink.

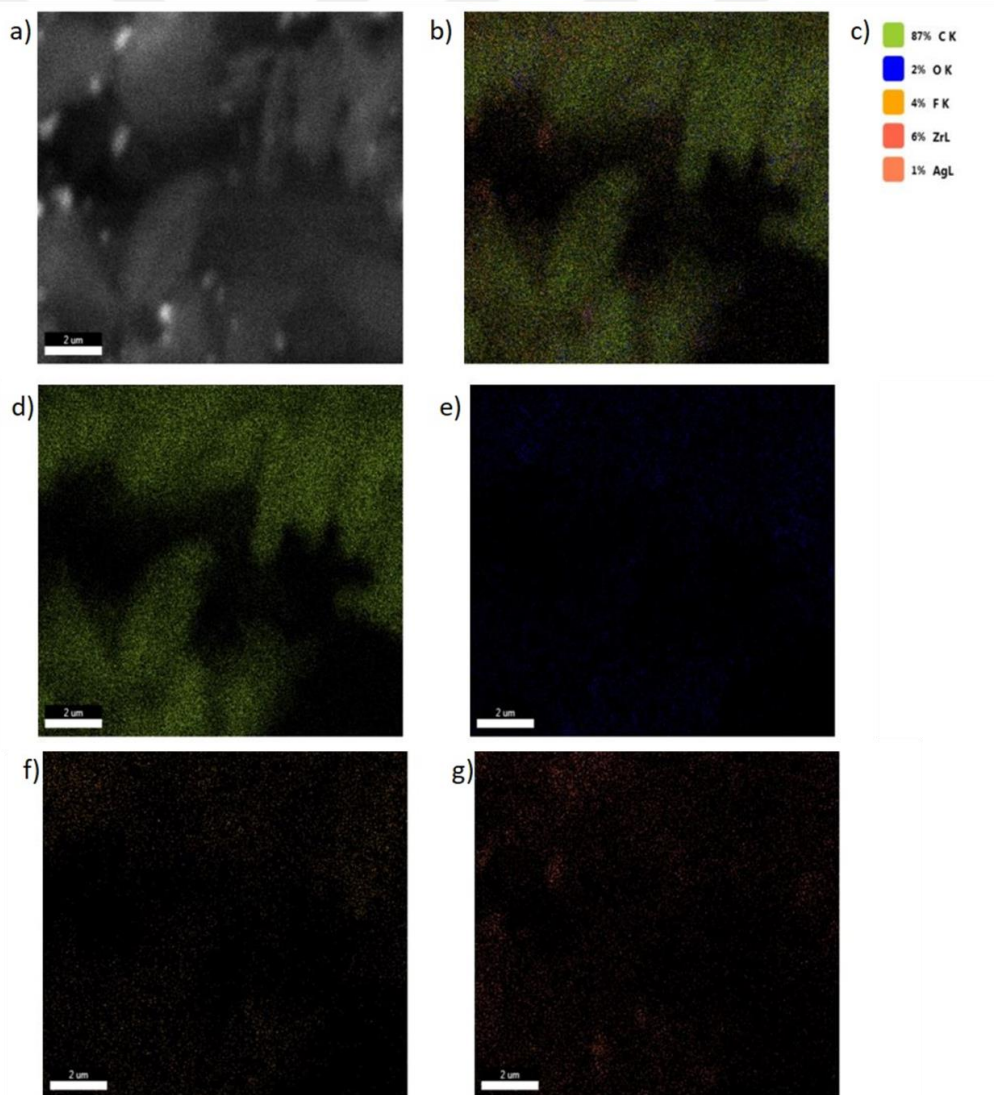


Figure 3.50 : EDAX results of 1,0mM Ag doped-PVDF carbon ink.

Table 3.13 : Resistivity results of 1.0 mM Ag doped PVDF carbon ink.

Thickness	Results	Sheet Resistance	Bulk Resistance (ohm*cm)
45 μm	415,67	1883,80	6,78
130 μm	179,33	812,74	5,04
255 μm	95,83	434,30	3,59

3.3.3 Silver nitrate doped polymer-based carbon ink results

3.3.3.1 0.25 mM silver nitrate doped PVDF results

0,25 mM silver nitrate doped PVDF carbon ink is applied on the FTO substrate and characterized. Real image (Figure 3.51) and optic microscope image (Figure 3.52) confirmed that increasing layer thickness, improve surface uniformity.

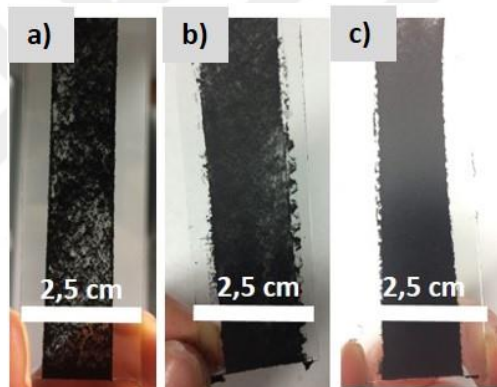


Figure 3.51 : Images of the 0,25 mM AgNO₃ doped-PVDF carbon ink with a) 45 μm b) 130 μm and c) 255 μm thickness.

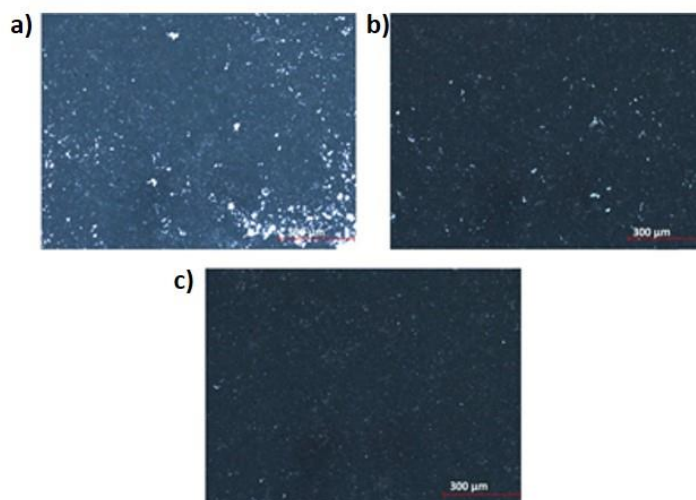


Figure 3.52 : Optic microscope images of 0,25 mM AgNO₃ doped-PVDF carbon ink with a) 45 μm b) 130 μm and c) 255 μm thickness.

SEM images (Figure 3.53) with different magnification show the micro-cracks on the surface of the carbon ink. However, EDAX results (Figure 3.54) proves the homogen dispersion of the ink, and electrical resistivity is shown in Table 3.14.

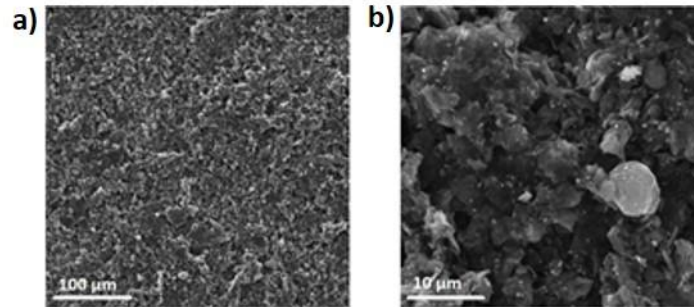


Figure 3.53 : SEM images a) 500x b) 5.00kx magnification of 0,25mM AgNO₃ doped-PVDF carbon ink.

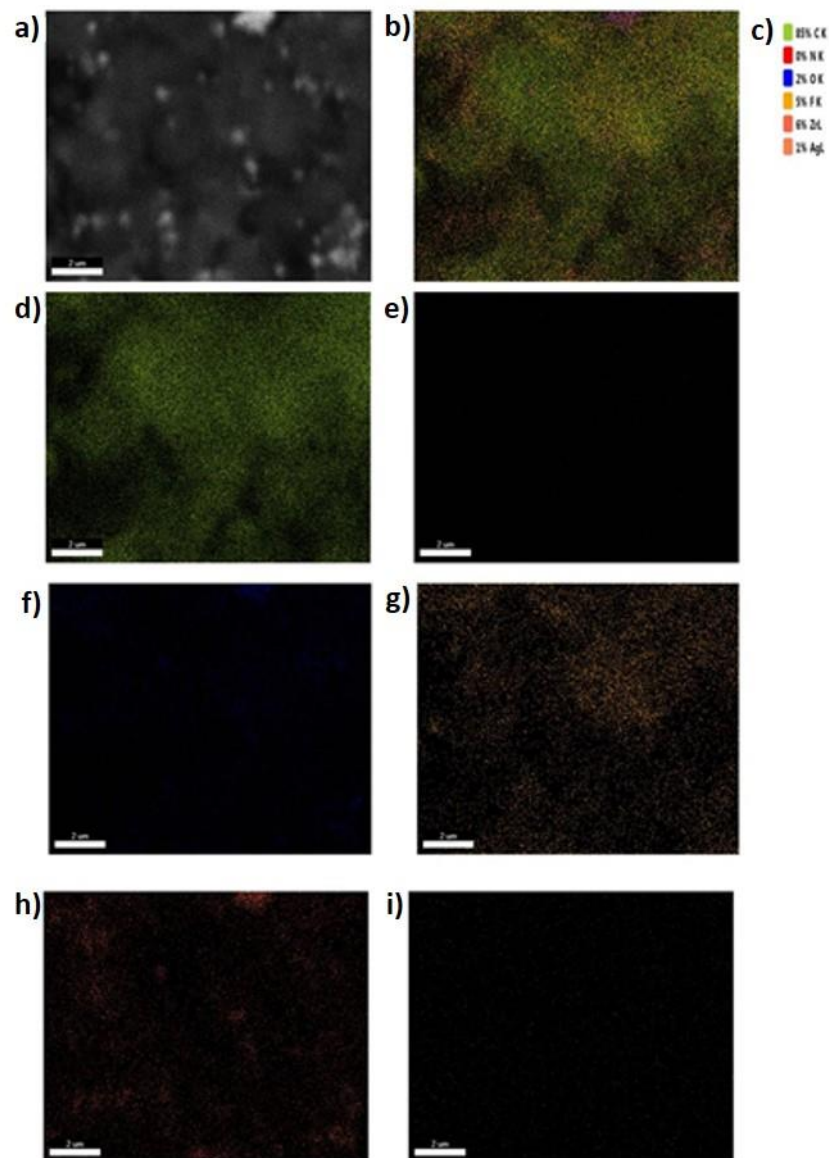


Figure 3.54 : EDAX results of 0,25mM AgNO₃ doped-PVDF carbon ink.

Table 3.14 : Resistivity results of 0,25 mM AgNO₃ doped PVDF carbon ink.

Thickness	Results	Sheet Resistance	Bulk Resistance
45 μm	457,67	2074,15	8,09
130 μm	263,00	1191,92	6,83
255 μm	111,33	504,56	5,30

3.3.3.2 0.5 mM silver nitrate doped PVDF results

Real image (Figure 3.55) and optic microscope images (Figure 3.56) of the carbon ink demonstrate the surface regularity in different thickness. While the thinnest layer could not achieve uniform and regular surface, the thickest layer has more regular and uniform surface.

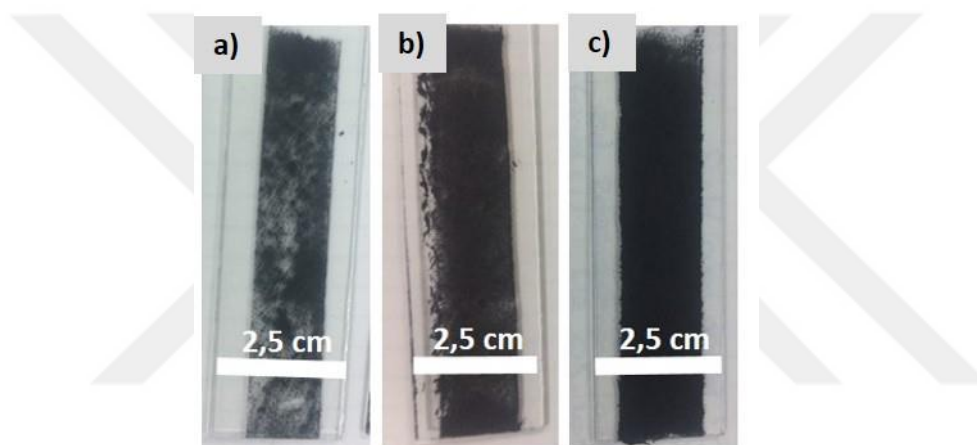


Figure 3.55 : Images of the 0,5 mM AgNO₃ doped-PVDF carbon ink with a) 45 μm b) 130 μm and c) 255 μm thickness.

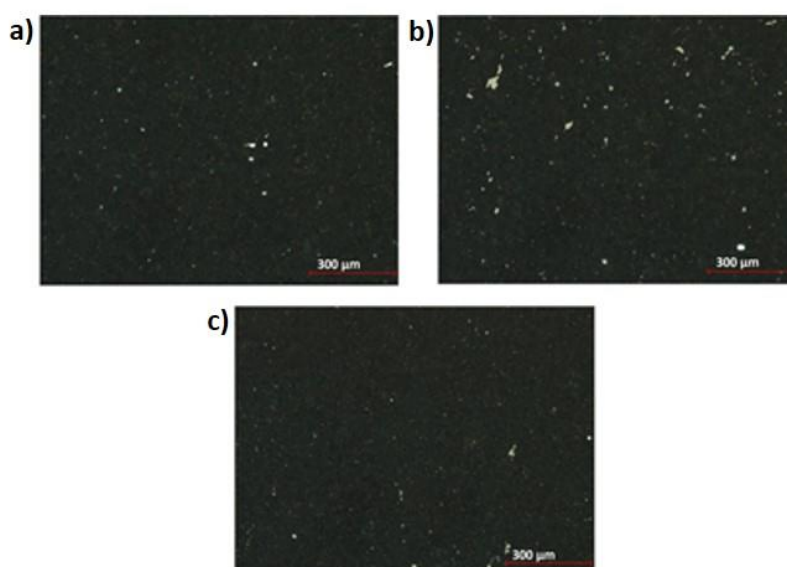


Figure 3.56 : Optic microscope images of 0,5 mM AgNO₃ doped-PVDF carbon ink with a) 45 μm b) 130 μm and c) 255 μm thickness.

Morphological properties of the carbon ink were investigated by SEM images (Figure 3.57) which showed micro-cracks on the surface of the ink. Homogeneity of the film was proved by EDAX results (Figure 3.58). Bulk resistivity of the carbon ink decreased by increasing layer thickness of film (Table 3.15).

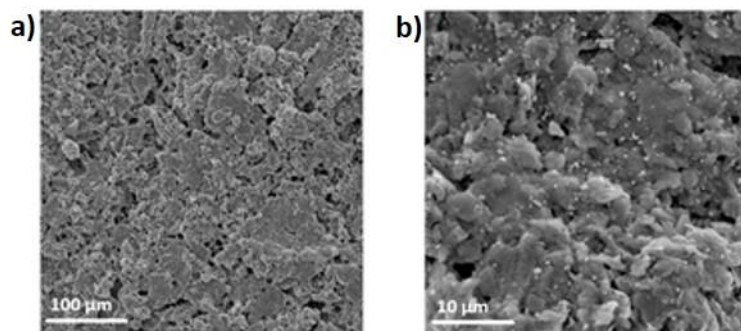


Figure 3.57 : SEM images a) 500x b) 5.00kx magnification of 0,5mM AgNO₃ doped-PVDF carbon ink.

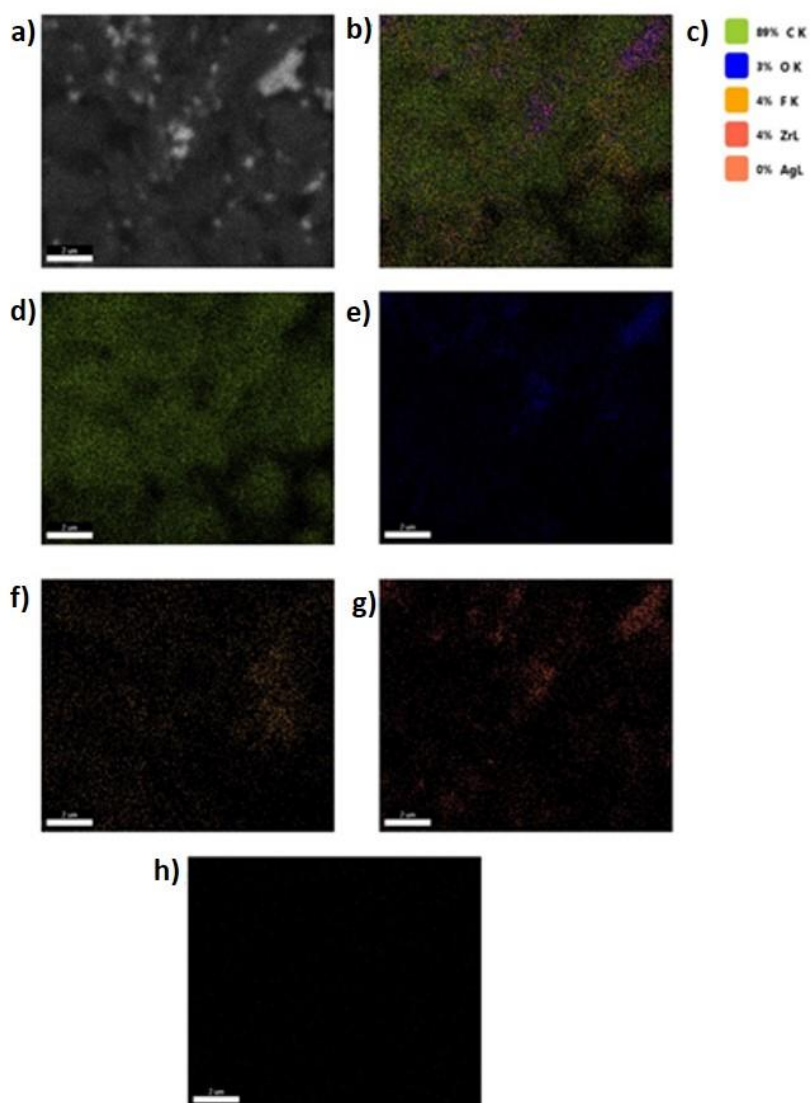


Figure 3.58 : EDAX results of 0,5mM AgNO₃ doped-PVDF carbon ink.

Table 3.15 : Resistivity results of 0,5 mM AgNO₃ doped PVDF carbon ink.

Thickness	Results	Sheet Resistance	Bulk Resistance (ohm*cm)
45 μm	433,48	1964,53	10,15
130 μm	290,33	1315,79	7,76
255 μm	140	634,48	5,65

3.3.3.3 0.75 mM silver nitrate doped PVDF results

Carbon ink with 0,75 mM silver nitrate was applied on the FTO substrate with different thickness. Surface properties was observed from real image (Figure 3.59) and optic microscope images (Figure 3.60) and confirmed that the thickest layer has the most uniform and regular surface.

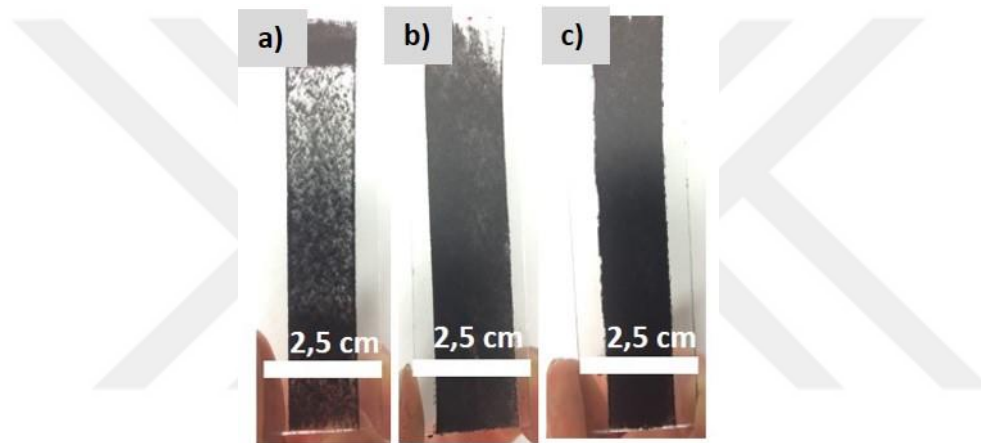


Figure 3.59 : Images of the 0,75 mM AgNO₃ doped-PVDF carbon ink with a) 45 μm b) 130 μm and c) 255 μm thickness.

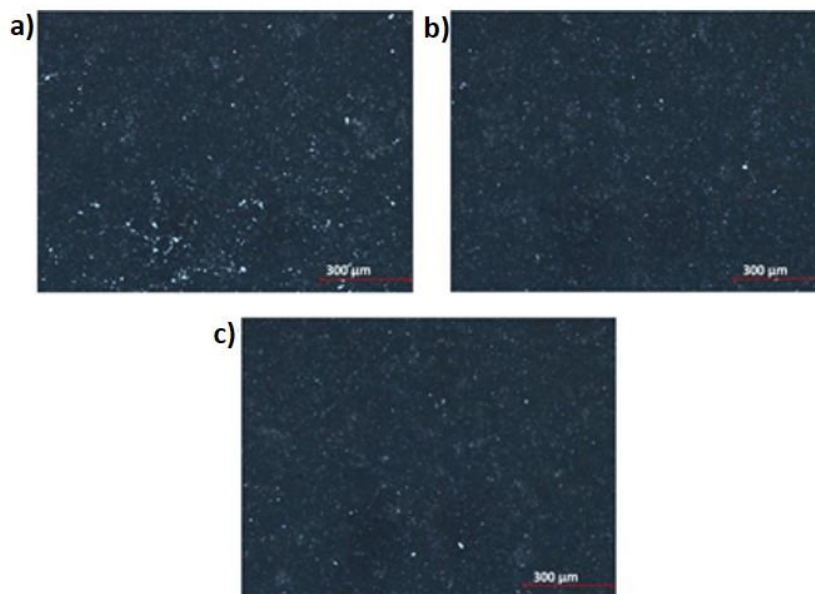


Figure 3.60 : Optic microscope images of 0,75 mM AgNO₃ doped-PVDF carbon ink with a) 45 μm b) 130 μm and c) 255 μm thickness.

Morphology and homogeneity of the carbon ink was characterized by SEM images (Figure 3.61) and EDAX results (Figure 3.61). Especially, SEM images with high magnification showed that uniformity of surface is poor. However, according to EDAX results, ingredients of ink were dispersed homogenously. Moreover, bulk resistivity is lower than 1,5 ohm*cm (Table 3.16).

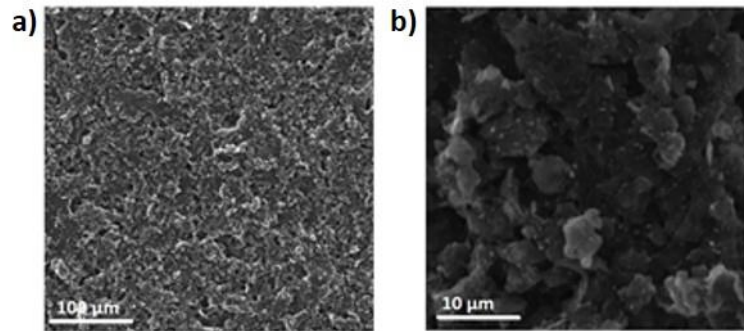


Figure 3.61 : SEM images a) 500x b) 5.00kx magnification of 0,75mM AgNO₃ doped-PVDF carbon ink.

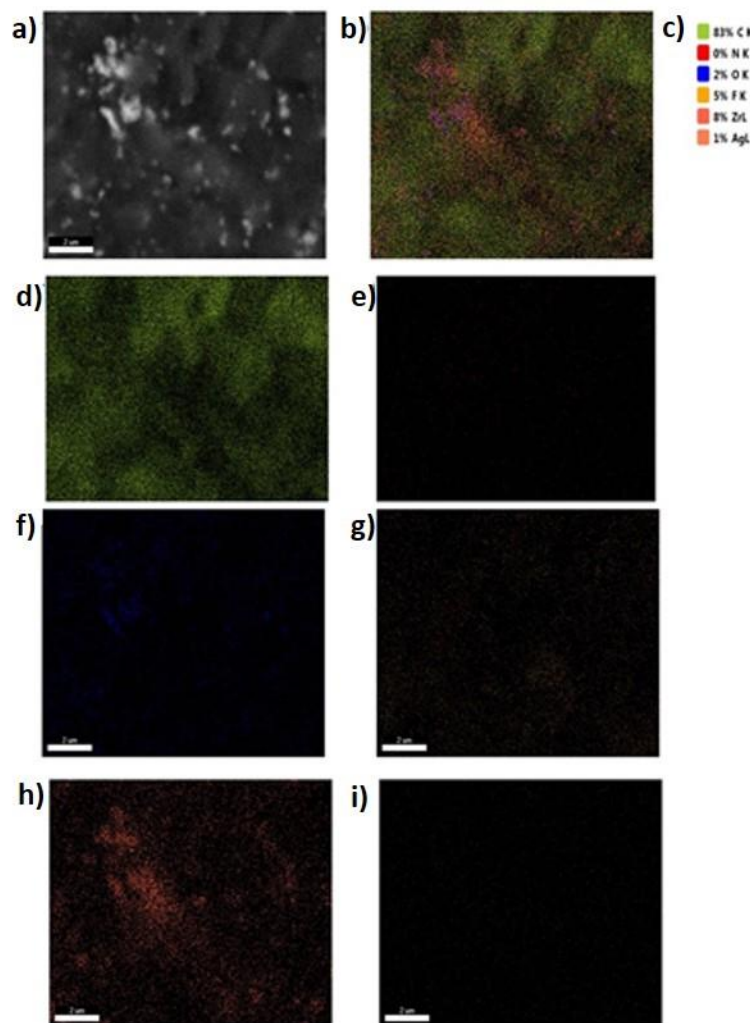


Figure 3.62 : EDAX results of 0,75mM AgNO₃ doped-PVDF carbon ink.

Table 3.16 : Resistivity results of 0,75 mM AgNO₃ doped PVDF carbon ink.

Thickness	Results	Sheet Resistance	Bulk Resistance (ohm*cm)
45 μm	168,33	762,89	1,47
130 μm	116,67	528,73	1,92
255 μm	84,58	383,33	2,15

3.3.3.4 1.0 mM silver nitrate doped PVDF results

Carbon ink with 1,0 mM silver nitrate was applied onto FTO. Real images (Figure 3.63) and optic microscope images (Figure 3.64) show how increasing thickness affect the uniformity of the film.

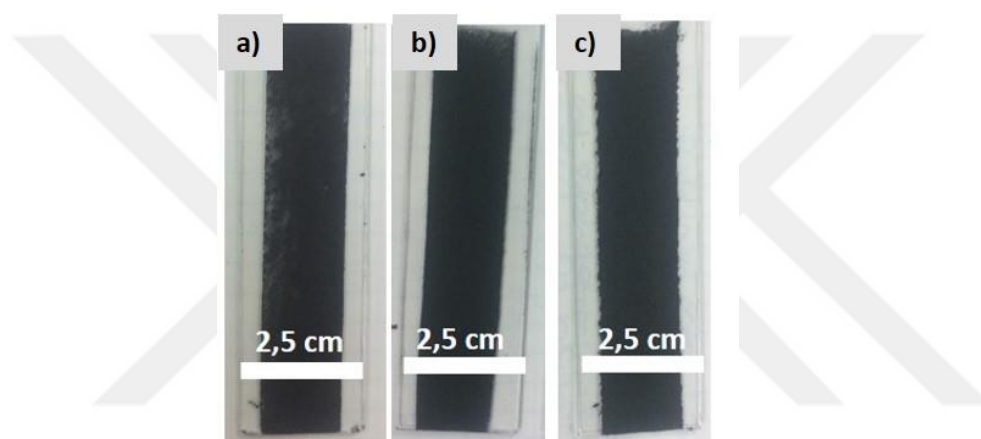


Figure 3.63 : Images of the 1,0 mM AgNO₃ doped-PVDF carbon ink with a) 45 μm b) 130 μm and c) 255 μm thickness.

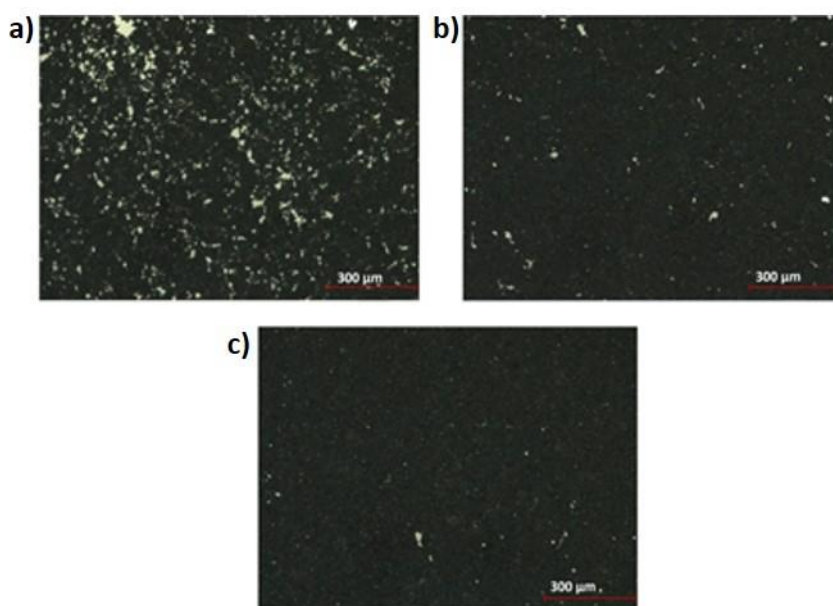


Figure 3.64 : Optic microscope images of 1,0 mM AgNO₃ doped-PVDF carbon ink with a) 45 μm b) 130 μm and c) 255 μm thickness.

Morphology and ingredients distribution of the ink were investigated by SEM images (Figure 3.65) and EDAX results (Figure 3.66). Micro-cracks were observed which normally caused to high resistivity of carbon ink. Despite that, ink's electrical conductivity is high, as shown in Table 3.17. Moreover, homogeneity is approved by EDAX images.

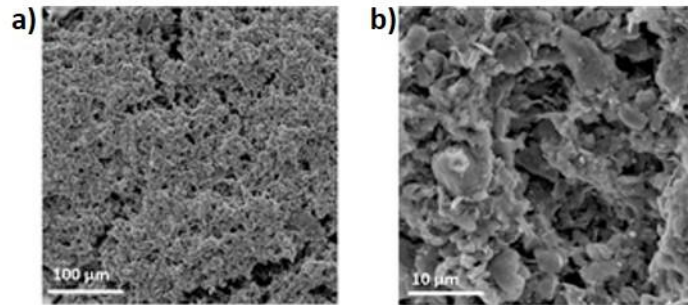


Figure 3.65 : SEM images a) 500x b) 5.00kx magnification of 1,0 mM AgNO₃ doped-PVDF carbon ink.

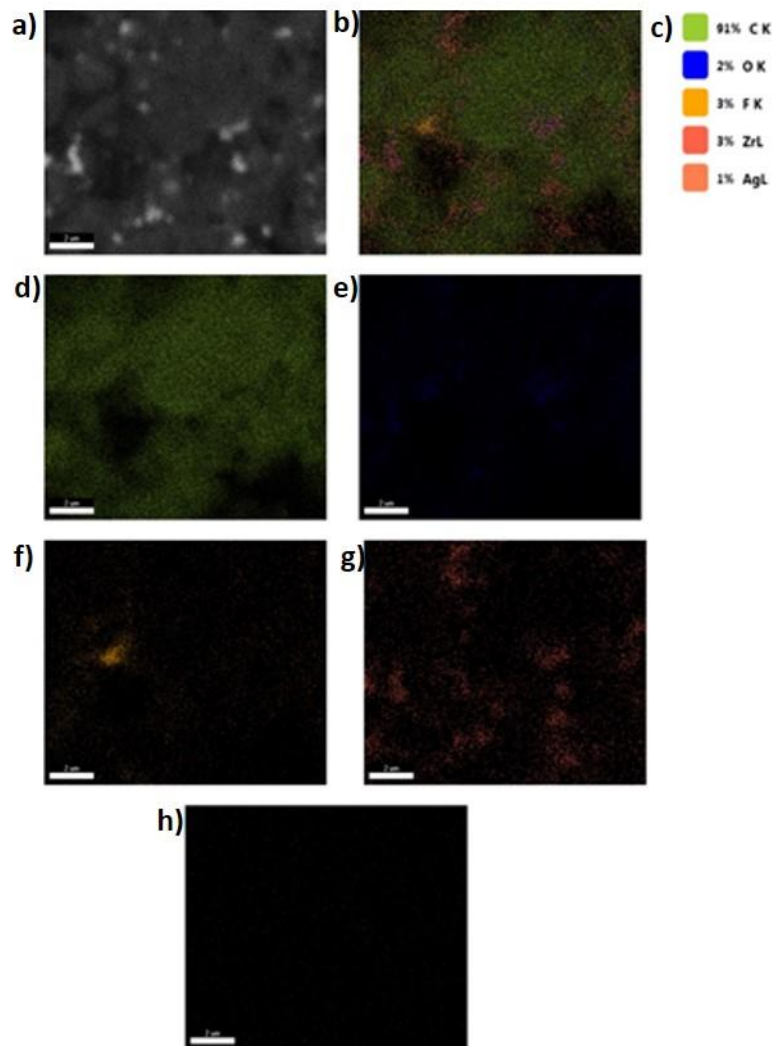


Figure 3.66 : EDAX results of 1,0 mM AgNO₃ doped-PVDF carbon ink.

Table 3.17 : Resistivity results of 1,0 mM AgNO₃ doped PVDF carbon ink.

Thickness	Results	Sheet Resistance	Bulk Resistance (ohm*cm)
45 μm	599,33	2716,18	6,25
130 μm	208	942,66	5,31
255 μm	85,24	386,29	3,95

3.4 Properties Of Environmentally Friendly and Polymer-Doped Low Temperature Processable Carbon-Based Conductive Ink

Carbon ink containing TC 1:2 30/70 and 1,0 mM silver nanoparticle was applied on FTO surfaces with different thickness. From the real and optical microscope images (Figure 3.67 and Figure 3.68) irregular surface were observed for the thinnest films, which improves when the number of layers increases. However, compared to the only silver nanoparticle contains ink surface, the surface of TC 1:2 30/70 and 1,0 mM silver nanoparticle carbon ink is more regular.

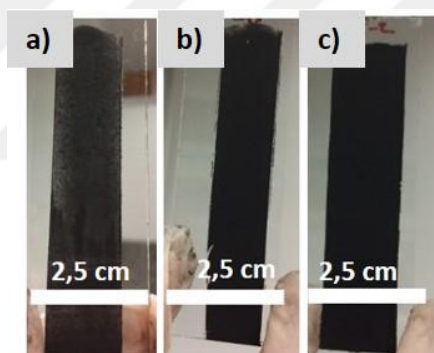


Figure 3.67 : Images of the TC 1:2 30:70 & 1,0 mM Ag doped-PVDF carbon ink with a) 45 μm b) 130 μm and c) 255 μm thickness.

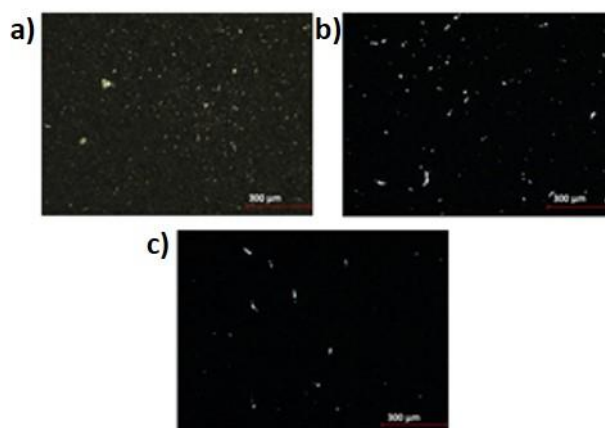


Figure 3.68 : Optic microscope images of TC 1:2 30:70 & 1,0 mM Ag doped-PVDF carbon ink with a) 45 μm b) 130 μm and c) 255 μm thickness.

According to SEM images (Figure 3.69) and EDAX results (Figure 3.70), surface uniformity and dispersion homogeneity were approved. However, the ink resistivity is higher than the silver and silver nitrate doped PVDF carbon ink (Table 1.1Table 3.18).

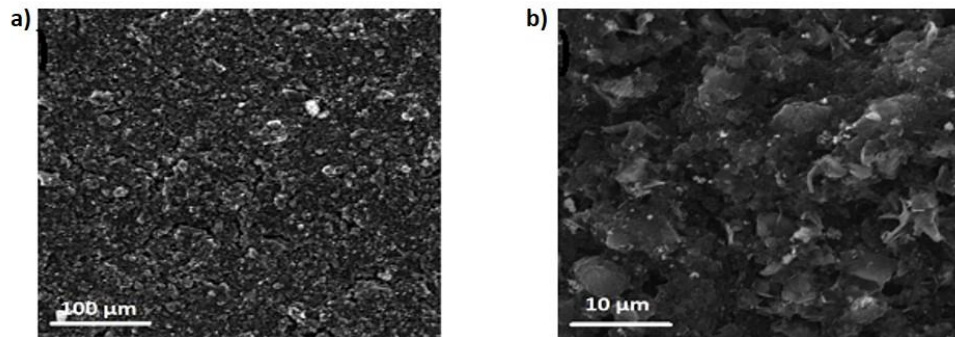


Figure 3.69 : SEM images a) 500x b) 5.00kx magnification of TC 1:2 30:70 & 1,0 mM Ag doped-PVDF carbon ink.

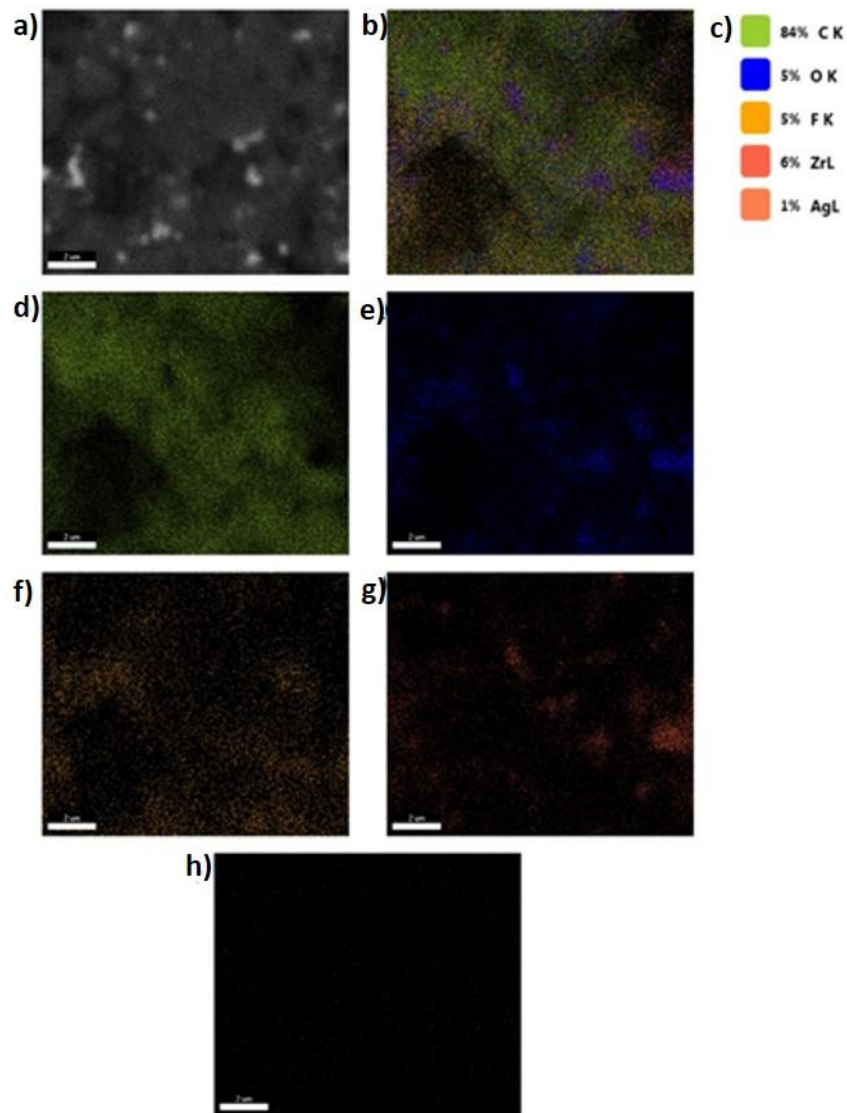


Figure 3.70 : EDAX results of TC 1:2 30:70 & 1,0 mM Ag doped-PVDF carbon ink.

Table 3.18 : Resistivity results of TC 1:2 30:70 & 1,0 mM Ag doped PVDF carbon ink.

Thickness	Results	Sheet Resistance	Bulk Resistance (ohm*cm)
45 μm	6560,67	29732,94	100,10
130 μm	1346,67	6103,09	23,40
255 μm	647,44	2934,21	13,50

Compared the silver and silver nitrate doped PVDF carbon inks (Figure 3.71), 0,5 Ag and 0,75 AgNO₃ doped-PVDF carbon inks showed the highest conductivity. However, increasing the Ag and AgNO₃ amount have the negative effect on the electrical conductivity of the inks. The reason for this Ag can create surface charges and defects on the polymer and/or high amount of Ag cause to agglomeration which leads to leakage current in the ink.

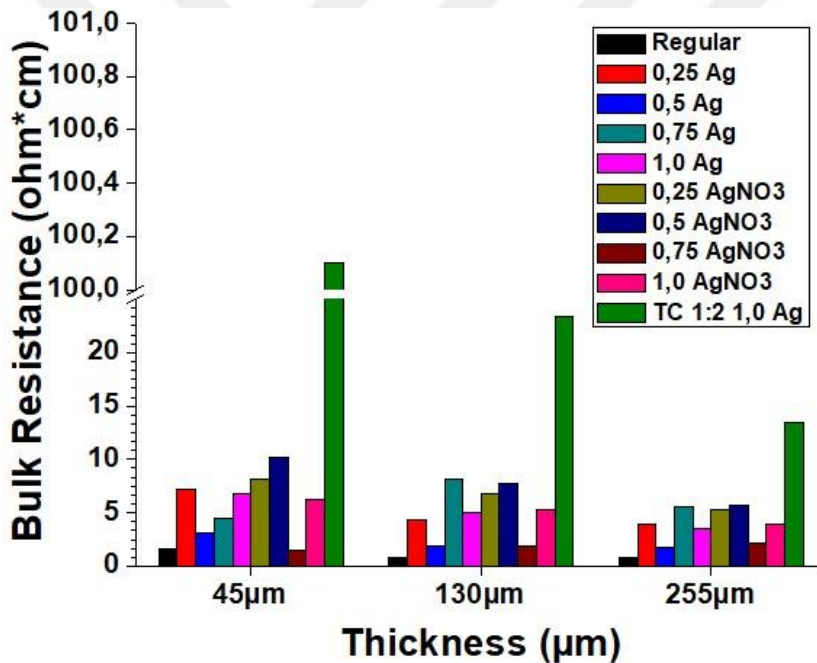


Figure 3.71 : Resistivity comparison of low temperature and doped polymer carbon inks.

3.5 Comparison of Perovskite Solar Cell Performance with Different Inks

To identifying solar cell performance, three parameters are used such as open-circuit voltage (V_{oc}), short-circuit current (J_{sc}) and fill factor (FF) [105]. To get high efficiency from the solar cell, these three parameters should be optimized at maximum value. FF depends on shunt (minor effect) and series resistance (main effect), the charge

transporting ability, recombination, and surface morphology of the layers. V_{oc} can be affected by recombination rate, surface morphology and crystalline structure of the solar cell materials and J_{sc} depends on the electron and hole transport channels and surface morphology of the layers. To improve the solar cell efficiency, perovskite should have the large crystal size and less crystal boundary, the low defect in its structure, enhance light harvesting ability and smooth surface, which lead to reduce leakage, better contact with the other layers and reduce the recombination rate of the cell. Also, carbon counter electrode contacts with the perovskite layer should be smooth and carbon should have large pore size, good electrical conductivity and optimized specific surface area [62,105,106]. According to perovskite solar cell results which are illustrated in Table 3.19, the solar cell with TC 1:2 30/70 carbon ink showed the highest efficiency compare to other solar cells. This can be a result of biowaste carbon's structure. TC 1:2 carbon has the largest mesoporous properties which can lead to improved hole transport channels, thus improve the J_{sc} . Moreover, TC 1:2 30/70 carbon ink has good conductivity and when applied to the solar cell it constituted a smooth layer that cause to the good interaction between the perovskite layer and carbon counter layer. Therefore, it is possible to prevent the leakage and decrease the resistivity and improve the FF and J_{sc} of the solar cell.

Table 3.19 : Comparison of the photovoltaic results of perovskite solar cells with carbon electrodes.

	Voc (V)	Jsc (mA/cm ²)	FF	Efficiency (%)	Series Resistance-Rs (ohm.cm ²)	Shunt Resistance- Rsh (ohm.cm ²)
Low T processable carbon ink	0,691	0,281	0,248	0,048	1729,33	1919,88
TC 1:2 30/70	0,897	9,991	0,506	4,534	976,48	1145,71
0.25 mM Ag	0,85	0,25	0,27	0,06	4361,35	3664,43
0.5 mM Ag	0,64	0,03	0,24	0,004	29817,52	20588,48
0.75 mM Ag	0,93	0,47	0,32	0,14	2503,64	2843,65
1.0 mM Ag	0,93	0,44	0,32	0,11	2653,97	2445,59
0.25 AgNO3 mM	0,85	0,03	0,26	0,006	20511,27	24244,67

Table 3.19 (continued): Comparison of the photovoltaic results of perovskite solar cells with carbon electrodes.

0.5 AgNO ₃ mM	0,92	0,29	0,27	0,07	2669,21	2911,76
0.75 AgNO ₃ mM	0,91	0,53	0,29	0,14	1989,38	1971,03
1.0 AgNO ₃ mM	0,85	0,17	0,31	0,05	4673,78	5101,26
TC 1:2 30:70 & 1,0 mM Ag	1,02	0,59	0,29	0,17	2401,54	2222,8

4. CONCLUSIONS AND RECOMMENDATIONS

To sum up in the first chapter, new, easy to process and low temperature carbon-based conductive ink was prepared and applied on the perovskite solar cell. According to literature, PVDF has not been used in carbon ink and this research shows that even 2,5wt% PVDF is sufficient to obtain regular film surface on FTO glass. Moreover, new type of ink can be dried at room temperature in 15 minutes without any heating. Low resistivity and homogeneity of the ink permit it to be used in application areas where high conductivity is need. However, the perovskite solar cell result was not sufficient. The reason behind it may be the printing process or the perovskite structure.

In the second chapter, from all activated carbon-based conductive ink TC 1:2 30/70 gave the best result. Its surface morphology is uniform, resistivity is very low and also gives the best power conversion efficiency compared to the other inks used in this thesis. Uniformity of the morphology may arise from high surface area of the particles. Also, continuous morphology affect the conductivity of the ink due to the fact that particles can interact with each other easily. It can also be said that TC 1:2 30/70 carbon ink have advantageous because it can be applied easily and its drying process takes only 15 minutes at standard temperature and humidity conditions.

In the third chapter, silver and silver nitrate doped PVDF carbon-based conductive ink was studied. According to all results, general trend of more homogenous and uniform surface and increased conductivity, with the increasment of the thickness of the ink layer was followed. Electrical resistivity results also show that, adding silver and silver nitrate enhance the conductivity. However when applied as electrodes on perovskite solar cell, the high efficiencies of perovskite solar cell couldn't be reached.

In summary, new and easy to process at low temperature carbon-based conductive ink can be prepared using PVDF as binder. Adding bio-waste carbon and/or Ag compounds into the ink can provide printed films with similar conductivities to some commercial inks [107–109]. However, during the study a problem with the printing technique was meet and non-uniform films were produced. Therefore, as further studies, the coating process can be improved or changed in order to obtain more regular

and uniform surface. Moreover, all carbon inks can be applied to different type of applications.



REFERENCES

- [1] **Url-1** < <https://www.iea.org/weo2017>>, date retrieved 03.05.2018.
- [2] **Url-2** < <https://yearbook.enerdata.net>>, date retrieved 03.05.2018.
- [3] **Url-3** < <https://www.worldenergy.org>>, date retrieved 03.05.2018.
- [4] **Kumar, J., Basu, B., Talukdar, F. A. and Nandi, A.** (2018) Graphene-based multimode inspired frequency reconfigurable user terminal antenna for satellite communication. *IET Communications* **12**, 67–74.
- [5] **K, V. A., R, V. K. R., Karthik, P. S. and Singh, S. P.** (2015) Copper conductive inks: synthesis and utilization in flexible electronics. *RSC Adv.* **5**, 63985–64030.
- [6] **Zhang, Q., Zheng, Y. and Liu, J.** (2012) Direct writing of electronics based on alloy and metal (DREAM) ink: A newly emerging area and its impact on energy, environment and health sciences. *Front. Energy* **6**, 311–340.
- [7] **Cui, W., Lu, W., Zhang, Y., Lin, G., Wei, T. and Jiang, L.** (2010) Gold nanoparticle ink suitable for electric-conductive pattern fabrication using ink-jet printing technology. *Colloids and Surfaces A: Physicochemical and Engineering Aspects* **358**, 35–41.
- [8] **Tang, C., Xing, B., Hu, G., Huang, F. and Zuo, C.** (2017) A facile microwave approach to the fast-and-direct production of silver nano-ink. *Materials Letters* **188**, 220–223.
- [9] **Choi, J. H., Ryu, K., Park, K. and Moon, S.-J.** (2015) Thermal conductivity estimation of inkjet-printed silver nanoparticle ink during continuous wave laser sintering. *International Journal of Heat and Mass Transfer* **85**, 904–909.
- [10] **Lee, I., Ryu, K., Park, K.-H., Moon, Y.-J., Hwang, J.-Y. and Moon, S.-J.** (2017) Temperature effect on physical properties and surface morphology of printed silver ink during continuous laser scanning sintering. *International Journal of Heat and Mass Transfer* **108**, 1960–1968.
- [11] **Lee, D.-G., Kim, D. K., Moon, Y.-J. and Moon, S.-J.** (2013) Effect of temperature on electrical conductance of inkjet-printed silver nanoparticle ink during continuous wave laser sintering. *Thin Solid Films* **546**, 443–447.
- [12] **Niittynen, J., Abbel, R., Mäntysalo, M., Perelaer, J., Schubert, U. S. and Lupo, D.** (2014) Alternative sintering methods compared to conventional thermal sintering for inkjet printed silver nanoparticle ink. *Thin Solid Films* **556**, 452–459.
- [13] **Zhang, W., Bi, E., Li, M. and Gao, L.** (2016) Synthesis of Ag/RGO composite as effective conductive ink filler for flexible inkjet printing electronics. *Colloids and Surfaces A: Physicochemical and Engineering Aspects* **490**, 232–240.
- [14] **Kim, D., Lee, I., Yoo, Y., Moon, Y.-J. and Moon, S.-J.** (2014) Transient variation of a cross-sectional area of inkjet-printed silver nanoparticle ink during furnace sintering. *Applied Surface Science* **305**, 453–458.

- [15] **Theodorakos, I., Zacharatos, F., Geremia, R., Karnakis, D. and Zergioti, I.** (2015) Selective laser sintering of Ag nanoparticles ink for applications in flexible electronics. *Applied Surface Science* **336**, 157–162.
- [16] **Stempien, Z., Rybicki, E., Rybicki, T. and Lesnikowski, J.** (2016) Inkjet-printing deposition of silver electro-conductive layers on textile substrates at low sintering temperature by using an aqueous silver ions-containing ink for textronic applications. *Sensors and Actuators B: Chemical* **224**, 714-725.
- [17] **Min, H., Lee, B., Jeong, S. and Lee, M.** (2017) Fabrication of 10 μm -scale conductive Cu patterns by selective laser sintering of Cu complex ink. *Optics & Laser Technology* **88**, 128-133.
- [18] **Gulen, M., Sarilmaz, A., Patir, I. H., Ozel, F. and Sonmezoglu, S.** (2018) Ternary copper-tungsten-disulfide nanocube inks as catalyst for highly efficient dye-sensitized solar cells. *Electrochimica Acta* **269**, 119–127.
- [19] **Kim, C. K., Lee, G.-J., Lee, M. K. and Rhee, C. K.** (2014) A novel method to prepare Cu@Ag core-shell nanoparticles for printed flexible electronics. *Powder Technology* **263**, 1–6.
- [20] **Min, H., Lee, B., Jeong, S. and Lee, M.** (2016) Laser-direct process of Cu nano-ink to coat highly conductive and adhesive metallization patterns on plastic substrate. *Optics and Lasers in Engineering* **80**, 12–16.
- [21] **Li, W., Li, W., Wei, J., Tan, J. and Chen, M.** (2014) Preparation of conductive Cu patterns by directly writing using nano-Cu ink. *Materials Chemistry and Physics* **146**, 82–87.
- [22] **Kawaguchi, Y., Hotta, Y. and Kawasaki, H.** (2017) Cu-based composite inks of a self-reductive Cu complex with Cu flakes for the production of conductive Cu films on cellulose paper. *Materials Chemistry and Physics* **197**, 87–93.
- [23] **Li, W., Li, L., Gao, Y., Hu, D., Li, C.-F., Zhang, H., Jiu, J., Nagao, S. and Suganuma, K.** (2018) Highly conductive copper films based on submicron copper particles/copper complex inks for printed electronics: Microstructure, resistivity, oxidation resistance, and long-term stability. *Journal of Alloys and Compounds* **732**, 240–247.
- [24] **Pajor-Świerzy, A., Farraj, Y., Kamyshny, A. and Magdassi, S.** (2017) Air stable copper-silver core-shell submicron particles: Synthesis and conductive ink formulation. *Colloids and Surfaces A: Physicochemical and Engineering Aspects* **521**, 272–280.
- [25] **Pajor-Świerzy, A., Farraj, Y., Kamyshny, A. and Magdassi, S.** (2017) Effect of carboxylic acids on conductivity of metallic films formed by inks based on copper@silver core-shell particles. *Colloids and Surfaces A: Physicochemical and Engineering Aspects* **522**, 320–327.
- [26] **Dai, X., Xu, W., Zhang, T. and Wang, T.** (2018) Self-Reducible Cu Nanoparticles for Conductive Inks. *Ind. Eng. Chem. Res.* **57**, 2508–2516.
- [27] **Lee, Y. J., Lee, C. and Lee, H. M.** (2018) Synthesis of oxide-free aluminum nanoparticles for application to conductive film. *Nanotechnology* **29**, 055602.
- [28] **Sergeev, A. S., Tameev, A. R., Zolotarevskii, V. I. and Vannikov, A. V.** (2018) Electrically Conductive Inks Based on Polymer Composition for Inkjet Printing. *Inorg. Mater. Appl. Res.* **9**, 147–150.

- [29] **Chang-Jian, C.-W., Cho, E.-C., Yen, S.-C., Ho, B.-C., Lee, K.-C., Huang, J.-H. and Hsiao, Y.-S.** (2018) Facile preparation of WO₃/PEDOT:PSS composite for inkjet printed electrochromic window and its performance for heat shielding. *Dyes and Pigments* **148**, 465–473.
- [30] **Pal, R. K., Pradhan, S., Narayanan, L. and Yadavalli, V. K.** (2018) Micropatterned conductive polymer biosensors on flexible PDMS films. *Sensors and Actuators B: Chemical* **259**, 498-504.
- [31] **Crouch, E., Cowell, D. C., Hoskins, S., Pittson, R. W. and Hart, J. P.** (2005) A novel, disposable, screen-printed amperometric biosensor for glucose in serum fabricated using a water-based carbon ink. *Biosensors and Bioelectronics* **21**, 712–718.
- [32] **(Kelvin) Fu, K., Padbury, R., Toprakci, O., Dirican, M. and Zhang, X.** (2018) 13 - Conductive textiles. In *Engineering of High-Performance Textiles* (Miao, M., and Xin, J. H., eds.), pp 305–334, Woodhead Publishing.
- [33] **Thangakameshwaran, N. and Santhoskumar, A. U.** (2014) Cotton Fabric Dipped in Carbon Nano Tube Ink for Smart Textile Applications. *International Journal of Polymeric Materials and Polymeric Biomaterials* **63**, 557–562.
- [34] **Hu, L., Pasta, M., Mantia, F. L., Cui, L., Jeong, S., Deshazer, H. D., Choi, J. W., Han, S. M. and Cui, Y.** (2010) Stretchable, Porous, and Conductive Energy Textiles. *Nano Letters* **10**, 708–714.
- [35] **Alamer, F. A.** (2018) Structural and electrical properties of conductive cotton fabrics coated with the composite polyaniline/carbon black. *Cellulose* **25**, 2075–2082.
- [36] **Sheng, Y., John, O. and Stephen, B.** (2018) Solid-State Supercapacitor Fabricated in a Single Woven Textile Layer for E-Textiles Applications. *Advanced Engineering Materials* **20**, 1700860.
- [37] **Paleo, A. J., Staiti, P., Brigandi, A., Ferreira, F. N., Rocha, A. M. and Lufrano, F.** (2018) Supercapacitors based on AC/MnO₂ deposited onto dip-coated carbon nanofiber cotton fabric electrodes. *Energy Storage Materials* **12**, 204–215.
- [38] **Jian, Z., Xuezhong, X., Yangyang, X. and Gilles, L.** (2018) Coaxial Thermoplastic Elastomer-Wrapped Carbon Nanotube Fibers for Deformable and Wearable Strain Sensors. *Advanced Functional Materials* **28**, 1705591.
- [39] **Zhu, X., Chen, X., Yang, Z., Liu, Y., Zhou, Z. and Ren, Z.** (2018) Investigating the influences of electrode material property on degradation behavior of organic wastewaters by iron-carbon micro-electrolysis. *Chemical Engineering Journal* **338**, 46–54.
- [40] **Fischer, T., Rühling, J., Wetzold, N., Zillger, T., Weissbach, T., Göschel, T., Würfel, M., Hübler, A. and Kroll, L.** (2018) Roll-to-roll printed carbon nanotubes on textile substrates as a heating layer in fiber-reinforced epoxy composites. *Journal of Applied Polymer Science* **135**, 45950.
- [41] **Wilson, J. S.** (Ed.). (2005) CHAPTER 1 - Sensor Fundamentals. In *Sensor Technology Handbook*, pp 1–20, Newnes, Burlington.
- [42] **Feng, X., Chen, W. and Yan, L.** (2015) Free-standing dried foam films of graphene oxide for humidity sensing. *Sensors and Actuators B: Chemical* **215**, 316–322.
- [43] **Mehrotra, P.** (2016) Biosensors and their applications – A review. *J Oral Biol Craniofac Res* **6**, 153–159.

- [44] **Chen, J.-C., Chung, H.-H., Hsu, C.-T., Tsai, D.-M., Kumar, A. S. and Zen, J.-M.** (2005) A disposable single-use electrochemical sensor for the detection of uric acid in human whole blood. *Sensors and Actuators B: Chemical* **110**, 364–369.
- [45] **Dias, A. C. M. S., Gomes-Filho, S. L. R., Silva, M. M. S. and Dutra, R. F.** (2013) A sensor tip based on carbon nanotube-ink printed electrode for the dengue virus NS1 protein. *Biosens Bioelectron* **44**, 216–221.
- [46] **Wang, J., Pamidi, P. V. A. and Park, D. S.** (1996) Screen-Printable Sol–Gel Enzyme-Containing Carbon Inks. *Analytical Chemistry* **68**, 2705–2708.
- [47] **Dossi, N., Toniolo, R., Pizzariello, A., Carrilho, E., Piccin, E., Battiston, S. and Bontempelli, G.** (2012) An electrochemical gas sensor based on paper supported room temperature ionic liquids. *Lab on a Chip* **12**, 153–158.
- [48] **Hassan, G., Bae, J., Lee, C. H. and Hassan, A.** (2018) Wide range and stable ink-jet printed humidity sensor based on graphene and zinc oxide nanocomposite. *J Mater Sci: Mater Electron* **29**, 5806–5813.
- [49] **Li, J.-P., Peng, T.-Z. and Fang, C.** (2002) Screen-printable sol–gel ceramic carbon composite pH sensor with a receptor zeolite. *Analytica Chimica Acta* **455**, 53–60.
- [50] **Liu, Y., Zheng, H. and Liu, M.** (2018) High performance strain sensors based on chitosan/carbon black composite sponges. *Materials & Design* **141**, 276–285.
- [51] **Rivnay, J., Owens, R. M. and Malliaras, G. G.** (2014) The Rise of Organic Bioelectronics. *Chem. Mater.* **26**, 679–685.
- [52] **Chong, C., Jianguang, Z., Shuang, L., Yi, X., Chuanxiong, N., Zhenqiang, S., Luis, C.-C. J., Nan, M. and Rainer, H.** (2017) A Water-Processable and Bioactive Multivalent Graphene Nanoink for Highly Flexible Bioelectronic Films and Nanofibers. *Advanced Materials* **30**, 1705452.
- [53] **Kuzmenko, V., Karabulut, E., Pernevik, E., Enoksson, P. and Gatenholm, P.** (2018) Tailor-made conductive inks from cellulose nanofibrils for 3D printing of neural guidelines. *Carbohydrate Polymers* **189**, 22–30.
- [54] **Zhi, M., Xiang, C., Li, J., Li, M. and Wu, N.** (2012) Nanostructured carbon–metal oxide composite electrodes for supercapacitors: a review. *Nanoscale* **5**, 72–88.
- [55] **Url-4** < <https://www.britannica.com> >, date retrieved 03.05.2018.
- [56] **Sharma, S., Siwach, B., Ghoshal, S.K. and Mohan, D.** (2017) Dye sensitized solar cells: From genesis to recent drifts. *Renewable and Sustainable Energy Reviews* **70**, 529–537.
- [57] **Kojima, A., Teshima, K., Shirai, Y. and Miyasaka, T.** (2009) Organometal Halide Perovskites as Visible-Light Sensitizers for Photovoltaic Cells. *Journal of the American Chemical Society* **131**, 6050–6051.
- [58] **Yang, X., Wang, H., Cai, B., Yu, Z. and Sun, L.** (2018) Progress in hole-transporting materials for perovskite solar cells. *Journal of Energy Chemistry* **27**, 650–672.
- [59] **Assadi, M. K., Bakhoda, S., Saidur, R. and Hanaei, H.** (2018) Recent progress in perovskite solar cells. *Renewable and Sustainable Energy Reviews* **81**, 2812–2822.
- [60] **Kim, H.-S., Lee, C.-R., Im, J.-H., Lee, K.-B., Moehl, T., Marchioro, A., Moon, S.-J., Humphry-Baker, R., Yum, J.-H., Moser, J. E., et al.** (2012)

- Lead Iodide Perovskite Sensitized All-Solid-State Submicron Thin Film Mesoscopic Solar Cell with Efficiency Exceeding 9%. *Sci Rep* **2**.
- [61] **Yang, W. S., Park, B.-W., Jung, E. H., Jeon, N. J., Kim, Y. C., Lee, D. U., Shin, S. S., Seo, J., Kim, E. K., Noh, J. H., et al.** (2017) Iodide management in formamidinium-lead-halide-based perovskite layers for efficient solar cells. *Science* **356**, 1376–1379.
- [62] **Duan, M., Hu, Y., Mei, A., Rong, Y. and Han, H.** (2018) Printable carbon-based hole-conductor-free mesoscopic perovskite solar cells: From lab to market. *Materials Today Energy* **7**, 221–231.
- [63] **Ku, Z., Rong, Y., Xu, M., Liu, T. and Han, H.** (2013) Full Printable Processed Mesoscopic CH₃NH₃PbI₃/TiO₂ Heterojunction Solar Cells with Carbon Counter Electrode. *Scientific Reports* **3**, 3132."
- [64] **Mei, A., Li, X., Liu, L., Ku, Z., Liu, T., Rong, Y., Xu, M., Hu, M., Chen, J., Yang, Y., et al.** (2014) A hole-conductor-free, fully printable mesoscopic perovskite solar cell with high stability. *Science* **345**, 295–298.
- [65] **Yue, H., Si, S., Anyi, M., Yaoguang, R., Huawei, L., Xiong, L. and Hongwei, H.** (2017) Stable Large-Area (10 × 10 cm²) Printable Mesoscopic Perovskite Module Exceeding 10% Efficiency. *Solar RRL* **1**, 1600019.
- [66] **Liu, S., Cao, K., Li, H., Song, J., Han, J., Shen, Y. and Wang, M.** (2017) Full printable perovskite solar cells based on mesoscopic TiO₂/Al₂O₃/NiO (carbon nanotubes) architecture. *Solar Energy* **144**, 158–165.
- [67] **Duan, M., Rong, Y., Mei, A., Hu, Y., Sheng, Y., Guan, Y. and Han, H.** (2017) Efficient hole-conductor-free, fully printable mesoscopic perovskite solar cells with carbon electrode based on ultrathin graphite. *Carbon* **120**, 71–76.
- [68] **Jiang, P., Jones, T. W., Duffy, N. W., Anderson, K. F., Bennett, R., Grigore, M., Marvig, P., Xiong, Y., Liu, T., Sheng, Y., et al.** (2018) Fully printable perovskite solar cells with highly-conductive, low-temperature, perovskite-compatible carbon electrode. *Carbon* **129**, 830–836.
- [69] **Yue, G., Chen, D., Wang, P., Zhang, J., Hu, Z. and Zhu, Y.** (2016) Low-temperature prepared carbon electrodes for hole-conductor-free mesoscopic perovskite solar cells. *Electrochimica Acta* **218**, 84–90.
- [70] **Tao, H., Li, Y., Zhang, C., Wang, K., Wang, J., Tan, B., Han, L. and Tao, J.** (2018) High permeable microporous structured carbon counter electrode assisted by polystyrene sphere for fully printable perovskite solar cells. *Solid State Communications* **271**, 71–75.
- [71] **Mali, S. S., Kim, H., Kim, H. H., Park, G. R., Shim, S. E. and Hong, C. K.** (2017) Large area, waterproof, air stable and cost effective efficient perovskite solar cells through modified carbon hole extraction layer. *Materials Today Chemistry* **4**, 53–63.
- [72] **Gopi, C. V. V. M., Venkata-Haritha, M., Prabakar, K. and Kim, H.-J.** (2017) Low-temperature easy-processed carbon nanotube contact for high-performance metal- and hole-transporting layer-free perovskite solar cells. *Journal of Photochemistry and Photobiology A: Chemistry* **332**, 265–272.
- [73] **Zhang, R., Chen, Y., Xiong, J. and Liu, X.** (2018) Synergistic carbon-based hole transporting layers for efficient and stable perovskite solar cells. *J Mater Sci* **53**, 4507–4514.

- [74] **Chu, Q.-Q., Ding, B., Li, Y., Gao, L., Qiu, Q., Li, C.-X., Li, C.-J., Yang, G.-J. and Fang, B.** (2017) Fast Drying Boosted Performance Improvement of Low-Temperature Paintable Carbon-Based Perovskite Solar Cell. *ACS Sustainable Chem. Eng.* **5**, 9758–9765.
- [75] **Liu, Z., Sun, B., Zhong, Y., Liu, X., Han, J., Shi, T., Tang, Z. and Liao, G.** (2017) Novel integration of carbon counter electrode based perovskite solar cell with thermoelectric generator for efficient solar energy conversion. *Nano Energy* **38**, 457–466.
- [76] **Duan, M., Tian, C., Hu, Y., Mei, A., Rong, Y., Xiong, Y., Xu, M., Sheng, Y., Jiang, P., Hou, X., et al.** (2017) Boron-Doped Graphite for High Work Function Carbon Electrode in Printable Hole-Conductor-Free Mesoscopic Perovskite Solar Cells. *ACS Appl. Mater. Interfaces* **9**, 31721–31727.
- [77] **Zhang, L., Liu, T., Liu, L., Hu, M., Yang, Y., Mei, A. and Han, H.** (2015) The effect of carbon counter electrodes on fully printable mesoscopic perovskite solar cells. *J. Mater. Chem. A* **3**, 9165–9170.
- [78] **Url-5** < <https://www.thoughtco.com/definition-of-electrical-conductivity-605064>>, date retrieved 19.05.2018.
- [79] **Url-6** < <https://www.thoughtco.com/the-most-conductive-element-606683>>, date retrieved 19.05.2018.
- [80] **Url-7** < <https://www.thoughtco.com/table-of-electrical-resistivity-conductivity-608499>>, date retrieved 19.05.2018.
- [81] **Shetzline, J. A. and Creager, S. E.** (2014) Quantifying Electronic and Ionic Conductivity Contributions in Carbon/Polyelectrolyte Composite Thin Films. *J. Electrochem. Soc.* **161**, H917–H923.
- [82] **Url-8** < <https://www.britannica.com/science/band-theory>>, date retrieved 21.05.2018.
- [83] **Url-9** < <http://hyperphysics.phy-astr.gsu.edu/hbase/Solids/Fermi.html>>, date retrieved 21.05.2018.
- [84] **Url-10** < <http://hyperphysics.phy-astr.gsu.edu/hbase/Solids/band.html#c5>>, date retrieved 21.05.2018.
- [85] **Owen, J.** (1989) 21 - Ionic Conductivity. In *Comprehensive Polymer Science and Supplements* (Allen, G., and Bevington, J. C., eds.), pp 669–686, Pergamon, Amsterdam.
- [86] **Goldstein, J. I., Newbury, D. E., Echlin, P., Joy, D. C., Lyman, C. E., Lifshin, E., Sawyer, L. and Michael, J. R.** (2003) *The SEM and Its Modes of Operation. In Scanning Electron Microscopy and X-ray Microanalysis*, pp 21–60, Springer, Boston, MA.
- [87] **Lowell, S., Shields, J. E., Thomas, M. A. and Thommes, M.** (2004) Surface Area Analysis from the Langmuir and BET Theories. In *Characterization of Porous Solids and Powders: Surface Area, Pore Size and Density*, pp 58–81, Springer, Dordrecht.
- [88] Resistivity Measurements Using the Model 2450 SourceMeter® SMU Instrument and a Four-Point Collinear Probe, Application Note Series, KEITHLEY.
- [89] **Vig, J. R.** (1979) UV/Ozone Cleaning of Surfaces: A Review. In *Surface Contamination*, pp 235–254, Springer, Boston, MA.
- [90] **Url-11** < <http://www.techvision.co.jp/english/products/ozone.htm> >, date retrieved 18.05.2018.

- [91] **Sahu, N., Parija, B. and Panigrahi, S.** (2009) Fundamental understanding and modeling of spin coating process: A review. *Indian J Phys* **83**, 493–502.
- [92] **Url-12** < <https://www.ossila.com/pages/spin-coating>>, date retrieved 18.05.2018.
- [93] **Berni, A., Mennig, M. and Schmidt, H.** (2004) Doctor Blade. In *Sol-Gel Technologies for Glass Producers and Users*, pp 89–92, Springer, Boston, MA.
- [94] **Yang, L., Wang, W. J., Song, B., Wu, R., Li, J., Sun, Y. F., Shang, F., Chen, X. L. and Jian, J. K.** (2010) Novel route to scalable synthesis of II–VI semiconductor nanowires: Catalyst-assisted vacuum thermal evaporation. *Journal of Crystal Growth* **312**, 2852–2856.
- [95] **Url-13** <http://users.wfu.edu/ucerkb/Nan242/L06-Vacuum_Evaporation.pdf>, date retrieved 18.05.2018.
- [96] **Url-14** < <http://www.sciencetech-inc.com/all-products/light-sources/solar-simulators.html> >, date retrieved 18.05.2018.
- [97] **Url-15** < <http://plasticphotovoltaics.org/lc/characterization/lc-measure.html>>, date retrieved 18.05.2018.
- [98] **Rosenburg, F., Ionescu, E., Nicoloso, N. and Riedel, R.** (2018) High-Temperature Raman Spectroscopy of Nano-Crystalline Carbon in Silicon Oxycarbide. *Materials (Basel)* **11**.
- [99] **Landers, J., Gor, G. Y. and Neimark, A. V.** (2013) Neimark Density functional theory methods for characterization of porous materials. *Colloids and Surfaces A: Physicochemical and Engineering Aspects* **437**, 3–32.
- [100] **Rajendran, S., Sivakumar, M., Subadevi, R. and Nirmala, M.** (2004) Characterization of PVA–PVdF based solid polymer blend electrolytes. *Physica B: Condensed Matter* **348**, 73–78.
- [101] **Manna, S., Batabyal, S. K. and Nandi, A. K.** (2006) Preparation and Characterization of Silver–Poly(vinylidene fluoride) Nanocomposites: Formation of Piezoelectric Polymorph of Poly(vinylidene fluoride). *J. Phys. Chem. B* **110**, 12318–12326.
- [102] **Liu, T., Li, X., Wang, D., Huang, Q., Liu, Z., Li, N. and Xiao, C.** (2017) Superhydrophobicity and regeneration of PVDF/SiO₂ composite films. *Applied Surface Science* **396**, 1443–1449.
- [103] **Ince-Gunduz, B. S., Alpern, R., Amare, D., Crawford, J., Dolan, B., Jones, S., Kobylarz, R., Reveley, M. and Cebe, P.** (2010) Impact of nanosilicates on poly(vinylidene fluoride) crystal polymorphism: Part 1. Melt-crystallization at high supercooling. *Polymer* **51**, 1485–1493.
- [104] **Mandal, D., Henkel, K. and Schmeisser, D.** (2011) Comment on “Preparation and Characterization of Silver–Poly(vinylidene fluoride) Nanocomposites: Formation of Piezoelectric Polymorph of Poly(vinylidene fluoride).” *J. Phys. Chem. B* **115**, 10567–10569.
- [105] **Wu, N., Wu, Y., Walter, D., Shen, H., Duong, T., Grant, D., Barugkin, C., Fu, X., Peng, J., White, T., et al.** (2017) Identifying the Cause of Voltage and Fill Factor Losses in Perovskite Solar Cells by Using Luminescence Measurements. *Energy Technology* **5**, 1827–1835.
- [106] **Yan, W., Li, Y., Ye, S., Li, Y., Rao, H., Liu, Z., Wang, S., Bian, Z. and Huang, C.** (2016) Increasing open circuit voltage by adjusting work function of hole-transporting materials in perovskite solar cells. *Nano Res.* **9**, 1600–1608.

- [107] **Url-16** < <http://shop.solaronix.com/perovskite-cell-components/conductive-carbon-layer-paste/elcocarb-b-sp.html> >, date retrieved 11.07.2018.
- [108] **Url-17** < <https://www.mgchemicals.com/products/greases-and-lubricants/conductive-greases/carbon-conductive-assembly-paste-847> >, date retrieved 11.07.2018.
- [109] **Url-18** < <http://www.creativematerials.com/products/carbon-inks> >, date retrieved 11.07.2018.



APPENDICES

APPENDIX A

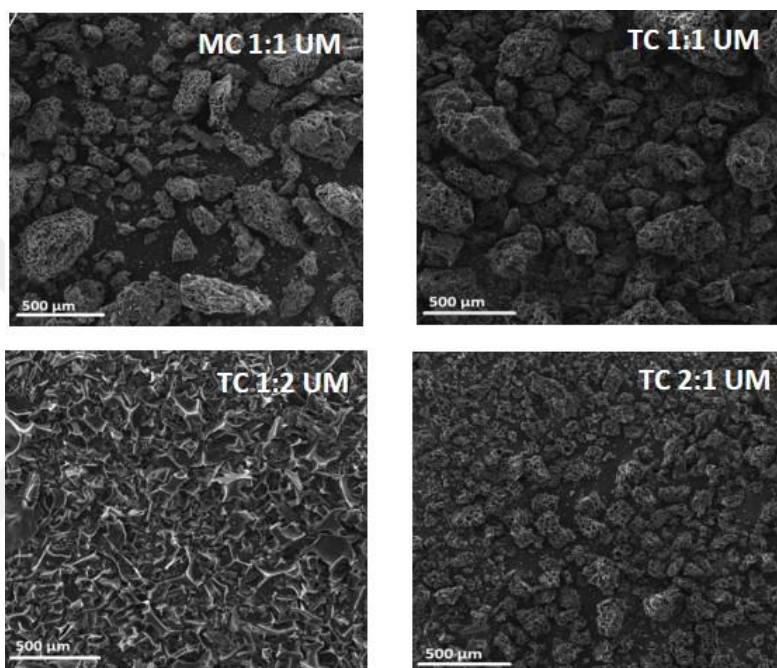


Figure A.1 : SEM images of unball milled coffee-waste carbon particles with 500x magnification.

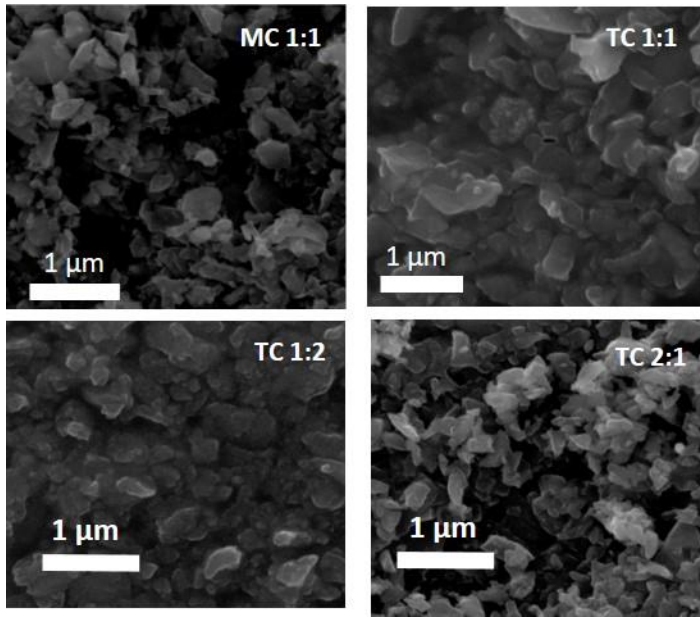


Figure A.2 : SEM images of ball milled coffee-waste carbon particles with 50.00kx magnification.

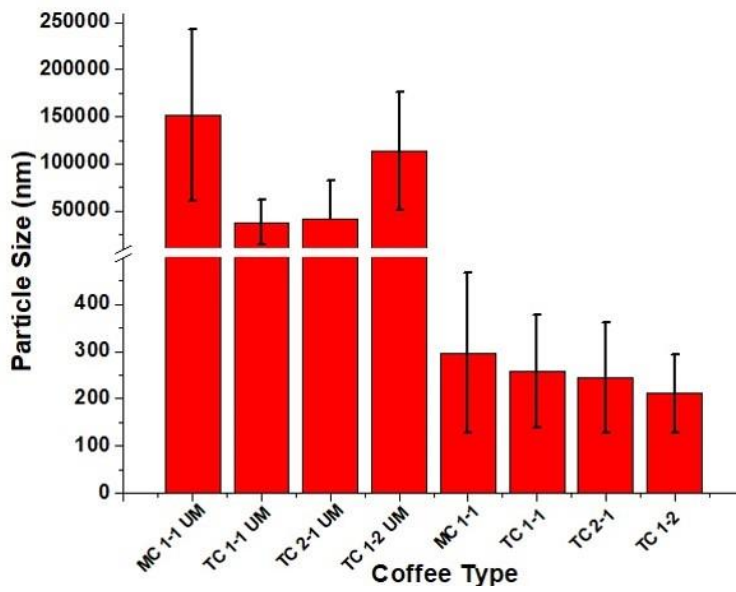


Figure A.3 : Particle size of unball milled and ball milled coffee-waste carbon particles.

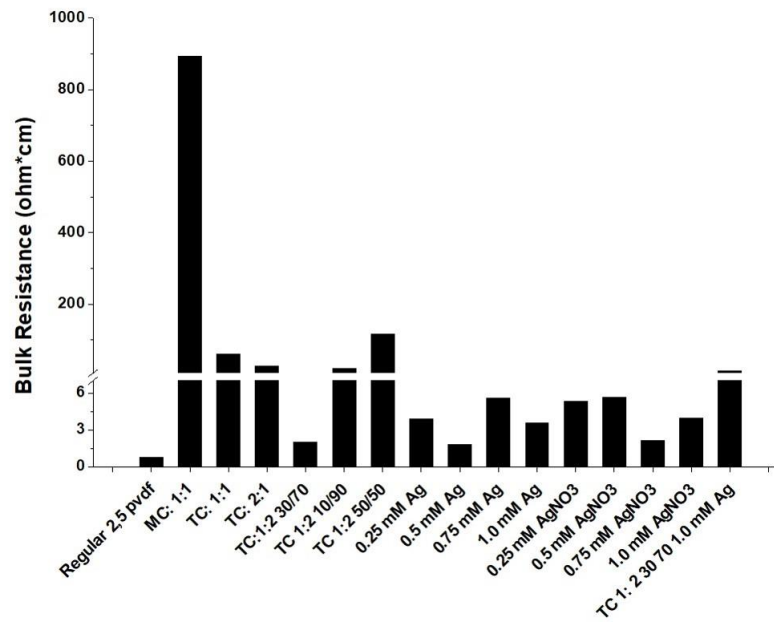


Figure A.4 : Bulk resistivity comparison of all inks.

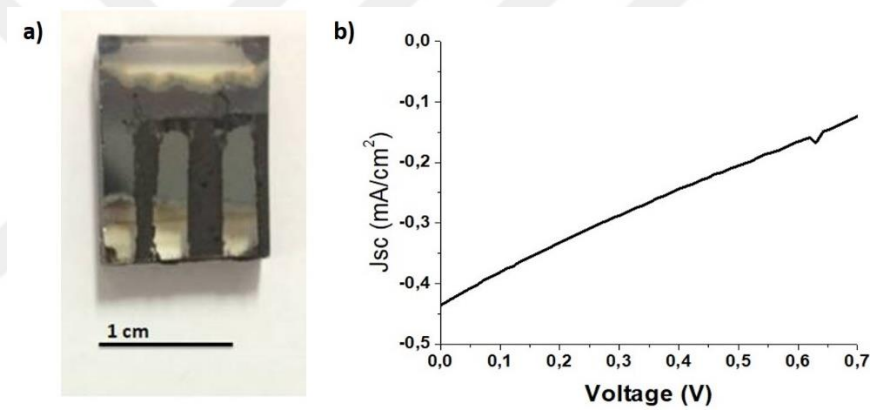


Figure A.5 : a) Perovskite solar cell with low temperature processable carbon ink, and b) Low temperature processable carbon ink coated perovskite solar cell current density-voltage diagram.

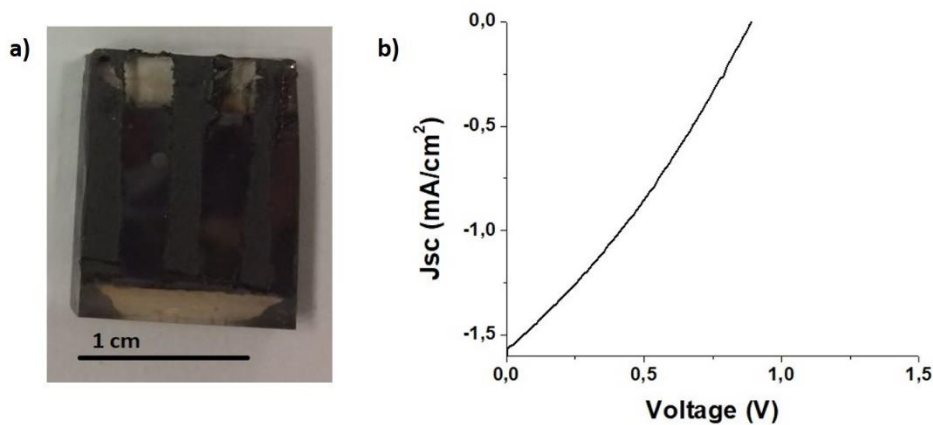


Figure A.6 : a) Perovskite solar cell with TC 1:2 30/70 carbon ink, and b) TC 1:2 30/70 carbon ink coated perovskite solar cell current density-voltage diagram.

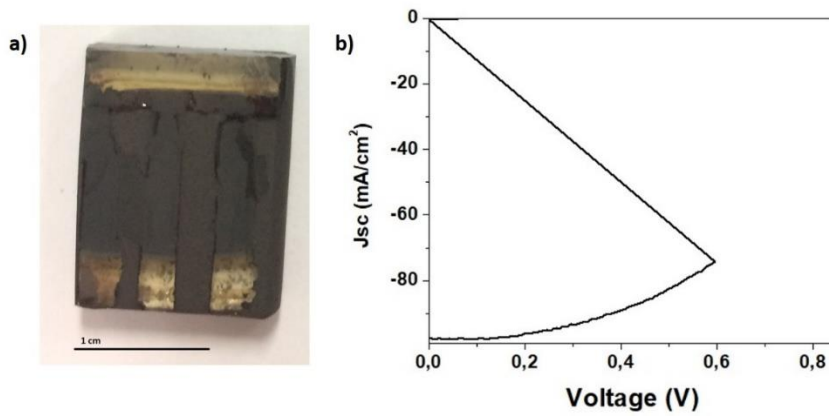


Figure A.7 : a) Perovskite solar cell with 0,25mM Ag doped-PVDF carbon ink, and b) 0,25mM Ag doped-PVDF carbon ink coated perovskite solar cell current density-voltage diagram.

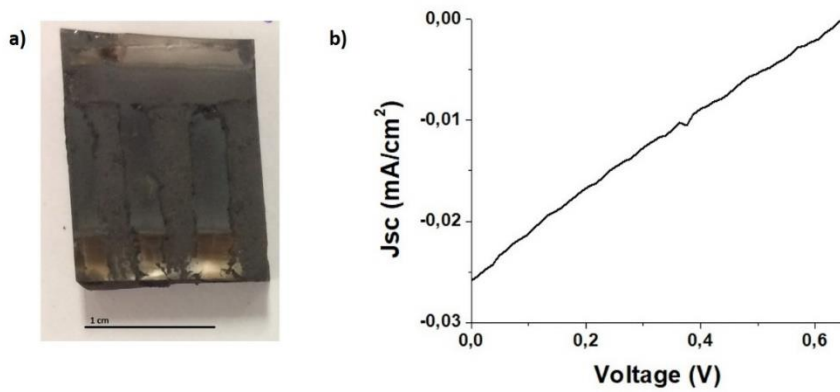


Figure A.8 : a) Perovskite solar cell with 0,5mM Ag doped-PVDF carbon ink, and b) 0,5mM Ag doped-PVDF carbon ink coated perovskite solar cell current density-voltage diagram.

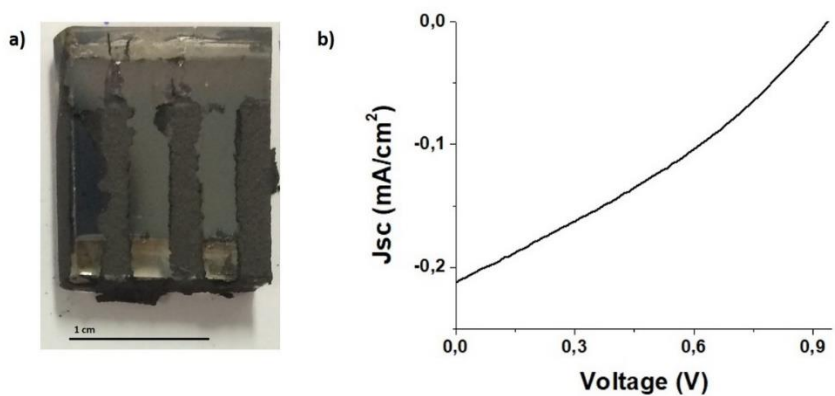


Figure A.9 : a) Perovskite solar cell with 0,75mM Ag doped-PVDF carbon ink, and b) 0,75mM Ag doped-PVDF carbon ink coated perovskite solar cell current density-voltage diagram.

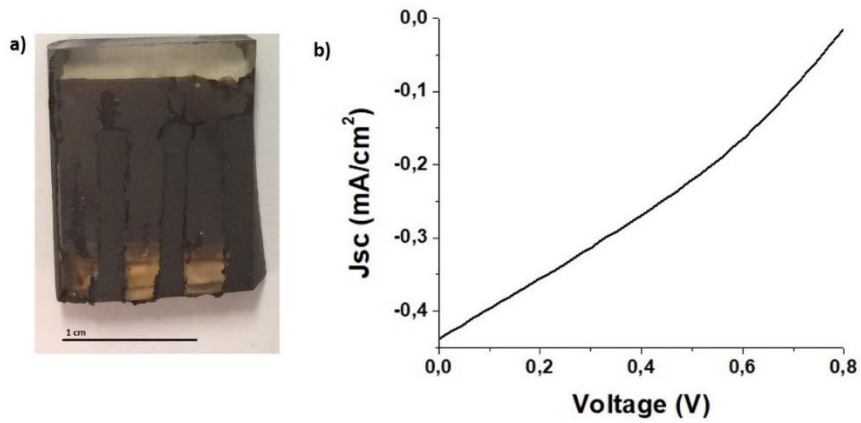


Figure A.10 : a) Perovskite solar cell with 1,0mM Ag doped-PVDF carbon ink, and b) 1,0mM Ag doped-PVDF carbon ink coated perovskite solar cell current density-voltage diagram.

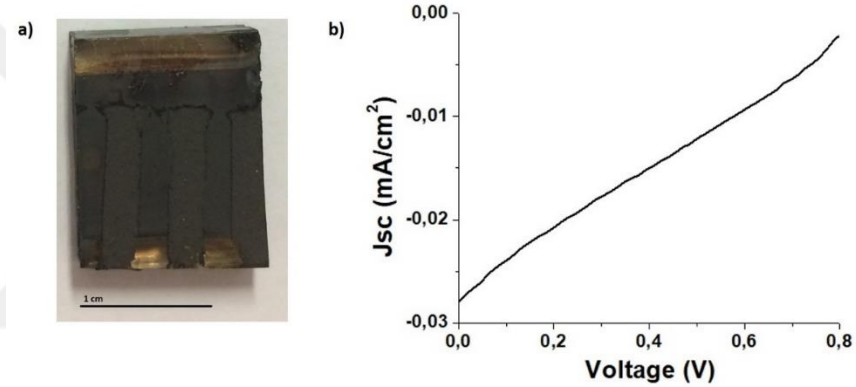


Figure A.11 : a) Perovskite solar cell with 0,25mM AgNO_3 doped-PVDF carbon ink, and b) 0,25mM AgNO_3 doped-PVDF carbon ink coated perovskite solar cell current density-voltage diagram.

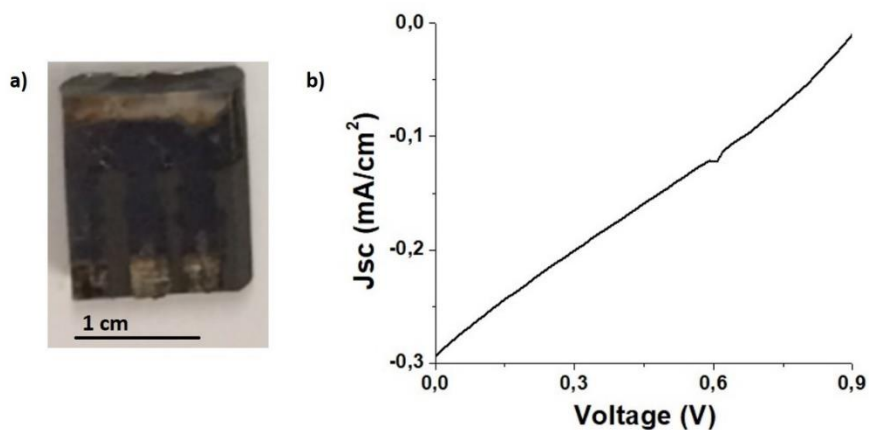


Figure A.12 : a) Perovskite solar cell with 0,5mM AgNO_3 doped-PVDF carbon ink, and b) 0,5mM AgNO_3 doped-PVDF carbon ink coated perovskite solar cell current density-voltage diagram.

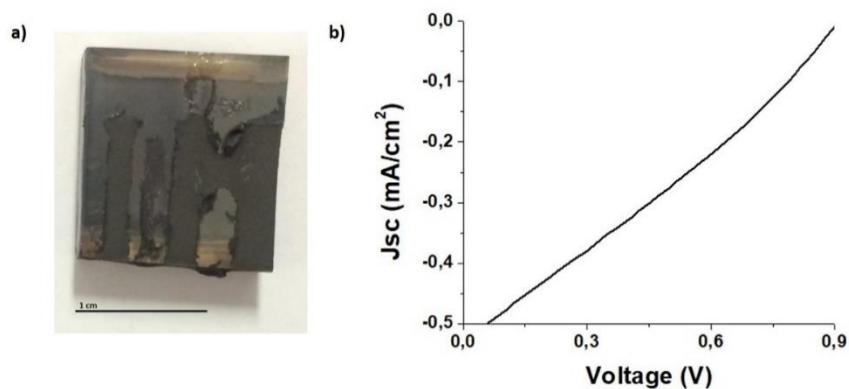


Figure A.13 : a) Perovskite solar cell with 0,75mM AgNO₃ doped-PVDF carbon ink, and b) 0,75mM AgNO₃ doped-PVDF carbon ink coated perovskite solar cell current density-voltage diagram.

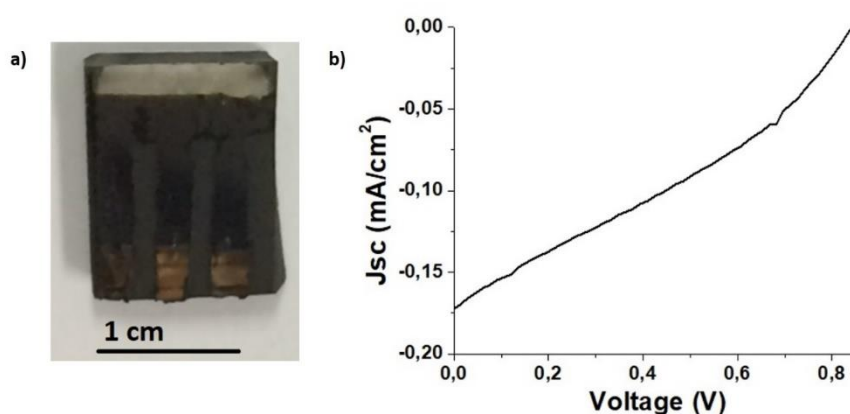


Figure A.14 : a) Perovskite solar cell with 1,0mM AgNO₃ doped-PVDF carbon ink, and b) 1,0mM AgNO₃ doped-PVDF carbon ink coated perovskite solar cell current density-voltage diagram.

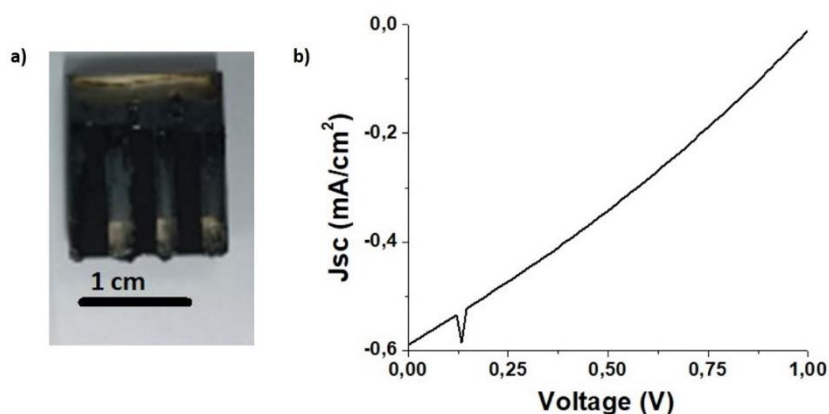


Figure A.15 : a) Perovskite solar cell with TC 1:2 30:70 & 1,0 mM Ag doped PVDF carbon ink, and b) TC 1:2 30:70 & 1,0 mM Ag doped PVDF carbon ink coated perovskite solar cell current density-voltage diagram.

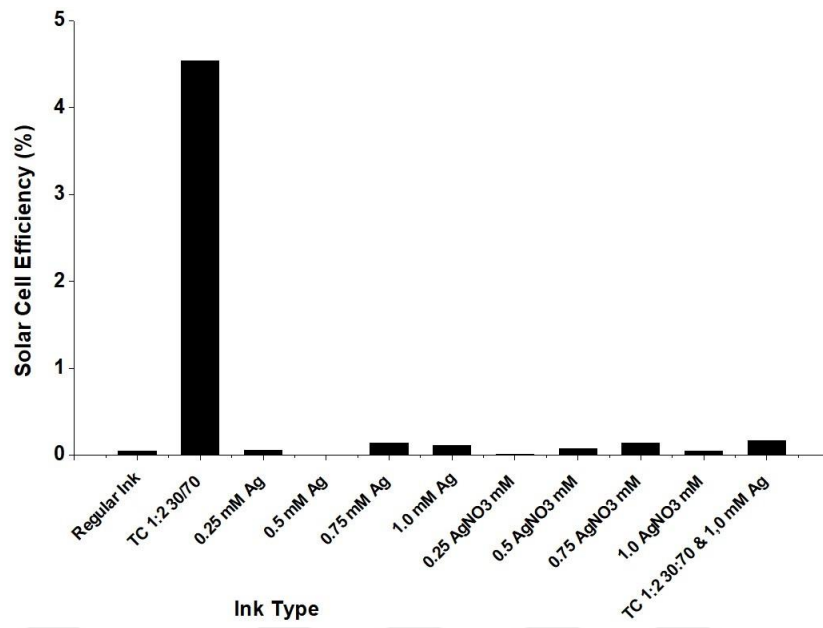


Figure A.16 : Comparison of solar cell efficiency.



CURRICULUM VITAE



Name Surname : Nur Dilara Öztürk

Place and Date of Birth : Istanbul/ Turkey

E-Mail : n.dlr.ozturk@gmail.com

EDUCATION:

- **B.Sc.:** 2014, Istanbul Technical University, Faculty of Textile Technologies and Design, Textile Engineering (Major Degree)
2015, Istanbul Technical University, Faculty of Arts and Sciences, Chemistry (Minor Degree)
- **M.Sc.:** 2018, Istanbul Technical University, Graduate School of Science Engineering and Technology, Nano Science and Nano Engineering

PROFESSIONAL EXPERIENCE AND REWARDS:

- Researcher at TEMAG Laboratory, September 2017- current
- Assistant Merchandiser at LC Waikiki, September 2014 - September 2016
- Assistant Merchandiser at Bestseller, July 2014 - September 2014
- Research and Development Intern at Arcelik Group, January 2014 - June 2014 (6 months)
- Consumer Services Personnel (Work and Travel Program) at La Quinta Inns & Suites, June 2013 - September 2013 (4 months)
- Graduate Assistant at Istanbul Technical University, January 2012 - June 2013 (1 year 6 months)
- Perovskite Solar Cell Project for TUBITAK - Project Number: 214M371
- Book Chapter : Carbon foams in Nanocarbon and its Composites: Preparation, Properties and Applications- Co-author - Publisher: Elsevier (Accepted Manuscript)
- SEM Certificate